Master's thesis

2023

Margrethe Klokkehaug

NTNU
Norwegian University of
Science and Technology
Faculty of Natural Sciences
Department of Materials Science and Engineering

Margrethe Klokkehaug

Al-Doped LLZO Synthesized via Spray Pyrolysis of Carbon-Free Nitrate Precursors

July 2023

NTNU
Norwegian University of
Science and Technology

NTNU
Norwegian University of
Science and Technology

NTNU
Norwegian University of
Science and Technology

Al-Doped LLZO Synthesized via Spray Pyrolysis of Carbon-Free Nitrate Precursors

Margrethe Klokkehaug

Chemical Engineering and Biotechnology
Submission date: July 2023
Supervisor: Mari-Ann Einarsrud and Kjell Wiik
Co-supervisor: Leif Olav Jøsang

Norwegian University of Science and Technology
Department of Materials Science and Engineering

Preface

This study was written as a part of the course TMT4900 Materials Chemistry and Energy Technology at the Department of Materials Science and Engineering at the Norwegian University of Science and Technology during the spring of 2023.

First off, I would like to express my deepest gratitude to my supervisors, Mari-Ann Einarsrud and Kjell Wiik. Their guidance and advices have been exceptional throughout the year. Additionally, I would like to thank my co-supervisor, Leif Olav Jøsang from CerPoTech AS, for his contributions, including spray pyrolysis and valuable input throughout this year's investigation. Furthermore, I would like to acknowledge Florian Flatscher for providing impedance measurements and his help in interpreting the results.

Thank you to all my fellow students in MTKJ and my friends in NTNUI handball for making the past 5 years in Trondheim truly wonderful. I cannot emphasize enough how much I appreciate every one of you. A special thanks goes to "Mattek-gang" for continuously brightening the mood during lunch breaks and good conversations. Finally, I am sincerely grateful for the unconditional support I received from my amazing family and friends in Ålesund, and my wonderful boyfriend. Their strong encouragement has been invaluable throughout this journey, and I am forever grateful.

Margrethe Klokkehaug

Trondheim, July 2023

Acknowledgements

In addition to my supportive and patient supervisors, I would like to express my gratitude towards all laboratory engineers at IMA that have been involved in my work. A special recognition goes to Caren Regine Zeiger for countless training sessions and for introducing me to the independent work in the laboratory, Elvia Anabela Chavez Panduro for facilitating for great XRD measurements, Johannes Ofstad for valuable assistance during spark plasma sintering and density measurements, Sergey Khromov for helpful input on SEM imaging, Eli Beate Jakobsen Larsen for training in CIP, and Andrey Kosinskiy for help with casting and polishing. Thank you to all the people in FACET ceramics group and battery group for feedback throughout the year and for providing motivation through knowledge-sharing on a weekly basis.

Abstract

Solid-state electrolytes are currently investigated for use in Li-ion batteries, substituting the organic liquid electrolytes in current battery technology. This will improve battery safety, chemical and thermal stability, and create new opportunities in the selection of anode materials. Al-doped $Li_7La_3Zr_2O_{12}$ (LALZO) is one of the most promising materials for use as solid-state electrolyte, and has been greatly investigated recent years. The material is traditionally synthesized using solid-state reaction. However, solution-based synthesis offers the advantage of facilitating for improvements in homogeneity and particle size. In solution-based synthesis, organic complexing agents are commonly used, which promotes formation of Li_2CO_3.

The aim of this work was to suppress formation of Li_2CO_3 during solution-based synthesis, as the presence lowers the ionic conductivity by occupying the Li charge carriers and distorting the crystal structure. Hence, carbon-free nitrate precursors were utilized. Two compositions of 17 mol% (17-LALZO) and 24.2 mol% (24,2-LALZO) Li excess were synthesized by spray pyrolysis, providing the stoichiometries $Li_{7.31}Al_{0.25}La_3Zr_2O_{12}$ and $Li_{7.76}Al_{0.25}La_3Zr_2O_{12}$. An excess of Li was added to secure adequate Li content, as Li loss caused by formation of volatile lithium compounds (VLCs) during heat treatments is evident. Precursor powders were calcined in ambient air at 750 °C for 6 h, resulting in t-LALZO for 24,2-LALZO due to Li surplus, and c-LALZO for 17-LALZO. Both calcined powders were observed with Li_2CO_3 due to exposure to ambient air during the initial phase of the synthesis. 17-LALZO was observed with $La_2Zr_2O_7$ as a consequence of Li loss during the heat treatment.

The calcined powders were sintered using two sintering methods: two-step sintering and spark plasma sintering. Single phase c-LALZO was achieved after two-step sintering in ambient air of 17-LALZO, using a primary sintering temperature of 1150 °C for 10 min and secondary sintering temperature of 1000 °C for 6 h. The use of a powder bed of high Li content during sintering provided enough Li for removing $La_2Zr_2O_7$, and the time and temperature was sufficient for complete removal of Li_2CO_3. Abnormal grain growth was successfully suppressed for all two-step sintered samples of 17-LALZO, evident from a homogeneous microstructure and narrow grain size distribution. The relative densities of the samples, ranging from 88.2 to 90.4%, were below the threshold at which abnormal grain growth typically occurs (around 92%). Two-step sintering of 24,2-LALZO resulted in single phase t-LALZO and abnormal grain growth for all sintered pellets, due to the higher Li content and subsequently formation of Li-Al-O phases, inducing higher diffusion rates and high relative densities (91.8 to 93.4 %). Sintering at 1150 °C for 10 min and 1000 °C for 0.5 h resulted in an ionic conductivity of 4.3×10^{-4} S/cm for 17-LALZO, while 5.6×10^{-6} S/cm was achieved for 24,2-LALZO. 17-LALZO exhibited two temperature ranges with different activation energies, 0.22 eV for temperatures lower than 80 °C and 0.47 eV for higher, suggesting a shift in conductivity mechanism from grain boundaries to bulk (grain) with increasing temperature. Spark plasma sintering was considered unsuccessful in this work due to the use of graphite dies, causing excessive Li loss during sintering.

Sammendrag

Faststoff elektrolytter blir for tiden undersøkt for bruk i Li-ion batterier som en erstatning for de organiske væskebaserte elektrolyttene som brukes i dagens batterier. Dette vil forbedre batterisikkerheten, kjemisk og termisk stabilitet, og vil gi muligheter innen valg av anodematerialer. Al-dopet $Li_7La_3Zr_2O_{12}$ (LALZO) er en av de mest lovende materialene for bruk som faststoff elektrolytt, og har blitt studert grundig spesielt de siste årene. Materialet er vanligvis syntetisert ved hjelp av faststoff syntese. Løsningsbasert syntese har derimot den fordelen at det er mulig å forbedre homogenitet og partikkelstørrelse. Ved løsningsbasert syntese er det vanlig å benytte organiske komplekseringsmidler, som fremmer dannelsen av Li_2CO_3.

Formålet med dette arbeidet var å undertrykke dannelsen av Li_2CO_3 ved løsningsbasert syntese, da tilstedeværelsen svekker den ioniske ledningsevnen ved å okkupere Li-ladningsbærerne og forstyrrer dermed krystallstrukturen. Derfor ble karbonfrie nitratforløpere brukt. To sammensetninger med 17 mol% (17-LALZO) og 24.2 mol% (24,2-LALZO) overskudd av Li ble syntetisert ved spray pyrolyse, som gav støkiometriene $Li_{7.31}Al_{0.25}La_3Zr_2O_{12}$ og $Li_{7.76}Al_{0.25}La_3Zr_2O_{12}$. Et overskudd av Li ble inkludert for å sikre tilstrekkelig innhold av Li, da tap av Li forårsaker dannelse av flyktige litiumforbindelser (VLCs) under varmebehandling. Forløperpulvere ble kalsinert i omgivende luft ved 750 °C i 6 t, som resulterte i t-LALZO for 24,2-LALZO grunnet overskudd av Li og c-LALZO for 17-LALZO. De kalsinerte pulversammensetningene ble observert med Li_2CO_3 grunnet eksponering for omgivende luft i den innledende fasen av syntesen. 17-LALZO ble observert med $La_2Zr_2O_7$ som en konsekvens av tap av Li under varmebehandlingen.

Kalsinert pulver ble sintret ved hjelp av to sintringsmetoder: to-stegs sintring og spark plasma sintring. Enfase c-LALZO ble oppnådd etter to-stegs sintring i omgivende luft for 17-LALZO, med primær sintringstemperatur 1150 °C i 10 min og sekundær sintringstemperatur 1000 °C i 6 t. Bruken av pulverseng med høyt innhold av Li under sintring tilførte nok Li til pelleten for å fjerne $La_2Zr_2O_7$, og tiden og temperaturen var tilstrekkelig for fullstendig dekomponering av Li_2CO_3. Undertrykkelsen av unormal kornvekst var vellykket for alle to-stegs sintrede prøver av 17-LALZO, noe som tydelig framgikk av en homogen mikrostruktur og en smal kornstørrelsesfordeling. Relativ tetthet oppnådd, mellom 88.2 og 90.4 %, var under grensen hvor unormal kornvekst vanligvis oppstår (rundt 92 %). To-stegs sintring av 24,2-LALZO resulterte i enfase t-LALZO og unormal kornvekst for alle sintrede pellets på grunn av det høyere innholdet av Li og følgelig dannelse av Li-Al-O-faser, som induserte høyere diffusjonsrater og høyere relativ tetthet (91.8 til 93.4 %). Sintring ved 1150 °C i 10 min og 1000 °C i 0,5 t resulterte i en ionisk ledningsevne på 4.3×10^{-4} S/cm for 17-LALZO, mens 5.6×10^{-6} S/cm ble oppnådd for 24,2-LALZO. 17-LALZO viste to temperaturområder med ulike aktiveringsenergier, 0.22 eV for temperaturer lavere enn 80 °C og 0.47 eV for høyere, som tyder på et skifte i mekanismer for ledningsevne fra korngrenser til korn ved økende temperatur. Spark plasma sintring ble ansett som mislykket i dette arbeidet på grunn av bruken av grafitt-stempel, som forårsaket massivt tap av Li under sintring.

Table of Contents

Abbreviations

AAS Ambient air sintering
AC Alternating current
AGG Abnormal grain growth
BE Blocking electrode
BSE Backscattered secondary electrons
CIP Cold isostatic pressing
CR Cooling rate
CTEM Continuous threat exposure management
DC Direct current
DSC Differential scanning calorimetry
EC Equivalent circuit
EDS Energy-dispersive X-ray spectroscopy
EIS Electrochemical impedance spectroscopy
GB Grain boundary
HIP Hot isostatic pressing
HT High temperature
HR Heating rate
LALZO $Li_{6.25}Al_{0.25}La_3Zr_2O_{12}$
LLZO $Li_7La_3Zr_2O_{12}$
LSR Liquid-state reaction
NGG Normal grain growth
NMR Nuclear magnetic resonance
MARS Microwave assisted reactive sintering
PB Powder bed
RD Relative density
RT Room temperature
SE Secondary electrons
SEM Scanning electron microscopy
SPS Spark plasma sintering
SSLB Solid-state Li-ion battery
SSR Solid-state reaction
SSS Single-step sintering
TGA Thermogravimetric analysis
TSS Two-step sintering
VLC Volatile lithium compound
XRD X-ray diffraction

List of Figures

List of Tables

1 Background

1.1 Motivation

Renewable energy sources are an important part of the energy supply system and are expected to be even more dominating during the next few decades. Thus, energy storage systems of high quality are required to secure consistent energy access. Rechargeable Li-ion batteries (LiB) with liquid or polymer-based electrolytes, as shown in Figure 1.1, are utilized in several portable electronic devices as of today, but due to safety issues and limitations, like Li dendrite formation, flammability and leakage [1, 2, 3], alternative solutions to the elements of the batteries are carefully and continuously considered.

Solid-state Li-ion batteries (SSLB) are one of the possible and most promising alternative solutions to the issues connected to traditional LiB, where a solid-state electrolyte will increase the thermal and chemical stability of the battery and thus remove several of the safety issues. The anode material can be switched to improve the conductivity of the electric device, and using Li as anode material would be favourable as it increases the concentration of the charge carrier. Graphite is commonly used in LiB with highest specific capacity of 372mAhg^{-1}. Switching to metallic lithium, with a specific capacity of 3860 mAhg^{-1}, would have a significant impact on the performance of the electrochemical cell [4].

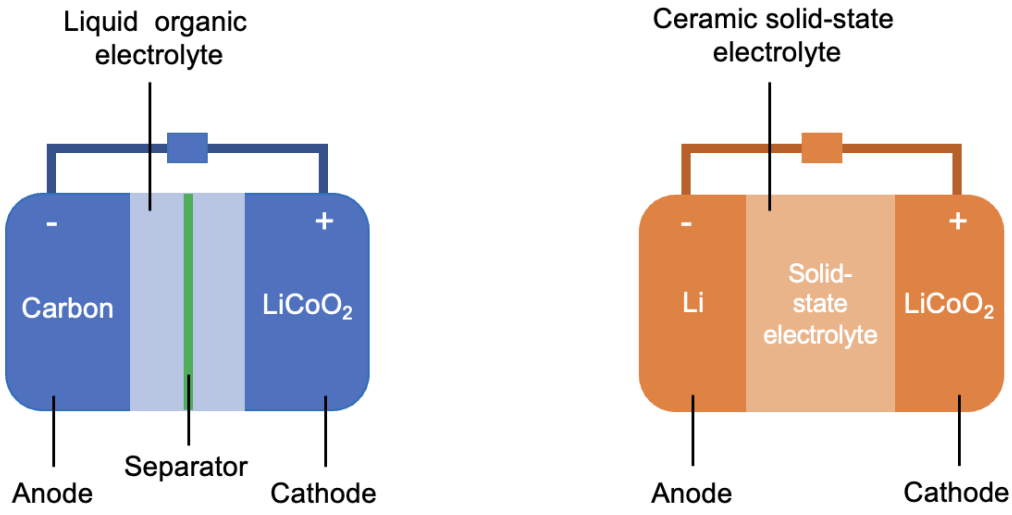

Figure 1.1: Traditional Li-ion battery using carbon as anode material (left). Solid-state Li-ion battery with Li substitution of anode material and a solid-state electrolyte (right).

The cubic garnet of nominal composition $Li_7La_3Zr_2O_{12}$ (LLZO) has proven to possess the highest measured ionic conductivity for the Li-based class of garnets [5, 6], and will be further investigated during this work with respect to ionic conductivity, microstructure, phase composition and sinterability. The material has shown high stability and low reactivity, a necessity for use as an electrolyte in batteries.

One of the biggest issues during synthesis of LLZO is the formation of the secondary phase Li_2CO_3 causing decreased ionic conductivity. This is mainly due to the use of organic complexing agents, like citric acid, during the initial phase of liquid-based synthesis. This work is an extension of the work done by Klokkehaug in 2022, where synthesis of Al-doped LLZO were done by using carbon-free nitrate precursors and spray pyrolysis as manufacturing method [7]. The project resulted in single phase Al-doped LLZO with cubic crystal structure from 24.2% to 12% Li excess precursor solution. Abnormal grain growth and high porosity were observed after sintering. By introducing alternative sintering methods, this work aims to improve the microstrure of the sintered pellets with uniform grain size distribution, normal grain growth and small grains while obtaining a single phase material.

1.2 Aim of work

The objective of this study is to suppress the formation of Li_2CO_3 by employing carbon-free water based nitrate precursors during the synthesis of Al-doped LLZO, as the presence of Li_2CO_3 reduces the ionic conductivity. The secondary phase occupies the lithium charge carriers and causes distortions in the crystal structure. Further on, the work aims to investigate the sintering properties of Al-doped LLZO manufactured by spray pyrolysis with varying Li-content in precursor solutions. Excess of lithium will be added to secure adequate Li-content after the spray pyrolysis and further heat treatments, as research has shown significant Li loss during these processes. Also, suppressing abnormal grain growth (AGG) during sintering by using different sintering methods and durations will be a central aim. The powder precursors will be synthesized by spray pyrolysis, followed by calcination for decomposing traces of nitrites. Two sintering methods will be compared and examined: two-step sintering (TSS) and spark plasma sintering (SPS). Sintering time and temperature will be varied to improve the microstructure of the material. In order to examine the development of the powders and analyze the properties of the final products, several analytical methods will be employed.

A thermogravimetric analysis (TGA) will be conducted of the powder precursors to determine fraction of volatile components and thermal stability, together with differential scanning calorimetry (DSC) to identify decomposition and formation of chemical compounds during heating. The microstructure and shape of the precursor powders, calcined powders and sintered pellets will be investigated by scanning electron microscopy (SEM) and energy-dispersive X-ray spectroscopy (EDS). Phase identification will be done by X-ray diffraction (XRD). Archimedes' method will be utilized to assess the density of the pellets, while the Li-ion conductivity will be measured by electrochemical impedance spectroscopy (EIS).

2 Introduction

2.1 Transition to solid-state batteries

In general, Li-ion batteries are constructed with a graphite anode, a layered oxide cathode, and a liquid electrolyte enabling flow of Li^+ in the battery. In the electrolyte, a permeable separator prevents short circuits between the electrodes while permitting the movement of ionic charge carriers. However, several safety issues associated with the formation of lithium dendrites, overcharging, thermal runaway, current collector dissolution, and gas evolution are present, leading to investigate substitute electrolyte and electrode materials [1, 2].

A solid-state Li-ion battery employs a solid electrolyte to separate the electrodes and enables the flow of charge carriers, improving the thermal and chemical stability of the electronic device. Certain materials have been identified as superior solid-state electrolytes due to their ionic conductivity and stability, with $Li_7La_3Zr_2O_{12}$ being one such material with exceptional properties [8, 9].

2.2 Structure of $Li_7La_3Zr_2O_{12}$

$Li_7La_3Zr_2O_{12}$ (LLZO) is categorized under the garnet crystallographic structure with general formula of $A_3B_2C_3O_{12}$. The A-sites consist of La^{3+} in an 8-coordinated arrangement, while the octahedral B-sites are occupied by Zr^{4+}, and tetragonal C-sites are occupied by Li^+ [5, 6]. The crystal structure is distorted due to an excess of Li^+, which deviates from the traditional garnet structure, occupying interstitial sites and causing the possibility of a tetragonal distortion.

The crystal structure is determined by the positioning of Li^+. LLZO has two polymorphs: tetragonal (space group I41/acd No. 142) and cubic (space group Ia-3d No. 230), as illustrated in Figures 2.1 and 2.2, respectively. The cubic crystal structure of LLZO (c-LLZO) has a framework of edge-sharing dodecahedral LaO_8 and octahedral ZrO_6, with Li^+ distributed disorderly in Li symmetry sites with partial occupancies in tetrahedral 24d, Li(1), and octahedral 96h sites, Li(2). In contrast, tetragonal LLZO (t-LLZO) exhibits an ordered crystal structure, with Li^+ occupying tetrahedral 8a, octahedral 16f, and 32g sites with the same framework [10, 9, 5, 11].

The arrangement of Li^+ on Li sites has a significant impact on the material's ionic conductivity. The loop structures in Figures 2.1 and 2.2 present the lithium diffusion pathways in c-LLZO and t-LLZO. In c-LLZO, both Li(1) and Li(2) possess occupancy degrees lower than 1. The Li(2)-sites are restricted due to the Coulombic repulsion between the neighboring ions, preventing 96h sites from being fully occupied simultaneously. A tetrahedral distortion of the cubic structure, into t-LLZO, transforms the 24d sites into fully occupied 8a and unoccupied 16e sites as shown in Figure 2.2. Additionally, 96h sites are transformed into fully occupied 16f and 32g sites [8].

Monitoring the crystal structure of LLZO is crucial to understand and determine the ionic conductivity, as the occupancy and arrangement of Li^+ on Li sites significantly affect the conductivity [8].

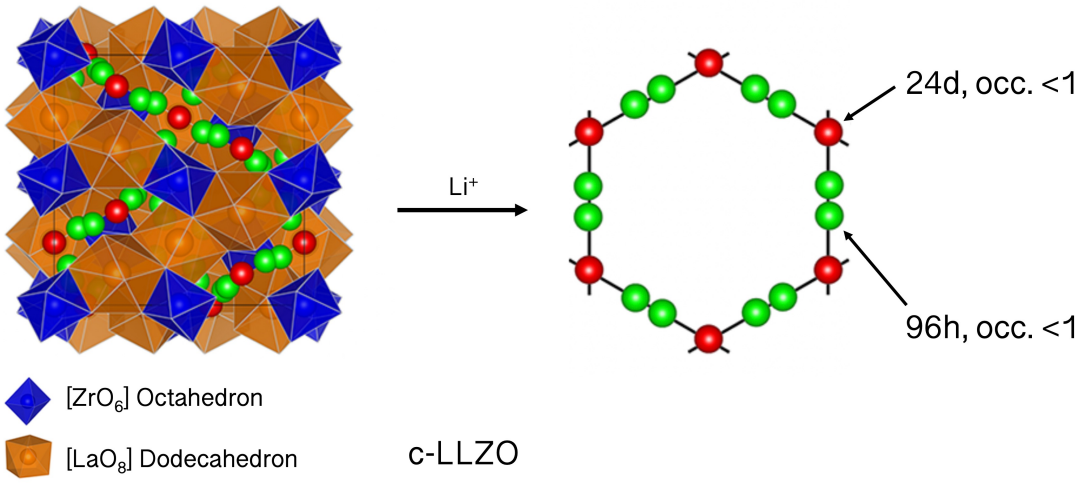

Figure 2.1: Cubic structure of LLZO to the left with disordered distribution of Li^+. ZrO_6 octahedron and LaO_8 dodecahedron are shown in blue and brown spheres, respectively. Arrangement of Li^+ is included, with Li(1) in red and Li(2) in green. Reprinted (adapted) with permission from Fei Chen et al. "Origin of the phase transition in lithium garnets". The Journal of Physical Chemistry C 122.4 (2018), pp. 1963–1972. Copyright 2023 American Chemical Society [8].

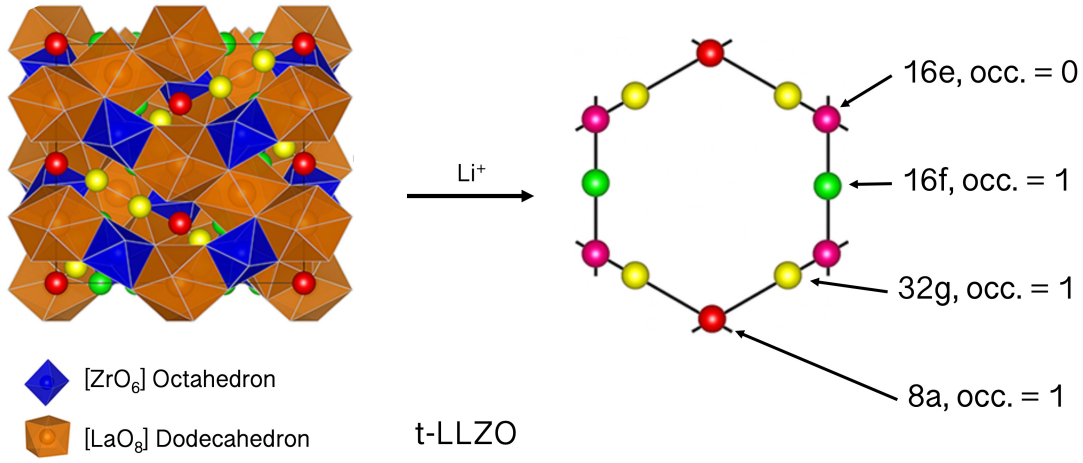

Figure 2.2: Tetragonal structure of LLZO to the left with ordered distribution of Li^+. ZrO_6 octahedron and LaO_8 dodecahedron are shown in blue and brown spheres, respectively. Arrangement of Li^+ is included, with Li(1) in red, Li(2) in green and Li(3) in pink. Reprinted (adapted) with permission from Fei Chen et al. "Origin of the phase transition in lithium garnets". The Journal of Physical Chemistry C 122.4 (2018), pp. 1963–1972. Copyright 2023 American Chemical Society [8].

2.3 Thermodynamic properties of $Li_7La_3Zr_2O_{12}$

$Li_7La_3Zr_2O_{12}$ (LLZO) exhibits three distinct phases, namely a high temperature (HT) cubic phase, a low temperature (LT) cubic phase occuring while the material is exposed to moisture or CO_2, and a tetragonal phase with ordered lithium sites. Of these phases, only the HT-cubic phase is suitable for use as a solid-state electrolyte due to its high ionic conductivity. The LT-cubic phase and tetragonal phase exhibit significantly lower ionic conductivities. At room temperature, the HT-cubic phase has an ionic conductivity 100 times greater than both the LT-cubic and tetragonal phases, with reported values of 10^{-4} S/cm compared to 10^{-6} S/cm [11, 12].

2.3.1 Undoped $Li_7La_3Zr_2O_{12}$

At ambient conditions, the tetragonal phase of LLZO is thermodynamically favored, primarily due to the electrostatic repulsion that occurs between Li sites in the cubic structure. This Li^+-Li^+ Coulomb repulsion is reduced by distorting the structure into a tetragonal arrangement, which optimizes bond angles and minimizes the energy of the system [8].

The phase transition from tetragonal to cubic crystal structure in LLZO is governed by the entropy of the system [13]. This relationship can be expressed as shown in Equation 2.1, which relates the Gibbs free energy ($\Delta G_{t\rightarrow c}$), enthalpy ($\Delta H_{t\rightarrow c}$), and entropy ($\Delta S_{t\rightarrow c}$) of the tetragonal to cubic phase transition as a function of the absolute temperature T. The entropy contribution to the Gibbs free energy can promote the phase transition from the tetragonal to cubic structure in LLZO.

$$\Delta G_{t\rightarrow c} = \Delta H_{t\rightarrow c} - T\Delta S_{t\rightarrow c} \tag{2.1}$$

To ensure a spontaneous transition reaction, the Gibbs free energy must be negative. Due to the disordering of Li^+, the cubic phase has a higher entropy compared to the tetragonal phase. This results in a positive change in entropy, hence the transition from tetragonal to cubic phase becomes spontaneous when a specific temperature is reached. The critical temperature for the tetragonal to cubic phase transition, $T_{t\rightarrow c}$, can be obtained by equating the Gibbs free energy to zero, as shown in Equation 2.2.

$$\mathrm{T_c} = \frac{\Delta \mathrm{H_{t\rightarrow c}}}{\Delta \mathrm{S_{t\rightarrow c}}} \tag{2.2}$$

Table 2.1 presents transition temperatures obtained from literature, indicating that the complete transition from t-LLZO to c-LLZO occurs at temperatures ranging from 600 to 700 °C. Due to the fact that the structure of LLZO depends on the input energy to maintain its stability, occurrence of a transition at room temperature is not possible. The tetragonal to cubic phase transition is reversible, and the crystal structure will rearrange to its original tetragonal phase as the temperature decreases below the critical transition temperature, T_c. However, the cubic phase of LLZO can be stabilized at room temperature by incorporating supervalent cations into the crystal structure.

Table 2.1: Transition temperatures from tetragonal to cubic crystal structure of LLZO. Experiments are conducted without exposure to moisture.

T_c	Characterization method	Reference
645 °C	XRD	[14]
650	XRD	[12]
602-677 °C	Lattice parameters hysteresis	[15]
527-727 °C	Energy calculations	[8]
$\sim$ 600 °C	XRD, CTEM	[16]
$>$ 350 °C	NMR	[17]

2.4 Al-doped $Li_7La_3Zr_2O_{12}$

The introduction of interstitial elements into the LLZO structure stabilizes c-LLZO at lower temperatures by forming vacancies on Li sites in the tetragonal crystal structure. Several dopants, such as tantalum, niobium, gallium, barium and, as this work is focused on, aluminium, have been investigated for use in LLZO aiming at improving the properties of the material [18].

Among these dopants, aluminium has been extensively studied due to its ability to stabilize c-LLZO. Aluminium-doped LLZO (LALZO) was initially accidentally introduced during high-temperature sintering in alumina crucibles, and has since been one of the most studied interstitial elements for LLZO [19, 20, 21]. It has been found to increase the ionic conductivity by stabilizing the cubic phase of LLZO and by promoting the formation of amorphous Li-Al-O phases displayed in the phase diagram in Figure 2.5. These phases act as sintering aids and increase the Li^+ diffusion rate in the structure [22].

Aluminium ions substitute Li^+ at Li(1) sites in the tetragonal LLZO structure. As Al^{3+} substitutes for three Li^+, two Li vacancies are created, leading to a disordered coordination of Li^+. This is shown in Equation 2.3 using Kroger-Vink notation. Incorporating aluminium into the LLZO structure can result in significant improvements in ionic conductivity due to the stabilization of the cubic phase at lower temperatures.

$$Al_2O_3(s) = 2Al_{Li}^{\cdot\cdot} + 4V_{Li}^{\prime} + 6O_O^{\times} \tag{2.3}$$

A study carried out by Rangasamy et al. has determined that substitution of Li with a dopant content of Al more than 0.82 mol% is crucial for the tetragonal-to-cubic transition of LLZO at room temperature [21]. Below this dopant concentration, the tetragonal phase remains stable [20]. The transition temperature is dependent on the Al-dopant concentration as illustrated in the phase diagram shown in Figure 2.3. In the absence of substitutional Al, the tetragonal phase is stabilized up to 640 °C, while the cubic phase is stable for all temperatures above 0.82 mol% Al. The solubility limit for Al in LLZO is 1.56 mol%, beyond this value two phases, c-LLZO and the secondary phase $LaAlO_3$, will coexist [21, 20, 23].

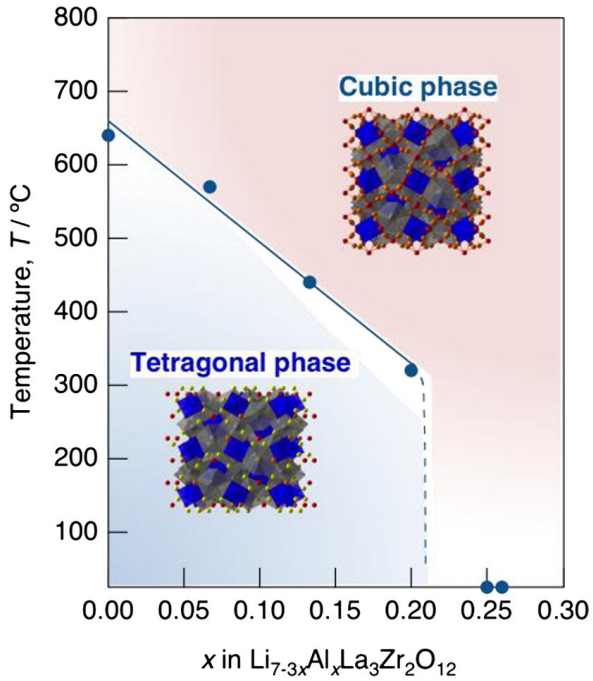

Figure 2.3: Phase diagram of tetragonal and cubic phase LLZO, as a function of Al content x in $Li_{7-3x}Al_xLa_3Zr_2O_{12}$. Reprinted (adapted) with permission from Matsuda et al. "Phase formation of a garnet-type lithium-ion conductor $Li_{7-3x}Al_xLa_3Zr_2O_{12}$". Solid State Ionics 277 (2015), pp. 23–29. Copyright 2023 Elsevier [23].

2.4.1 Formation of secondary phases

The synthesis of Al-doped LLZO poses a significant challenge due to the formation of undesirable secondary phases. Reactions between the oxides present could form secondary phases, as shown in phase diagrams of the systems Li_2O-ZrO_2 and Li_2O-Al_2O_3 in Figures 2.4 and 2.5, respectively. The phases can lead to structural changes and a decrease in the ionic conductivity of the material, making their avoidance crucial for the optimal performance of Al-doped LLZO-based systems [24, 25, 26]. In literature, several primary secondary phases have been identified, which are discussed below.

Tetragonal LLZO may be present due to a low Al dopant content or Li content above critical value. Excess Li above a specific critical value leads to the filling of vacant Li sites, which promotes a distortion of the structure for further Li uptake. This rearrangement of the crystal structure results in tetragonal LLZO [21]. Although it has similar Bragg diffraction line values as the cubic phase, the tetragonal phase differs from the cubic phase by line splitting [27]. Given that Li loss is common during high-temperature heat treatments such as calcination and sintering, it is essential to evaluate the initial Li content during synthesis of Al-doped LLZO to avoid undesired structural changes.

LT-cubic LLZO could form due to exposure to moisture or CO_2 absorption from precursor materials or the ambient atmosphere. The structure exhibits low ionic conductivity of 10^{-6} Scm^{-1} and is unsuitable for use as a solid-state electrolyte. The low ionic conductivity is due to the lower occupancy of Li sites, leading to the formation of secondary phases like Li_2CO_3 and $La_2Zr_2O_7$ hindering Li-ion transport. It can be distinguished from the HT-cubic LLZO using XRD, as it has a slightly larger lattice parameter of 13 Å in addition to the lower ionic conductivity [12]. The formation of LT-cubic phase can be avoided by limiting exposure to moisture and using an inert atmosphere that does not contain CO_2 during synthesis.

Li_2ZrO_3 is a secondary phase that can occur if there is an excessive amount of lithium present. While increasing the Li content could prevent the formation of $La_2Zr_2O_7$, if the amount of excess Li exceeds what lost during heat treatments, residual Li_2ZrO_3 can be formed [28]. Additionally, other stable phases from the Li_2O-ZrO_2 system, such as $Li_6Zr_2O_7$ and Li_8ZrO_6, could also form, as depicted in the phase diagram in Figure 2.4.

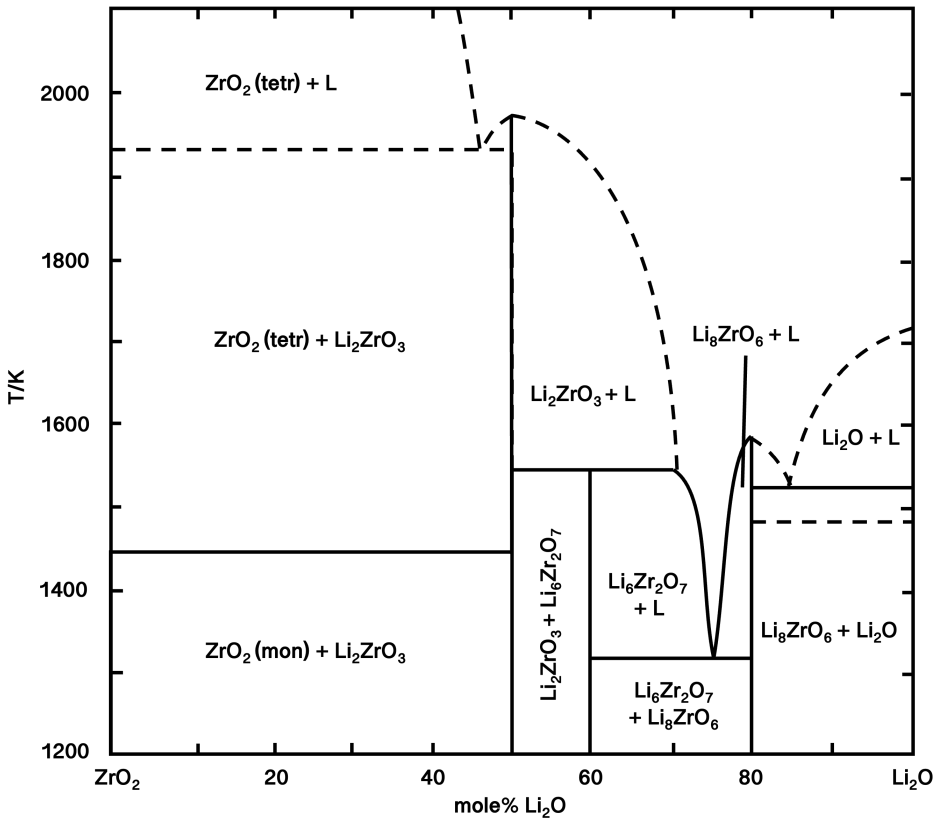

Figure 2.4: Phase diagram of the Li_2O-ZrO_2 system. Reprinted (adapted) with permission from G.P. Wyers, E.H.P. Cordfunke. "Phase relations in the system Li_2O-ZrO_2". Journal of Nuclear Materials 168.1-2 (1989), pp. 24–30. Copyright 2023 Elsevier [29].

Li_2CO_3 is a secondary phase commonly generated during the synthesis of LLZO due to the use of organic complexing agents in the precursor solution or due to exposure to an atmosphere with a high CO_2 content [30]. This compound has a relatively high stability and necessitates a high-temperature treatment to be removed. The presence of Li_2CO_3 results in decreased ionic conductivity by binding Li^+ in the system and impedes the formation of LLZO. To prevent the formation of Li_2CO_3, the use of organic complexing agents should be avoided during wet processing, and the exposure to air should be minimized. The decomposition of Li_2CO_3 occurs at a temperature higher than 723 °C through Equation 2.4 [31, 32]. During the decomposition, Li_2O forms, which can react with $La_2Zr_2O_7$ and generate LLZO, as demonstrated in Equation 2.5.

$$Li_2CO_3(s) \longrightarrow Li_2O(s) + CO_2(g) \tag{2.4}$$

$$2La_2Zr_2O_7(s) + 7Li_2O(s) + La_2O_3(s) \longrightarrow 2Li_7La_3Zr_2O_{12}(s) \tag{2.5}$$

At moderate temperatures and a low partial pressure of CO_2, the rate of decomposition of Li_2CO_3 is inhibited due to Le Chatelier's principle, where the transportation rate of CO_2 out of the structure is reduced. To ensure adequate decomposition of Li_2CO_3, it is necessary to allow sufficient time for the transport of CO_2 during heat treatment. At higher temperatures beyond the melting point of Li_2CO_3, the Gibbs free energy and partial pressure of CO_2 will increase, as shown in Appendix B, causing CO_2 to be transported more rapidly out of the structure [28, 32].

$La_2Zr_2O_7$ (pyrochlore) is frequently observed in LLZO systems, and this is attributed to Li deficiency. During synthesis, heat treatments can lead to a deficiency in lithium as it is a volatile element, thereby resulting in the decomposition of LLZO, as depicted in Equation 2.5 in the reversed direction. However, the addition of an appropriate amount of Li excess during the initial stage of synthesis can prevent the formation of pyrochlore. Also, by providing additional Li during heat treatments in the synthesis could contribute to removal of the impurity phase.

Amorphous Li-Al-O phases have the potential to occur in Al-doped LLZO systems, which can enhance sintering by increasing the Li^+ diffusion rate between grains [22]. The phase diagram for the Li_2O-Al_2O_3 system illustrated in Figure 2.5, indicates eutectic melting point at 1064°C, where Li_5AlO_4, $LiAlO_2$, and a liquid phase coexist. This temperature is below the common sintering temperatures of LLZO, promoting sintering through liquid phase sintering, but could also contribute to abnormal grain growth due to the increased mass transport [22].

$LaAlO_3$ is another secondary phase that could occur in the Al-doped LLZO system. Introduction of too high Al concentration exceeding the solubility limit of Al, leads to formation of $LaAlO_3$ and consequently decreasing the ionic conductivity of the material as it serves as a barrier in the crystal structure [21]. Also, $LaAlO_3$ is commonly formed through solid-state reaction using La_2O_3(s) and Al_2O_3(s), as shown in Equation 2.6. By exposing the powders to heat treatments, typically above 1000 °C, in an oxygen-rich atmosphere, formation of $LaAlO_3$ could be induced [33, 34].

$$La_2O_3(s) + Al_2O_3(s) \longrightarrow 2LaAlO_3(s) \tag{2.6}$$

$Li_{0.5}Al_{0.5}La_2O_4$ could occur in the crystal structure due to Li deficiency or Al surplus. To avoid the formation of this secondary phase, a sufficient concentration of Li should be present as significant Li loss during heat treatments are evident during synthesis of Al-doped LLZO. Providing Li through the use of powder bed of high Li content during sintering is an option for counteracting the decreased Li concentration. The content of Al in the initial precursor should be evaluated to achieve a single phase material and avoid formation of $Li_{0.5}Al_{0.5}La_2O_4$ [35].

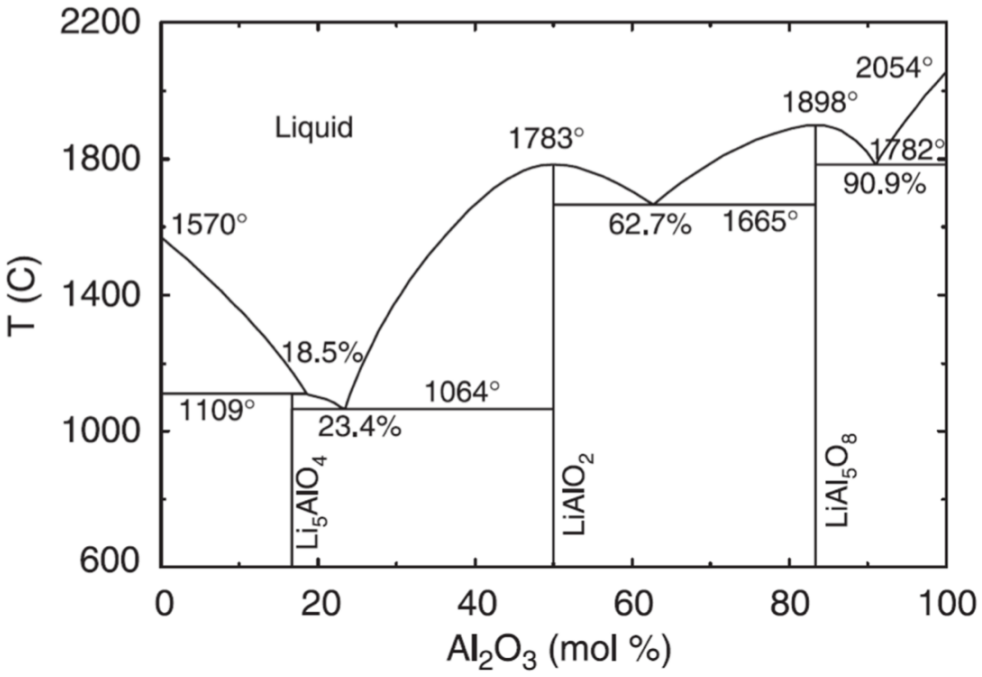

Figure 2.5: Phase diagram of the Li_2O-Al_2O_3 system. Reprinted (adapted) with permission from Karl E. Spear, Theodore M. Besmann, Nagraj S. Kulkarni. "Thermodynamic Optimization of Lithia–Alumina". Journal of the American Ceramic Society 91.12 (2008), pp. 4074–4083. Copyright 2023 John Wiley and Sons [36].

When secondary phases coexist in the LLZO structure, they interfere with the microstructure of the solid-state electrolyte, leading to a decrease in Li-ion conductivity [28]. To optimize the ionic properties of the material, it is of importance to prevent formation of these secondary phases and obtain a single phase material.

2.5 Volatile lithium compounds in Li-garnets

The loss of Li during different stages of the synthesis of LLZO-based materials can result in structural changes and a decrease in ionic conductivity [24, 25, 26]. Such mass loss is primarily caused by formation of volatile lithium compounds (VLCs), reactions with equipment like crucibles, and secondary phases where ions from the original stoichiometry are bound to other chemical compounds, necessitating an external supply of energy to break the bonds.

A study conducted by Huang et al. investigated the existence of VLCs in LLZO compounds through a series of sintering experiments. To capture VLCs during the heat treatments, an Al_2O_3 sheet was used due to the high reactivity to VLC gases. The sheet was not in contact with the powder bed to assure that only the volatile lithium compounds would be deposited. An XRD analysis of the alumina sheet revealed the presence of $LiAl_5O_8$ and $LiAlO_2$ after sintering, confirming the precence of VLCs [37]. The reactions between the alumina sheet and the VLC gases are shown in Equations 2.7 and 2.8, also expected from the phase diagram in Figure 2.5. From solid Li_2O, both Li and Li_2O gases could form through sintering at higher temperatures in vacuum. For sintering in air, the VLCs will primarily consist of $Li_2O(g)$ due to the existence of oxygen and its high vapor pressure compared to Li(g) [38].

$$Li_2O(g) + Al_2O_3(s) \longrightarrow 2LiAlO_2(s) \tag{2.7}$$

$$Li_2O(g) + 5Al_2O_3(s) \longrightarrow 2LiAl_5O_8(s) \tag{2.8}$$

The concentration of VLCs in the powder bed plays a critical role in the densification mechanisms, ionic conductivities, and phase purity during sintering. The optimal concentration is highly dependent on the initial composition of the sintered material, powder bed and sintering program. Lowering the VLC concentration may result in uniform grain growth with trans-granular fractures, but with low ionic conductivity. Increased VLC concentration could enhance the ionic properties of the material, but could also promote abnormal grain growth, inducing low mechanical strength. Hence, there appears to be a critical VLC concentration required for achieving sufficient sintering of green LLZO pellets. Achieving an optimal amount of VLCs is crucial for obtaining a material with properties suitable for use as a solid-state electrolyte, such as high ionic conductivity, high relative density and good mechanical strength.

The crucible material has also shown to have a large impact on the VLCs. Using Al_2O_3, highly reactive with Li, could extract Li from the structure and react while in physical contact. By substituting to an inert material, like MgO and Pt, these undesirable reactions could be avoided. Utilizing powder bed during sintering in alumina crucibles could also remove or limit contact between the sample and the crucible material, but some additional Li loss compared to inert crucibles could still occur.

Further research should aim at the effect of VLCs in solid-state electrolytes during battery operation or cycling, as a reaction with the electrode surface could potentionally cause formation of passivating layers or other undesired side reactions. Understanding and controlling the behavior of VLCs is crucial for maintaining long-term stability in the battery.

2.6 Sintering

To enable the use of Al-doped lithium lanthanum zirconium oxide (LALZO) in Li-ion batteries, it is crucial to achieve a dense material of high mechanical strength. During sintering, the material undergoes diffusion between particles at their contact points. The densification could also be facilitated by the presence of a liquid phase. Bonding between the particles ultimately leads to the formation of a polycrystalline microstructure. As the porosity decreases, the material experiences significant shrinkage. Since many ceramics require close tolerances, monitoring shrinkage and distortion during the sintering process becomes a necessity [39].

It is preferable to have a uniform microstructure with fine grains and a narrow distribution of grain sizes giving high mechanical strength [40]. The microstructure depends greatly on several factors, including the characteristics of the initial powders, the particle size and size distribution, the packing of particles during densification, and the sintering conditions. Precise control of all these variables is necessary to achieve the desired properties and obtain a dense material with high strength. Additionally, as the material is intended for use as a solid-state electrolyte, it should exhibit excellent electrochemical properties, high purity and minimal flaw size. Results from previous sintering studies of Al-doped LLZO are displayed in Table 2.2, showing obtained densities and ionic conductivites for different sintering techniques and conditions.

Table 2.2: Relative densities (RD), ionic conductivities (σ_{RT}) and activation energies (E_a) of Al-doped LLZO from previous studies. Sintering methods and conditions are included. SSR = solid-state reaction, LSR = liquid-state reaction, MARS = microwave assisted reactive sintering, SPS = spark plasma sintering, AAS = ambient air sintering, HIP = hot isostatic pressing.

Synthesis method	Sintering conditions	σ_{RT} [Scm^{-1}]	RD [%]	E_a [eV]	Ref.
SSR	MARS, 2.45 GHz, N_2 atmpsphere, 1200 °C for 3 h	1.1×10^{-4}	89.3	0.36	[41]
SSR	SPS, 1050 °C for 10 min, 75 MPa	0.9×10^{-4}	96	0.42	[42]
SSR	SPS, 1100 °C for 10 min, 40 MPa	2.6×10^{-4}	N/A	N/A	[43]
SSR	SPS, 1150 °C for 10 min, 10 MPa	5.7×10^{-4}	99.8	0.30	[44]
SSR	AAS, 1230 °C for 36 h	5.11×10^{-4}	92	0.31	[45]
SSR	AAS, 1100 °C for 12 h	1.0×10^{-5}	75	0.48	[46]
SSR	AAS, 1100 °C for 12 h, 1200 °C for 12 h	1.44×10^{-4}	90.5	0.42	[46]
SSR	AAS, 1150°C for 15h	1.4×10^{-4}	93	0.31	[47]
SSR	Ar atmosphere, 1150 °C for 10 h	2.4×10^{-4}	90	N/A	[48]
SSR	AAS, 1230 °C for 6 h	4.8×10^{-4}	91	N/A	[49]
SSR	AAS, 1210 °C for 6 h	5.3×10^{-4}	92	0.25	[50]
LSR	AAS, 1150 °C for 2 h	3.0×10^{-4}	88	N/A	[25]
LSR	AAS, 1100 °C for 4 h, LiF sintering aid	1.0×10^{-4}	81	0.29	[51]
LSR	AAS, 1100 °C for 15 h	3.0×10^{-4}	92	0.27	[52]
LSR	AAS, 1100 °C for 3 h	3.3×10^{-4}	N/A	0.28	[53]
LSR	AAS, 1200 °C for 10 h	4.9×10^{-4}	90	0.28	[54]
LSR	HIP, O_2 atmosphere 1180 °C for 5 h	1.2×10^{-4}	97	N/A	[55]

Polycrystalline materials undergo solid-state sintering through the transport along specific pathways, namely the lattice, grain boundary, and surface. These pathways define the mechanisms that promote sintering, as illustrated in Figure 2.6. The possible mechanisms are 1) surface diffusion, 2) lattice diffusion from the surface and 3) evaporation-condensation leading to neck coarsening and change in microstructure without densification, while 4) grain boundary diffusion, 5) lattice diffusion from the grain boundaries and 6) plastic flow are removing material from the grain boundary region and promotes neck growth and densification by dislocation motion [39, 40]. In other words, to increase density in a material it is beneficial to restrict mechanisms 1), 2) and 3), while encouraging mechanisms 4), 5) and 6).

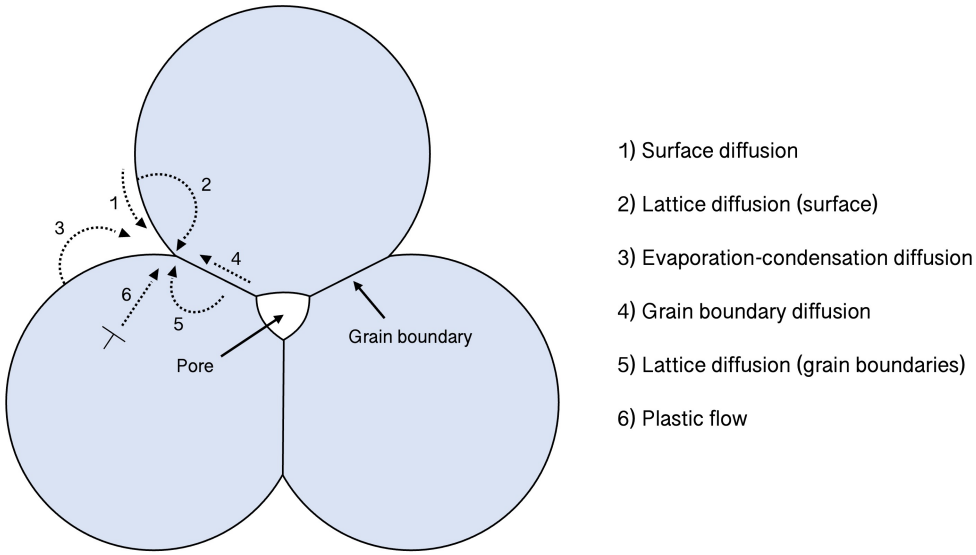

Figure 2.6: Illustration of the possible diffusion mechanisms during solid-state sintering. Figure inspired by [40].

The sintering procedure entails several steps with different purposes, driven by diffusion. In the initial stage, there is a rearrangement of particles and neck formation at the contact area between the particles. The rearrangement includes slight movement or rotation of particles to increase the connectivity. Bonding between the particles takes place at the contact points where material transport can occur and the surface energy is the highest.

The intermediate stage affects the porosity of the material, where the necks between particles grow, porosity decreases, and the centers of the original particles are moving towards each other. This leads to a shrinkage equal to the amount of porosity decrease. The grain boundaries move, causing one particle (now referred to as grain) to grow while neighboring grains are consumed. The geometric changes accommodate for further neck growth and decrease in porosity. If the pore channels are connected, the intermediate sintering continues, and ends when the pores become isolated around 92 % of theoretical density.

The final stage of the sintering process includes removal of the remaining porosity. This is achieved by vacancy diffusion along grain boundaries, and the pores must therefore be located close to the grain boundaries. The removal of porosity and vacancy diffusion are facilitated by the movement of grain boundaries and controlled grain growth. If the grain growth happens too rapidly, the grain boundaries could move faster than the pores, leaving isolated pores within the grain. As the grain continues to grow, the pore is further detached from the grain boundary, and is less likely to be eliminated. Control of grain growth is hence important in order to maximize removal of porosity [56, 39].

The mechanisms that lead to waste of sintering driving force without assisting densification are called coarsening mechanisms. These mechanisms involve consolidation without shrinkage and increased density, leading to low mechanical strength and possible irretrievable porosity. In contrast, materials exposed to densification mechanisms will have an increase in neck area and the centres of the structural units are approaching each other, causing higher density as the mass per volume is increased.

Figure 2.7 describes the rate controlling mechanisms during solid-state sintering inducing densification and coarsening of the material. Several sintering variables may be adjusted to influence the material movements. Temperature, time at chosen temperature, pressure, the powder particle size and shape, and composition of the system with reference to atmosphere and additives could have a significant effect on the sintered material. The sintering variables can be adjusted to affect the mechanisms at the initial and intermediate stages, to promote densification over coarsening. At the final stage of the process, the parameters are reassessed, as the effect of the mechanisms have shown to change [56].

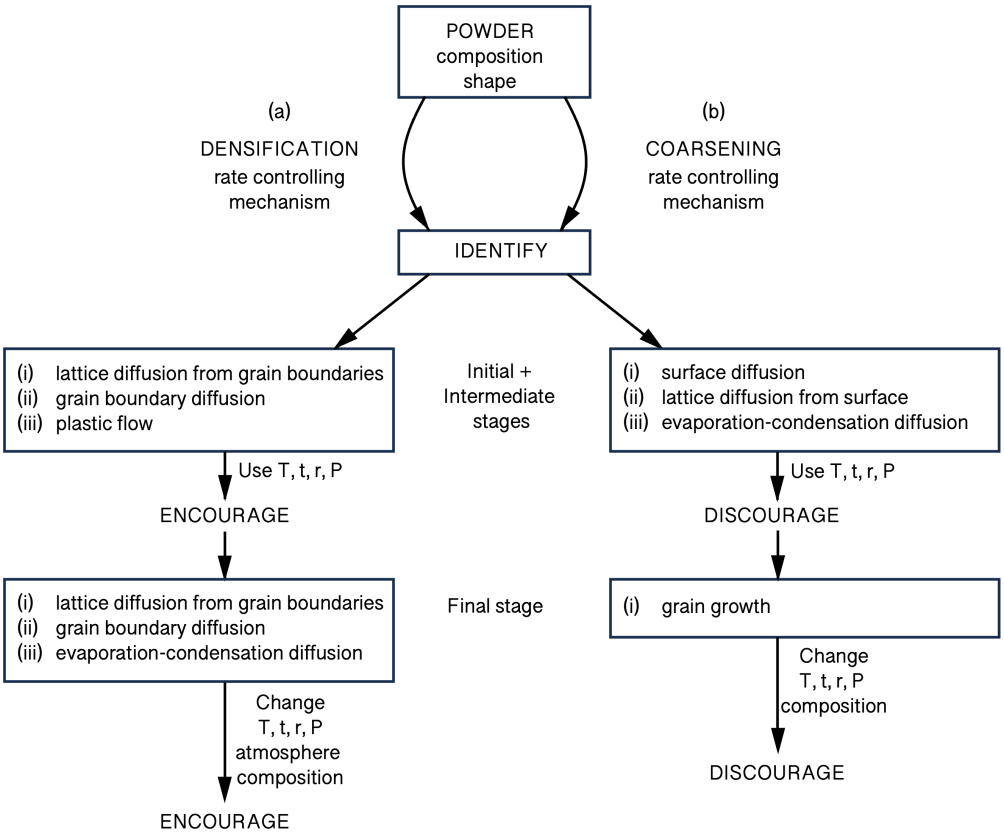

Figure 2.7: Stages of the sintering process including mechanisms and variables. Figure inspired by [56].

The material flux in terms of microscopic driving force for solid-state sintering is derived from Fick's first law, shown in Equation 2.9, where J is the flux, c is the concentration, D_i is the diffusion coefficient, k is Boltzmann's constant, T is the absolute temperature and $\Delta\mu_i$ is the change in chemical potential. The driving force of the material diffusion is the difference in free energy or chemical potential between the free surfaces of particles and the points of contact between the particles. The relation shown in Equation 2.9 is used to predict how change in sintering variables will affect the densification time for each mechanism, as specific cases often requires a specified degree of sample shrinkage or densification [56].

$$J_i = \frac{-cD_i}{kT} \cdot \Delta\mu_i \tag{2.9}$$

Various sintering types can be utilized for optimizing the sintering variables and promoting densification mechanisms through application of heat and/or pressure. Solid-state sintering involves preliminary pressing followed by pressure-less heat-treatment for further densification. Hot-pressing or pressure-sintering involves simultaneous application of pressure and heat, while liquid-phase sintering includes utilizing a limited amount of melt as sintering aid [57]. The present study explores solidification of Al-doped LLZO by two distinct sintering methods: two-step sintering (solid-state) and spark plasma sintering (hot-pressing).

2.6.1 Abnormal grain growth in Al-doped LLZO

Research has indicated that Al-doped LLZO is susceptible to abnormal grain growth (AGG), a phenomenon observed during heat treatment where a few grains experience sudden growth. Due to higher thermodynamic driving forces and difference in curvature, neighboring small grains are absorbed, forming large grains [58]. The captivation of smaller grains will enclose eventual pores in the larger grains. These cannot be retrieved, even with prolonged heat treatments, and will contribute to increased irreversible porosity. AGG leads to a heterogeneous microstructure characterized by a bimodal grain size distribution, causing reduced mechanical strength and stability. Additionally, AGG contributes to lowered ionic conductivity due to symmetry damage of Li^+ distribution and transport channels [59, 52]. Achieving normal grain growth (NGG), characterized by a narrow range of grain sizes and shapes, can yield high density and mechanical strength [58].

Monitoring the chemical composition could be a challenge during sintering at elevated temperatures due to volatile lithium. A significant Li loss could cause, in addition to formation of secondary phases, abnormal grain growth and a substantial decrease in ionic conductivity, as Li^+ is the charge carrier in the material. Utilizing a lower sintering temperature decreases the connectivity, and lowers the relative density and ionic conductivity. Optimizing the temperature program, with several temperature steps, adjust other parameters, like pressure or external energy supply, or applying sintering aids could have big impact on the densification of the material.

In addition to conventional solid-state sintering, that seems promising regarding obtaining high relative density of pure c-LLZO without AGG, the use of sintering additives to lower sintering temperature has been reported, reducing porosity and improving connectivity between the grains [60, 61]. Phases from the Li-Al-O system could function as sintering aids, and are one of the benefits of using Al as dopant of LLZO. Other sintering aids are Li_4SiO_4, MgO and amorphous alumina coating, but an optimal sintering aid is yet to be discovered [62, 24, 63].

2.6.2 Two-step sintering

Two-step sintering (TSS) is commonly employed to achieve a material of high density and tightly bound small grains. The aim of the method is to avoid coarsening during the first step of sintering, which removes densification driving force. The method facilitates for rapid heating and short exposure time at elevated temperatures, promoting high mechanical strength and a homogeneous microstructure [64, 59].

The sintering method involves two steps with distinct purposes. The first step, known as the initial or primary sintering, involves heating the material to an elevated temperature, below its melting point. The material undergoes significant shrinkage and particle rearrangement, leading to neck formation between particles and increased relative density. The second step, often referred to as the final or secondary sintering, is at a lower temperature, and enhances the final densification of the material while minimizing grain growth. By reducing the sintering temperature in the second step, the grain growth is limited, which allows for better control over the microstructure and more customized properties [65].

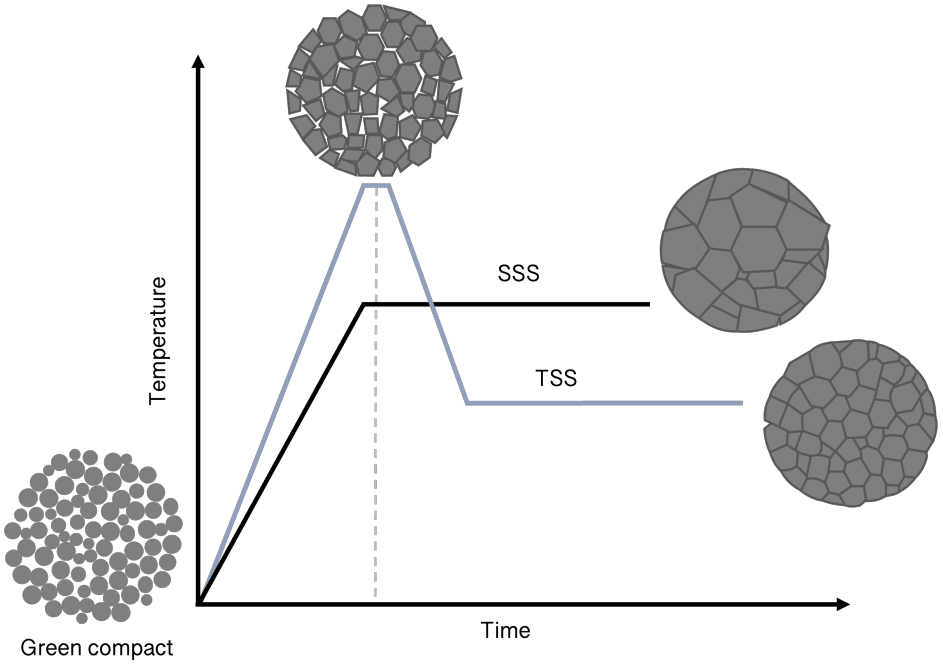

Figure 2.8: Difference in microstructure for single-step sintering (SSS) and two-step sintering (TSS). Figure inspired by [65].

The difference in microstructure between conventional sintering and two-step sintering is illustrated in Figure 2.8. Two-step sintering has several advantages over alternative densification methods. In comparison to more advanced sintering techniques, it provides a cost-effective approach while achieving high-density materials [65]. Additionally, the two-step sintering process can effectively reduce the occurrence of defects like cracks and voids by controlling the sintering rate during the secondary sintering stage.

Xu et al. compared single-step sintering to multi-step sintering of Al-doped LLZO with respect to relative density and ionic conductivity. Two-step sintering resulted in a relative density of 90.5 % and ionic conductivity of 1.44 $\times$ 10^{-4} S/cm, where the material was exposed to 1100 °C for 12 h at the initial step followed by 1200 °C for 12 h. The single-step sintering yielded a relative density of 75 % and an ionic conductivity of 1.01 $\times$ 10^{-5} S/cm, proving that two-step sintering could enhance the material's properties [46].

2.6.3 Spark plasma sintering

Spark plasma sintering (SPS) involves applying uniaxial pressure and pulsed direct current (DC) to rapidly heat and densify powder particles, where heat is produced by Joule heating, electrical discharges and high-temperature plasma [39]. It is typically carried out in a vacuum or in a protective atmosphere. Comparing SPS to solid-state sintering and hot pressing, characterized with long duration and high temperature, SPS can be done rapidly as the heat generation is caused by the electrothermal effect [66].

The process of spark plasma sintering is displayed in Figure 2.9. The heat is only distributed in the die-punch instead of the whole furnace chamber, requiring less energy supply. There exist some uncertainties regarding the mechanisms of SPS, but it is believed to be based on the generation of sparks between the gaps among powder particles, as shown in 2.9b, allowing the current to pass through. These sparks, occurring either between gaps or at contact points, result in localized heating within the discharge column at the start of a DC pulse, illustrated in 2.9c, raising the temperature to above 1000 °C. The high temperature facilitates the melting and evaporation of powder particles, and the gas between the particles is believed to be transformed to plasma through ionization, displayed in 2.9d. This enables formation of necks around the contact surface, as shown in Figure 2.9e [67, 39].

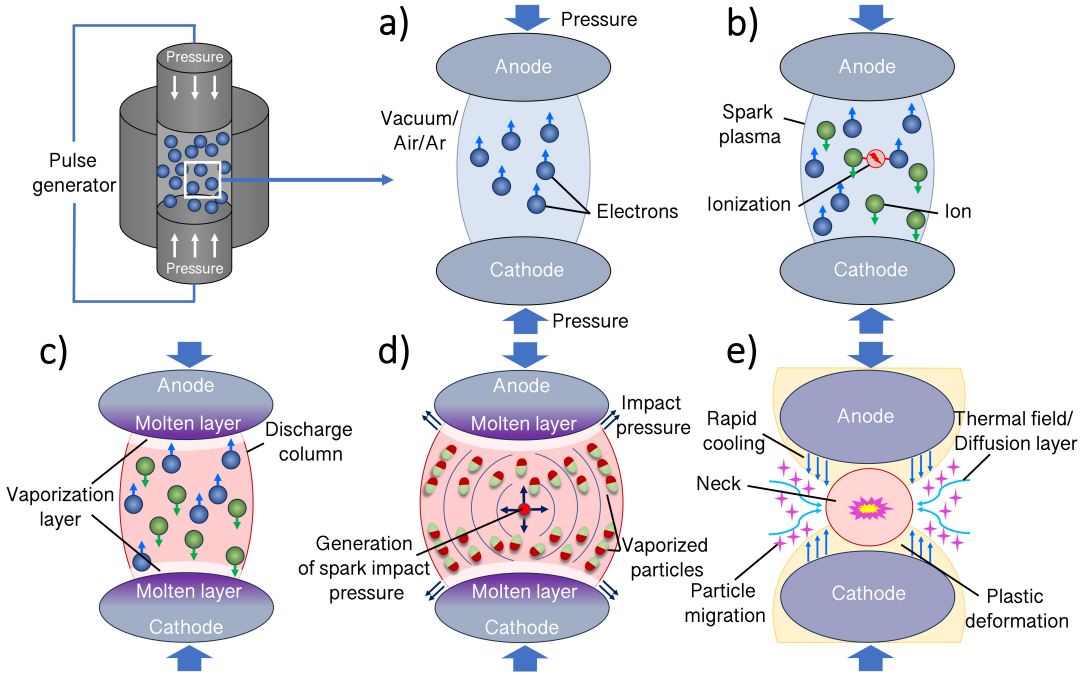

Figure 2.9: Mechanism behind formation of spark plasma and necking. Figure inspired by [67].

The mechanisms during SPS include multiple fields simultaneously, affecting the microstructure and properties of the spark plasma sintered material. The stress field is caused by both the uniaxial pressure and the thermal expansion from the samples and the die. The thermal field is introduced by the heating mechanisms present, namely Joule heating, electrical discharges and high-temperature plasma. The electric field is activated by the external voltage from the pulsed direct-current generator. The effects and interaction between the different forces are highly dependent on sample and die material, and a deeper understanding of the complete process remains to be further explored.

SPS facilitates high heating rates, up to 1000 °C/min, where newly formed grain boundaries at the initial sintering stage will not have sufficient time to reach their equilibrium structures. Grain growth is consequently inhibited [66]. Also, using SPS enables use of lower sintering temperatures. The sintering mechanisms evaporation-condensation diffusion, surface diffusion and plastic flow are activated, which are kinetically faster than those of conventional sintering, where grain boundary diffusion is dominating. As a result, consolidation of heat-resistant bulk materials is possible. Another advantage utilizing SPS is the shorter holding time at elevated temperatures. Normally, a maximum of 15 min is enough for reaching the desired density for SPS. The short processing time lowers production costs and can prevent undesired reactions or phase transformations from occurring, profitable for sintering temperature sensitive, hard-to-sinter, nanocrystalline and metastable materials [68, 66].

Castillo et al. (2018) utilized SPS sintering of Al-doped LLZO. The powder compacts were heated to 1050 °C for 10 min, and a uniaxial pressure of 75 MPa was applied. An ionic conductivity of 0.9 x 10^{-4} S/cm was achieved [42]. Another study by Zhu et al. (2023), where SPS was used as a consolidation process, resulted in an ionic conductivity of 2.6 x 10^{-4} S/cm using a temperature of 1100 °C for 10 min and applied uniaxial pressure of 40 MPa [43]. In both studies, a heating rate of 100 °C/min was employed, and graphite was used as die and punch material. Hence, the method seems promising for achieving the necessary properties of Al-doped LLZO for use as solid-state electrolytes.

2.7 Electrochemical properties

Electrochemical impedance spectroscopy (EIS) is a common technique used to evaluate electronic properties. In EIS, the impedance is determined by application of a low-amplitude sinusoidal potential across a range of frequencies, typically 10^{-2} to 10^{7} Hz [69]. Since some ceramic materials possess dielectric properties, the application of direct current (DC) would cause polarization at the electrode-electrolyte interface and/or at the phase boundaries of the material. To avoid this effect and obtain accurate electronic measurements, an alternating current (AC) is applied during the procedure [70].

The impedance is defined as the ratio between the voltage input signal and the phase-shifted current response signal, and describes the material's ability to resist a flow of alternating current. Unlike resistance, which is only applicable to ideal resistors, impedance measurements accounts for non-ideal behavior of resistors like ceramic solid-state electrolytes. Resistance measurements are limited to ideal resistors that exhibit three characteristics: (i) materials obeying Ohm's law across all current and voltage magnitudes, (ii) possessing frequency-independent resistance, and (iii) producing a current response that aligns with the applied voltage in terms of phase. Hence, the electrochemical properties of the material must be determined by impedance.

The results from EIS facilitates the ability to distinguish between and identify the bulk and grain boundary components, as well as give an approximation of the overall resistance in the sample [71]. In equation 2.10, the impedance is represented as a complex number, where $Z(\omega)$ is the impedance of the material, ω is the radial frequency, E is the applied voltage over time t, I is the sinusoidal current response, E_0 is the voltage amplitude of the signal, I_0 is the current amplitude, Z_0 is the impedance magnitude and ϕ is the phase shift.

$$Z(\omega) = \frac{E}{I} = \frac{E_0 \exp(i\omega t)}{I_0 \exp(i(\omega t - \phi))} = Z_0 \exp(i\phi) = Z_0 (\cos(\phi) + i\sin(\phi)) = Z' + Z'' \tag{2.10}$$

These values are often utilized to construct a Nyquist-plot, where the real part (Z'), representing the resistance, is plotted against the imaginary part (Z"), which denotes the magnitude. Each point on the plot represents the impedance of the material at a specific frequency, with higher frequencies displayed towards the left. Semicircles are commonly seen in Nyquist-plots, and the resistance of the different contributions can be found by assessing the intersection between the semicircles and the real axis. Figure 2.10 presents a typical Nyquist-plot with two semicircles, one representing the bulk resistance at high frequencies and the other one depicts the grain boundary resistance at lower frequencies. The following tail in the plot is a response of the electrode connected to the material.

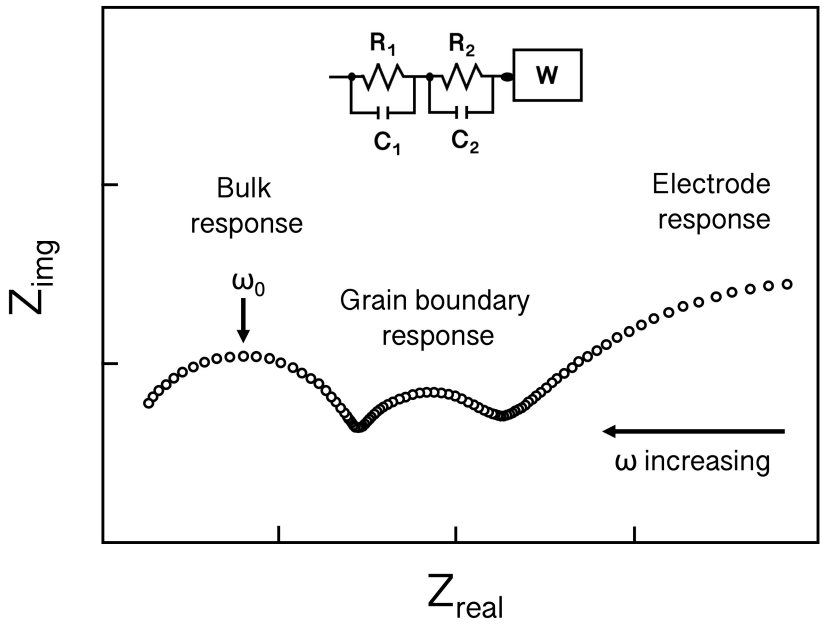

Figure 2.10: Illustration of a typical Nyquist-plot, where the real part of the impedance is plotted on the x-axis, the imaginary part is plotted on the y-axis, scaled equally. Figure inspired by [72].

To investigate the activation energy of ionic conductivities of materials, EIS measurements can be conducted through a specific temperature range. The results can then be plotted in an Arrhenius plot to find the activation energy and the pre-exponential factor, also to investigate the thermal stability [70]. The inverted temperature is plotted against the conductivity at the respective temperature, σ_T, which is commonly done by using Equation 2.11,

$$\ln\sigma_T = \ln A + \frac{-E_a}{kT} \tag{2.11}$$

where A is pre-exponential factor, E_a is the activation energy, k is the Boltzmann constant and T is the temperature corresponding to σ_T. The pre-exponential factor is obtained from the interception with the y-axis in the Arrhenius plot, and represents the frequency of collisions between reactant molecules, as well as determines the rate of reaction at high temperatures. The activation energy can be found from the slope of the linear interpolation of the measurements, and represents the minimum energy required for a reaction to occur. Activation energies for Al-doped LLZO are commonly between 0.3 to 0.4 eV, highly dependent on synthesis method, density and composition. Ionic conductivities and activation energies for lithium diffusion from literature are displayed in Table 2.2 .

3 Experimental

3.1 Chemicals and apparatus

Chemicals utilized during synthesis of precursor solutions are listed in Table 3.1. The compositions of final precursor solutions are described in Section 3.2.1. Apparatuses employed throughout the work are depicted in Table 3.2.

Table 3.1: Chemicals used during thesis work.

Chemical	Formula	State	Purity	Manufacturer
Lanthanum nitrate	$La(NO_3)_3$	aq	$\geq$ 99%	Lehmann & Voss
Zirconyl nitrate	$ZrO(NO_3)_2$	aq	99.9%	Lehmann & Voss
Lithium nitrate	$LiNO_3$	s	$\geq$ 99%	Rodachem
Aluminum nitrate	$Al(NO_3)_3 \cdot 9H_2O$	s	$\geq$ 99.5 %	Emplura
Ethanol	C_2H_5OH	l		
Isopropanol	$(CH_2)_2CHOH$	l		
Synthetic air	80% N_2 and 20% O_2	g	5.0	Linde Group

Table 3.2: Apparatuses used during thesis work.

Purpose/Measurement	Apparatus	Model
Thermal decomposition	DSC/TG	Netzsch STA449 Jupiter TGA Hugin
Microstructure	SEM/EDS	Hitachi S3400N
Gold sputtering	Gold coater	Edwards Sputter Coater S150B
Carbon sputtering	Carbon coater	Cressington 208 Carbon
Phase identification	XRD	Bruker D8 A25 DaVinci
Phase identification	HT XRD	D8 Focus
Calcination & sintering	Furnace	Nabertherm muffle furnace
Drying	Furnace	Termaks TS8136
Drying	Rotavapor	BUCHI Rotary evaporator R-210
Milling of powder	Ball mill	US Stoneware 764 AVM
Pressing	Uniaxial pressing	C-press
Pressing	Cold isostatic pressing	Autoclave Engineers CIP22260
Sintering	SPS	Dr Sinter SPS-825
Dry polishing	Polishing machine	Struers LaboPol-21
Diamond suspension polishing	Polishing machine	Struers Tegramin-20
Ionic conductivity	Potentiostat	Solartron ModuLab XM ECS

3.2 Procedure

A flow chart of the experimental work is shown in Figure 3.1. Analytical methods are shown in blue. All powders and pellets were stored in a desiccator to minimize contact with moisture.

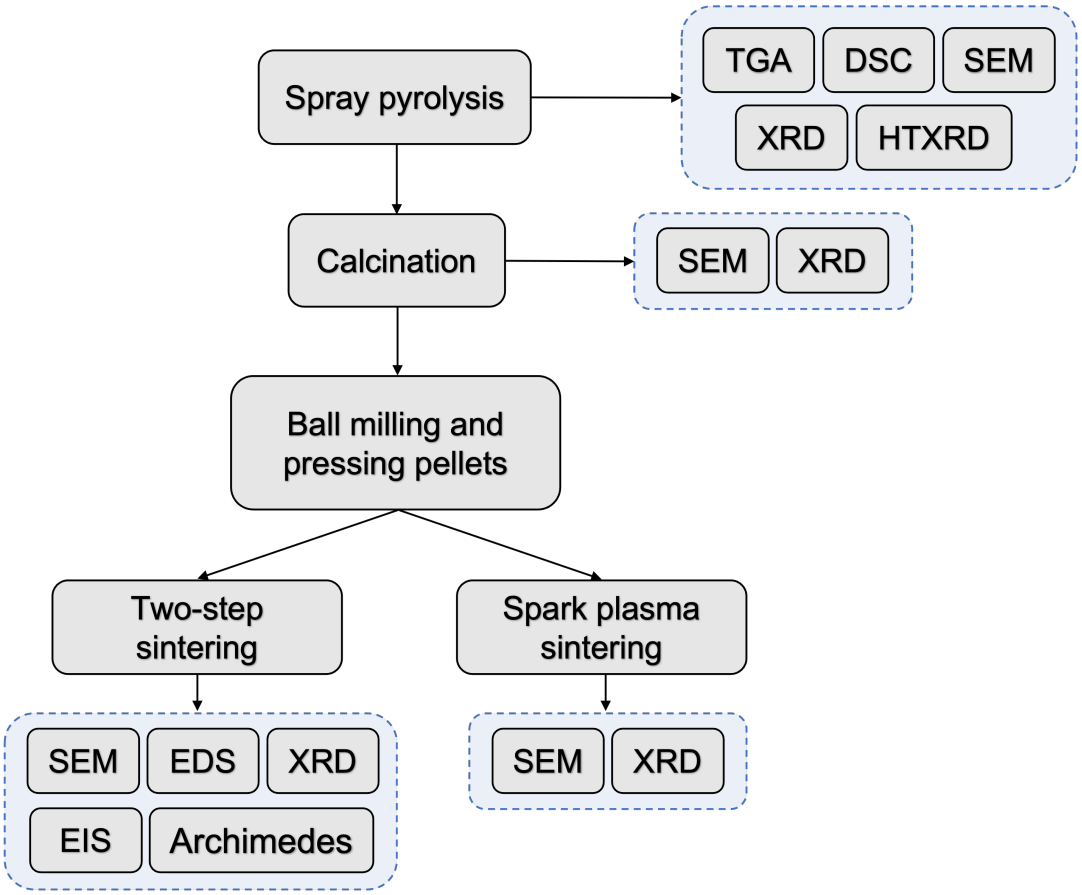

Figure 3.1: Flow chart illustrating conducted activities. Analytical methods shown in blue.

3.2.1 Spray pyrolysis

Two powder precursors of different Li excess (24.2 and 17 mol%) of $Li_{6.25}Al_{0.25}La_3Zr_2O_{12}$ were synthesized by spray pyrolysis at CerPoTech AS (Trondheim, Norway) with stoichiometry as shown in Table 3.3. The setup for the spray pyrolysis process is illustrated in Figure 3.2. Precursor solutions were synthesized using the nitrates displayed in Table 3.1. $Al(NO_3)_3$(s) was dissolved in deionized water at a concentration of $\sim$ 1.3 mmol/g two days before the spraying. $LiNO_3$(s) was dissolved in deionized water the same day as the synthesis reaching a concentration of $\sim$ 3.7 mmol/g. $La(NO_3)_3$ and $ZrO(NO_3)_2$ solutions were used as-recieved.

Table 3.3: Stoichiometry and nomenclature of compositions with respectively 17 and 24.2 mol% Li excess from nominal composition, $Li_{6.25}Al_{0.25}La_3Zr_2O_{12}$.

Composition	Stoichiometry	Nomenclature
1	$Li_{7.31}Al_{0.25}La_3Zr_2O_{12}$	17-LALZO
2	$Li_{7.76}Al_{0.25}La_3Zr_2O_{12}$	24,2-LALZO

Table 3.4 displays concentrations of the nitrate precursor solutions utilized during the synthesis. Stoichiometric amounts and masses of solutions for achieving the nominal compositions shown in Table 3.3 are also displayed. Concentrations of $La(NO_3)_3$ (aq) and $ZrO(NO_3)_2$ (aq) were determined by thermogravimetric calibration, where an exact quantity of the precursor solution was thermally decomposed to oxides at temperatures above 500 °C (La_2O_3) and 400 °C (ZrO_2). The oxide masses were determined to calculate the mole of cations per unit mass of solution. The mass calculations were based on the precursor concentrations and stoichiometric amounts for attaining the final compositions.

The two precursor solutions were based on the nominal stoichiometries displayed in Table 3.3. The beakers containing $LiNO_3$(aq) were used to prepare the precursor solutions. The nitrate solutions were added in the following order: $La(NO_3)_3$, $ZrO(NO_3)_2$ and $Al(NO_3)_3$, based on mass of solutions from highest to lowest. The precursor solutions were mixed by magnetic stirring for 30 min before the spray pyrolysis. The order of spraying was based on the amount of Li excess, starting with the composition of lowest Li surplus. The tube furnace was sprayed with deionized water between each spraying to minimize contamination from previous samples.

Table 3.4: Calculated quantity of nitrate solutions used for synthesis of precursor solutions.

Composition	Solution	State	Conc. [mmol/g]	Mass solution [g]	Stoich. amount [mol]	Excess Li [mol%]
1	$LiNO_3$	aq	3.7	299.65	4.34	17
2	$LiNO_3$	aq	3.7	318.10	4.61	24.2
1, 2	$Al(NO_3)_3$	aq	1.3	112.03	0.15	-
1, 2	$La(NO_3)_3$	aq	1.7	1052.09	1.78	-
1, 2	$ZrO(NO_3)_2$	aq	0.25	561.34	1.19	-

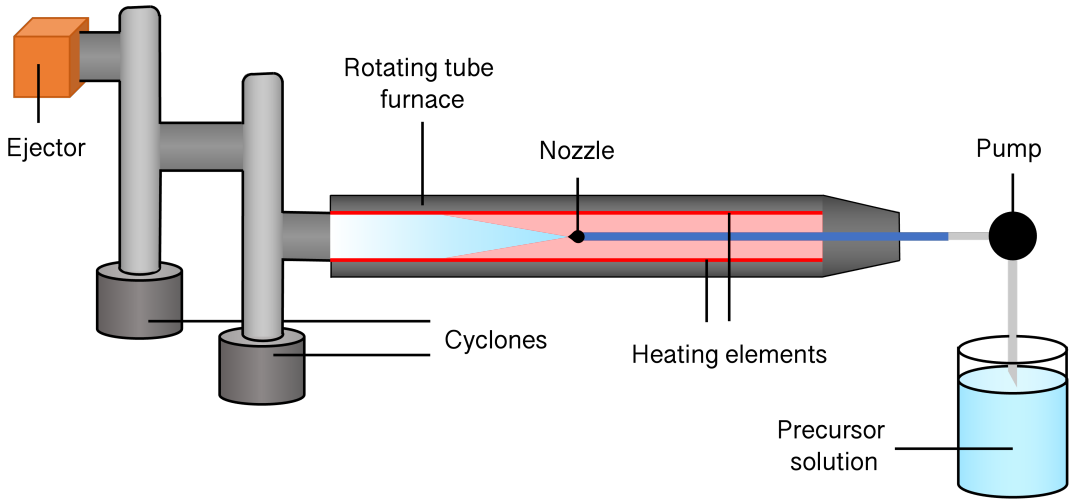

Figure 3.2: Schematics of equipment and setup utilized during spray pyrolysis.

3.2.2 Calcination

The precursor powders were calcined in order to produce single phase cubic LALZO. The powders were calcined in MgO crucibles with lids to avoid furnace-induced contamination, in ambient air at a temperature of 750 °C with holding time of 6 h. Only one composition was calcined at a time. Heating and cooling rates were 200 °C/h. The selection of calcination conditions were based on prior work conducted by Herskedal and Eriksen [73, 25]. The masses of the powders were measured both before and after calcination. Description of the crucible utilized can be found in Table 3.5.

Table 3.5: Crucibles used during thesis work.

Treatment	Crucible material	Shape	d_{inner} [mm]	d_{outer} [mm]	Height [mm]	V_{inner} [cm^3]
Sintering	MgO	Cylindrical	22.6	24.8	49.9	19.1
Calcination	MgO	Square	90.2	99.2	25.6	208.1

3.2.3 Ball milling and drying

The calcined powders were ground by wet ball milling in order to reduce particle size and promote particle homogenization, while also breaking up agglomerates. The powder was mixed with 400 mL yttria stabilized zirconia (YSZ) balls (d = 6 mm) and 300 mL isopropanol in 1000 mL polyethylene (PE) flasks (d = 9 cm). The rotation speed was maintained at approximately 60 % of the critical milling speed, and the process was carried out for a period of 24 h. The isopropanol was subsequently removed by a rotavapor, and the resulting product was further dried in a furnace at 100 °C for 1 h to eliminate residual humidity. The milling and drying procedure is presented in Figure 3.3.

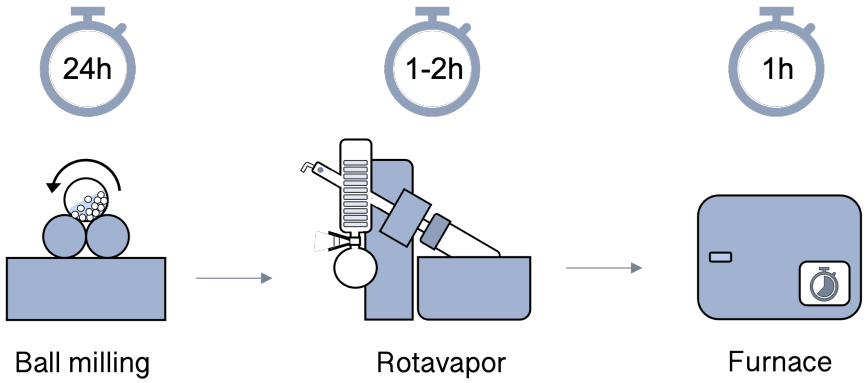

Figure 3.3: Procedure for milling and drying of calcined powders.

3.2.4 Pellet preparation

Milled powder was ground gently in a morter and thereafter sieved using a 250 µm grit sieve to achieve a fine powder with narrow agglomerate size distribution. Green bodies were then produced by double-action uniaxial pressing at $\sim$ 2 MPa. To ease removal of pellets after pressing, stearic acid was applied to the pressing tools. Subsequently, the pellets were isostatically pressed by cold isostatic pressing (CIP) to enhance the density. The pellets were placed in latex gloves which was evacuated prior to pressing. Hydrostatic pressure applied during CIP was set to 200 MPa with a holding time of 1 min. Pellet diameter and thickness after pressing were measured to approximately 9.5 mm and 1.8 mm, respectively.

3.2.5 Two-step sintering

Pressed pellets were sintered utilizing two-step sintering (TSS) in ambient air. The samples were placed in alumina crucibles with the calcined powder of 24.2 mol% Li excess as powder bed (PB) to avoid Li loss, as shown in Figure 3.4a. The mass ratio between the powder bed and pellet was 2:1 (PB-ratio = 2). Description of the crucible utilized is displayed in Table 3.5.

Different temperatures and holding times were investigated to maximize relative densities and minimize abnormal grain growth of the pellets. The temperature programs, listed in Table 3.6 with parameter descriptions in Figure 3.4b, had an initial heating rate of 200 °C/h from RT to 700 °C. Subsequently, the heating rate was elevated to 800 °C/h over the temperature range of 700 °C to T_1. The cooling rate from T_1 to T_2 was 800 °C/h, which was decreased to 200 °C/h from T_2 to 200 °C. After cooling down to 200 °C, the crucible was removed from the furnace and placed in a desiccator to avoid exposure to moisture while cooling down. Relative densities were determined by Archimedes' method in isopropanol.

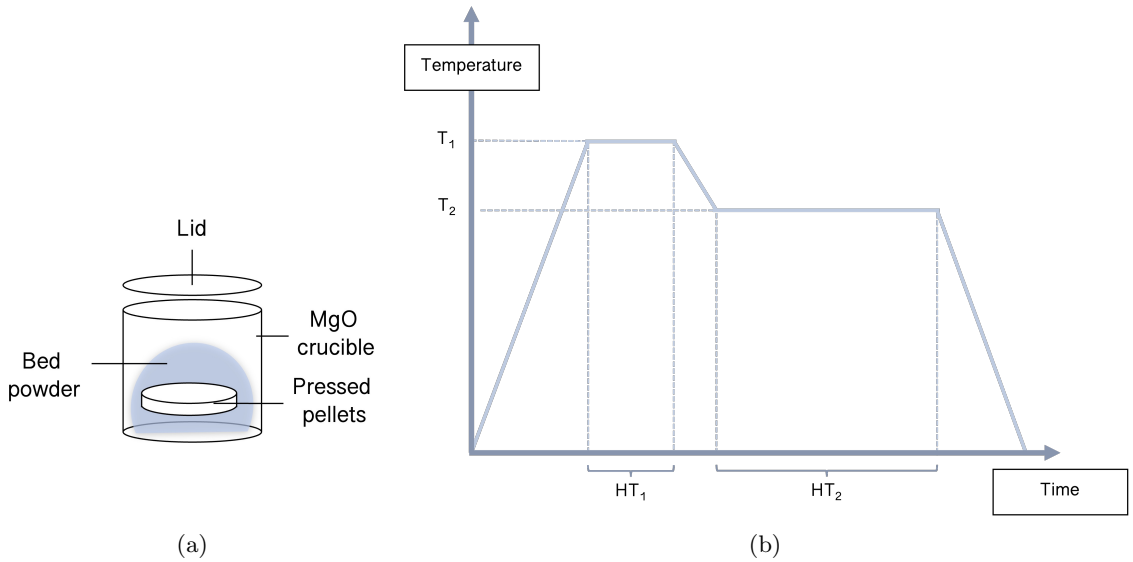

(a) (b)

Figure 3.4: Setup of crucible with powder bed (PB-ratio = 2) shown in a), description of two-step sintering parameters shown in b).

Table 3.6: Temperature programs for two-step sintering of 24,2-LALZO and 17-LALZO. HT = holding time, T = temperature, RD = relative density. Analyses of samples are displayed.

Nomenclature	T_1 [°C]	HT_1 [min]	T_2 [°C]	HT_2 [h]	XRD	SEM	Archimedes'	EIS
TSS-1 (1000/0.5)	1150	10	1000	0.5	×	×	×	×
TSS-2 (1000/6)	1150	10	1000	6	×	×	×	
TSS-3 (1020/0.5)	1150	10	1020	0.5	×	×	×	
TSS-4 (1050/0.5)	1150	10	1050	6	×	×	×	

3.2.6 Spark plasma sintering

Spark plasma sintering was conducted on calcined powder. Three samples of 17-LALZO were sintered, described in Table 3.7. The powder was placed in a graphite die to provide conductivity during operation. The setup is depicted in Figure 3.5. The inside of a two punch graphite die (d_{inner} = 12 mm) was covered with graphite foil before one of the graphite punches was inserted. The punch was lined with graphite foil on the contact surface, and calcined powder was placed on top. The die was cautiously shaken to achieve an even distribution of the powder. Graphite foil was placed on top of the powder before the second graphite punch was placed in the die. Uniaxial pressing was utilized for stabilizing and aligning the powder with the pyrometer measurement hole.

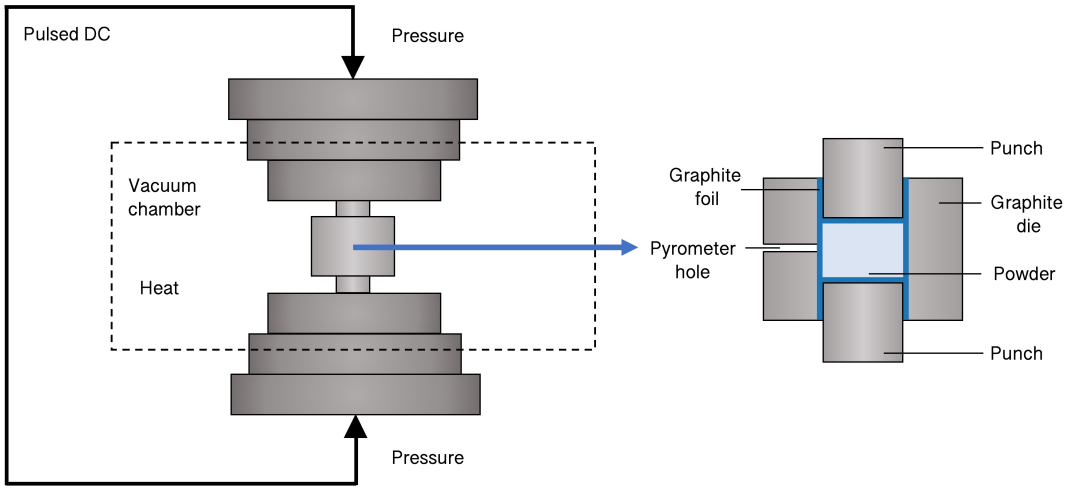

Figure 3.5: Setup of the SPS procedure.

Table 3.7: Nomenclatures and masses for SPS of calcined 17-LALZO powder. Analyses of samples are displayed.

Nomenclature	Composition	Mass [g]	XRD	SEM
SPS-1 (0.35)	17-LALZO	0.35		
SPS-2 (0.4)	17-LALZO	0.4		×
SPS-3 (0.7)	17-LALZO	0.7	×	×

Before the die was placed in the SPS, a layer of graphite felt (t = 20 mm) was applied surrounding the setup to reduce heat loss during the process. Three graphite discs were then placed in the window to align the sample with the hole for temperature measurements. The die with the sample was placed symmetrically with the electrodes on top of the discs, and three additional graphite plates were placed onto the die. The chamber was evacuated to 25 MPa and the sintering program displayed in Figure 3.6 was used. The heating and cooling rates were 100 °C/min. The sample was first heated to 900 °C, followed by an increase in uniaxial pressure to 50 MPa. Subsequently, the temperature was raised and maintained at a maximum temperature of 1000 °C for 5 min, after which it was reduced to 900 °C. The pressure was then lowered to 25 MPa, followed by further cooling until reaching RT.

To remove the sample from the die, a uniaxial press was utilized. The graphite foils were attempted removed by using SiC paper, but as the pellets were not coherent, the attempts on removal were cancelled and analytical measurements were conducted with the graphite foil present.

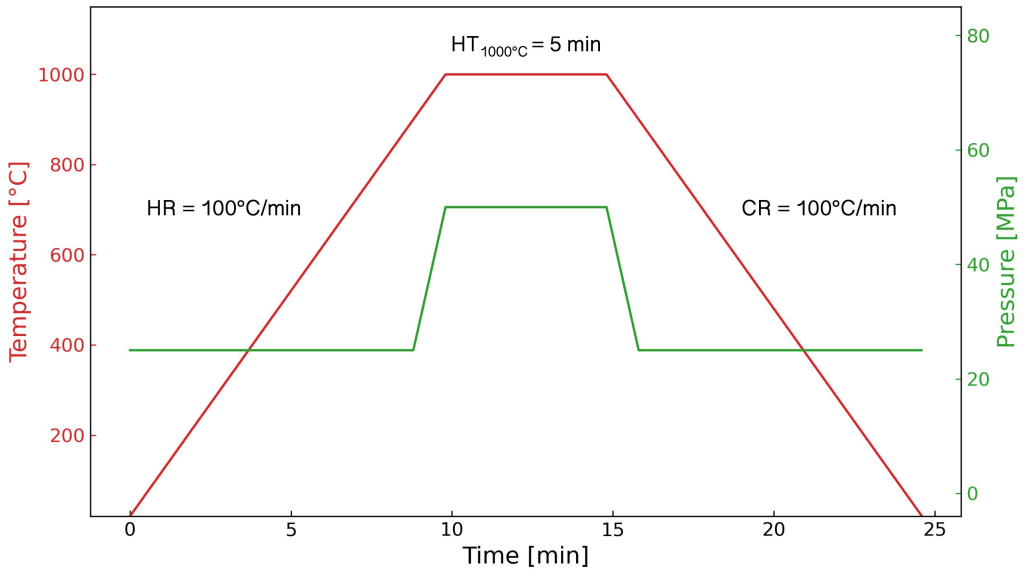

Figure 3.6: Program for spark plasma sintering of calcined powder. Temperature (red) and uniaxial pressure (green) displayed as a function of time. HT = holding time, HR = heating rate, CR = cooling rate.

3.2.7 Thermogravimetric analysis

Thermogravimetric analysis (TGA) and differential scanning calorimetry (DSC) were conducted in synthetic air on the precursor powders. A maximum temperature of 1250 °C and heating/cooling rates of 10° C/min were used. The holding time at maximum temperature was 1 h. Samples 24,2-LALZO and 17-LALZO were placed in Al_2O_3 crucibles with lids to avoid contamination, with a small hole to release exhaust gas developed during heating. Sample masses were measured prior to the analysis with an accuracy of 0.0001 g, and were used in the program to calculate percentage mass loss.

3.2.8 Scanning electron microscopy and element analysis

Powder morphology and pellet microstructure were investigated by scanning electron microscopy (SEM). Imaging was done by using secondary electrons (SE) and back-scattered electrons (BSE) with 15 kV accelerating voltage, 30 µm aperture and a working distance of 5 to 10 µm. Precursor powders and calcined powders were distributed on carbon tape, and gold sputtered to provide conductivity. Sintered pellets were broken in half to study the fracture surface, and were placed on the sample holder with conducting aluminium tape surrounding the samples. Polished sintered pellets were coated with carbon and surrounded with aluminium tape for conductivity.

3.2.9 X-ray diffraction

The phase compositions were characterized by X-ray diffraction (XRD) at both ambient conditions and elevated temperatures, using diffractometers with Bragg-Brentano geometry. The radiation source was Cu Kα with wavelength $\lambda = 1.54$ Å. The collection range was determined to $2\theta \in [10°, 75°]$ for RT measurements with fixed divergence slit 0.2°. Precursor powders, calcined powders and milled sintered pellets were prepared in standard sample holders and scanned within 120 min after sample preparation to minimize exposure to moisture in air.

High-temperature XRD (HT XRD) was conducted on precursor powder of composition 24,2-LALZO to investigate the change in phase composition with increasing temperature. Collection range determined was $2\theta \in [15°, 70°]$ with primary and secondary Soller slits 2.5°. The precursor powder was placed in a sample holder made of alumina. Reaction between the powder and the alumina will not occur as the scanning temperatures are too. The selection of temperatures and scanning rates were based on the results from the thermal analysis, where an unidentified exothermic peak appeared at approximately 500 °C. Hence, scanning was conducted at every 50 °C between 350 and 700 °C with collection time of 20 min. The heating rate between each temperature scan was set to 10 °C/min. Conditions during XRD and HT-XRD are listed in Table 3.8.

Table 3.8: Parameters utilized during XRD and high-temperature XRD.

Parameter	XRD	HT-XRD
Temperature	RT	350-700 °C
Temperature step		50 °C
Collection time per step	120 min	20 min
Step size	0.0133°	0.0245°
Scan rate	1.47 s	0.53 s

Indexing the different phases in the diffractograms was done by using DIFFRAC.EVA V6 Bruker (AXS) software with the database 2022 PDF-4+. PDF-cards utilized from the database are listed in Table 3.9. Contributions from Kα2 radiation were stripped from the diffractograms prior to extraction of data for all but the precursor powders. Python 3.8.8. was used for plotting diffractograms. All diffraction patterns presented in this work are normalised based on the highest intensity peak.

Table 3.9: PDF-4+ card numbers utilized during analyses of powders and pellets.

Compound	Formula unit	PDF-4+ card number
Al-doped c-LLZO	$Li_{6.22}La_3Zr_2Al_{0.26}O_{12}$	04-024-8262
Pyrochlore	$La_2Zr_2O_7$	01-087-4443
Lithium carbonate	Li_2CO_3	00-022-1141
Lithium nitrate	$LiNO_3$	04-010-5519
Lanthanum nitrate	$La(NO_3)_3$	01-083-4943
Zirconium oxide nitrate	$ZrO(NO_3)_2$	00-049-1062
Lithium aluminum lanthanum oxide	$Li_{0.5}Al_{0.5}La_2O_4$	00-040-1167
Lanthanum aluminum oxide	$LaAlO_3$	04-007-4276
Zirconium oxide	ZrO_2	04-007-0952
Graphite	C	00-056-0159

3.2.10 Archimedes' method

The masses of dry pellets were measured prior to the procedure, and the samples were then placed in an evaporation dish in a desiccator. The samples were evacuated for 30 min. Subsequently, the immersion liquid, isopropanol, was slowly introduced until 3/4 of the evaporation dish volume was filled. To ensure that isopropanol had filled all open pores in the pellet, vacuum was again introduced to the system for 30 min. Thereafter, air was introduced to the desiccator. The pellet masses were measured while still submerged in the immersion liquid, together with the temperature of the isopropanol. Finally, a damp tissue was employed to remove residual isopropanol on the surface of the pellet before the mass was determined. All masses and temperatures of the immersion liquid are included in Appendix F.1.

3.2.11 Electrochemical impedance spectroscopy

The ionic conductivity of the samples with highest relative density was measured by electrochemical impedance spectroscopy (EIS). The sintered pellets were polished by hand with SiC paper (European grit (#800 - #4000)), and subsequently sputtered with Au functioning as blocking electrodes during the measurements. The sides of the pellets were polished after gold sputtering to remove contact between the upper and lower metallic layer. Dimensions of the pellets are listed in Appendix I.1.

The samples were then placed in a two-electrode set-up, and a frequency range of 1 MHz to 100 mHz was utilized. The sinusoidal voltage amplitude was set to 10 mV. Measurements were conducted at both room temperature and at elevated temperatures, with a duration of 3 min for each temperature measurement.

The room temperature measurements were plotted as Nyquist plots, and the EC-lab BioLogic ZFit software was utilized for fitting impedance data with equivalent circuits. Two circuits are displayed in Figure 3.7, where the equivalent circuit in Figure 3.7a considers the resistance contributions from the bulk and the grain boundaries separately. The circuit is accountable for Nyquist plots with two semicircles. The resistors are denoted R_b and R_{GB}, with constant phase elements Q_b and Q_{GB} in parallel. The contributions from the Au blocking electrode is included in the last constant phase element, Q_{BE}. Figure 3.7b displays a model with total response as one resistance, where the bulk and grain boundary resistance are represented by R_{b+GB} with Q_{b+GB} in parallel. The blocking electrode response is included in the last sequence. This equivalent circuit is valid for Nyquist plots with one semicircle.

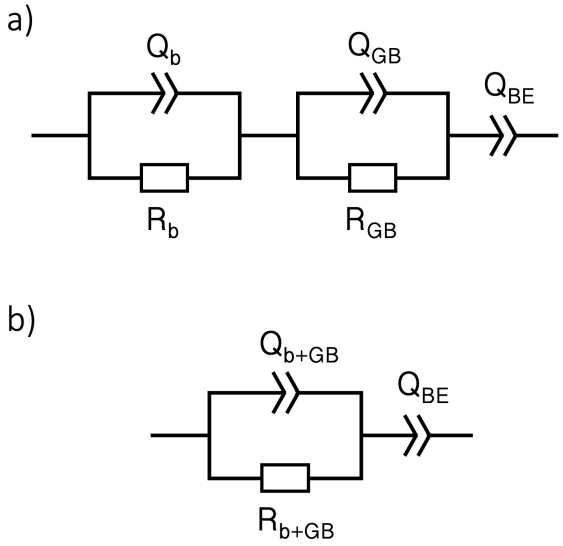

Figure 3.7: Equivalent circuits utilized during fitting of electrochemical impedance measurements in Nyquist diagrams, where R denotes a resistor, Q is a constant phase element, GB represents grain boundary and b is the bulk. Circuit a) is applicable for samples where bulk and grain boundary contributions are separable, while b) is applicable for inseparable resistance contributions.

The EIS measurements for temperatures from 30 to 200 °C included steps of 10 °C. The data was plotted in Arrhenius plots displaying total conductivity as a function of inverse temperature, which was used to find the activation energy and the pre-exponential factor for conductivity of the two materials. The activation energy, E_a, was calculated through Equation 3.1, where R is the gas constant and *slope* is the gradient of the interpolated line.

$$E_a = -\text{slope} \cdot \text{R} \tag{3.1}$$

The pre-exponential factor was found at the interception between the interpolated line and the y-axis. The conductivity for each temperature measurement was estimated by analyzing Bode plots of the individual measurements, which depict conductivity as a function of Z'. The average conductivity of the plateau region in the Bode plots was then calculated and utilized as total conductivity in the Arrhenius plots. The diagrams were plotted using Python 3.8.8.

4 Results

4.1 Precursor powder

4.1.1 Phase composition

Figure 4.1 presents the results from the XRD analysis conducted on precursor powders of compositions 24,2-LALZO and 17-LALZO. Diffraction lines corresponding to LALZO, Li_2CO_3, $La_2Zr_2O_7$, and $LiNO_3$ are observed. Nitrates are dominating for both powders, particularly with sharp and distinct reflections indicating the presence of $LiNO_3$ at 2θ-values 24.82°, 32.21°, 35.37°, and 42.42°. Both 24,2-LALZO and 17-LALZO contain LALZO and $La_2Zr_2O_7$, with the latter as a consequence of lithium deficiency after heat treatments. There are indications of small amounts of Li_2CO_3, evidenced by minor diffraction lines at 2θ-values 31.80° and 39.56°.

Diffraction lines indicating $ZrO(NO_3)_2$ and $La(NO_3)_3$ are marked with green and pink triangles, respectively. Broad reflections appear at 2θ-values $\sim$ 29°, 48° and 56° for the two samples due to a small particle size of $La_2Zr_2O_7$.

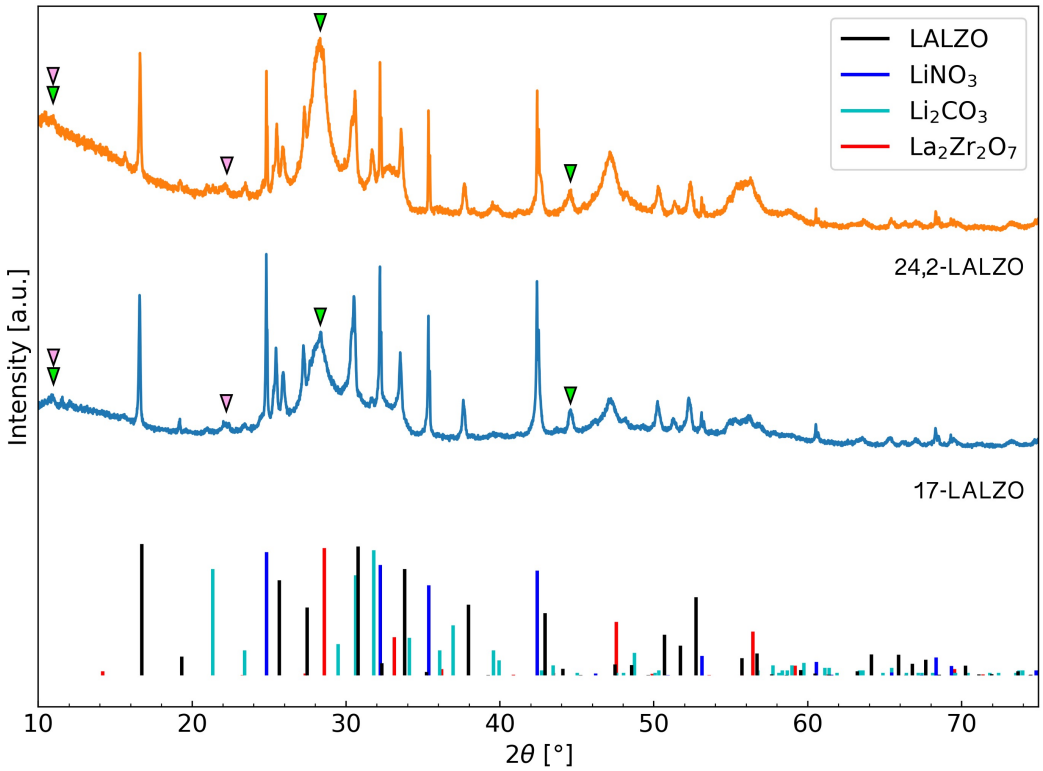

Figure 4.1: X-ray diffractogram of precursor powders 24,2-LALZO and 17-LALZO. Diffraction lines for LALZO, Li_2CO_3, $LiNO_3$ and $La_2Zr_2O_7$ are included. Reflections indicating $ZrO(NO_3)_2$ and $La(NO_3)_3$ are marked with green and pink triangles, respectively.

4.1.2 Thermal analysis

Figure 4.2 displays the thermal decompositions and mass losses during thermogravimetric analysis of precursor powders 24,2-LALZO and 17-LALZO. Mass losses due to surface water and crystal water between RT and 150 °C are not included. The highest mass loss for both samples occurs around the decomposition temperature of $LiNO_3$ at 600 °C [32]. Some loss also occurs around 723 °C, due to decomposition of Li_2CO_3 [32]. During the holding time for precursor powder 24,2-LALZO, decrease in mass is observed due to further decomposition of residual nitrates and Li_2CO_3. Total mass loss during the heat treatment for precursor powder of composition 17-LALZO was measured to approximately 31%, while 45% was measured for 24,2-LALZO. The total mass loss includes measurements from RT to 1250 °C and holding time of 1 h at maximum temperature. The complete TGA is displayed in Appendix C.1.

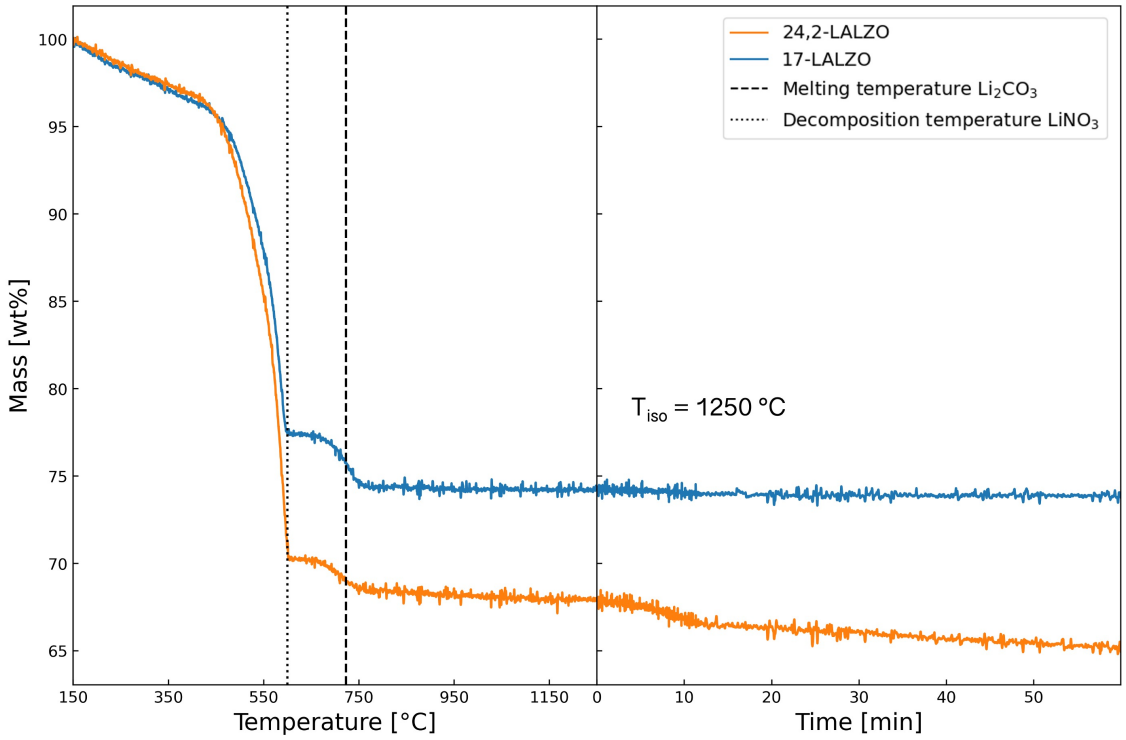

Figure 4.2: TGA of precursor powders between 150 and 1250 °C, with holding time of 60 min at the maximum temperature. Decomposition temperature of $LiNO_3$, $T_d \approx 600$ °C, and melting temperature of Li_2CO_3, $T_m = 723$ °C are displayed as broken lines.

The DSC curves for the precursor powders are depicted in Figure 4.3. Both powders are observed with two endothermic peaks and one exothermic peak. The endothermic peaks appearing at approximately 600 °C correspond with the decomposition temperature of $LiNO_3$, where sample 24,2-LALZO has the highest value. The endothermic peaks above 700 °C are observed close to the decomposition temperature of Li_2CO_3. The exothermic peaks at $\sim$ 500 °C were investigated using HT XRD.

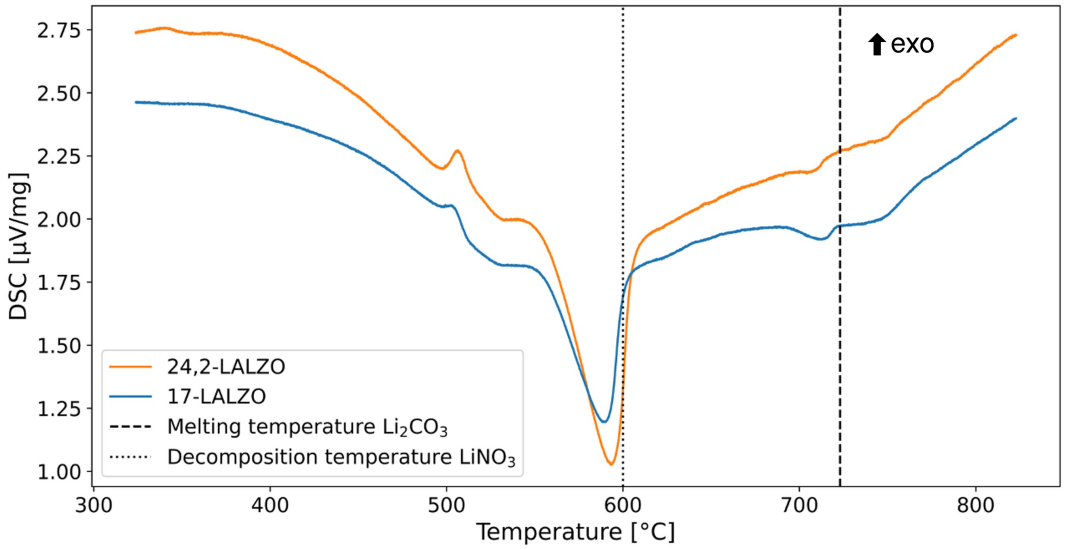

Figure 4.3: DSC of precursor powders between 300 and 850 °C. Decomposition temperature of $LiNO_3$, $T_d \approx 600$ °C, and melting temperature of Li_2CO_3, $T_m = 723$ °C are displayed as broken lines.

4.1.3 High temperature X-ray diffraction

The two-dimensional (2D) presentation of the HT XRD is shown in Figure 4.4, presenting the intensity of diffraction lines for the temperature range 350 to 700° and $2\theta \in [15°, 70°]$. The lines of highest intensity is due to formation of LALZO at 450 °C. $La_2Zr_2O_7$ is present for lower temperatures, observed at 2θ-values 28.59°, 33.13°, 47.55° and 56.43°. At T > 450 °C $La_2Zr_2O_7$ disappears due to reaction with excess Li forming LALZO. Formation and disappearance of low intensity diffraction lines were observed at low 2θ-values and temperatures up to 500 °C, justified by observations in Appendix D.1 of the complete HT XRD for the sample. These low intensity diffraction lines are displayed in Figure 4.5.

In Figure 4.5, three diffractograms are highlighted, corresponding to 700, 450 and 400 °C and $2\theta \in [16°, 30°]$. The scan at the highest temperature (700°C) is included to compare the lower temperature scans with the final composition after the heat treatment. Appearance of two diffraction lines at $\sim 23.4°$ and 24.4° is observed in Figure 4.5, shown in the black frame, indicating formation of $LaAlO_3$ and the intermediate phase $Li_{0.5}Al_{0.5}La_2O_4$ at 450 °C. The remaining reflections in the diffractograms correspond to residual nitrates from the precursor solution. The results from the high-temperature phase identification of 24,2-LALZO are assumed to be valid also for precursor powder 17-LALZO, due to the similar development observed in DSC.

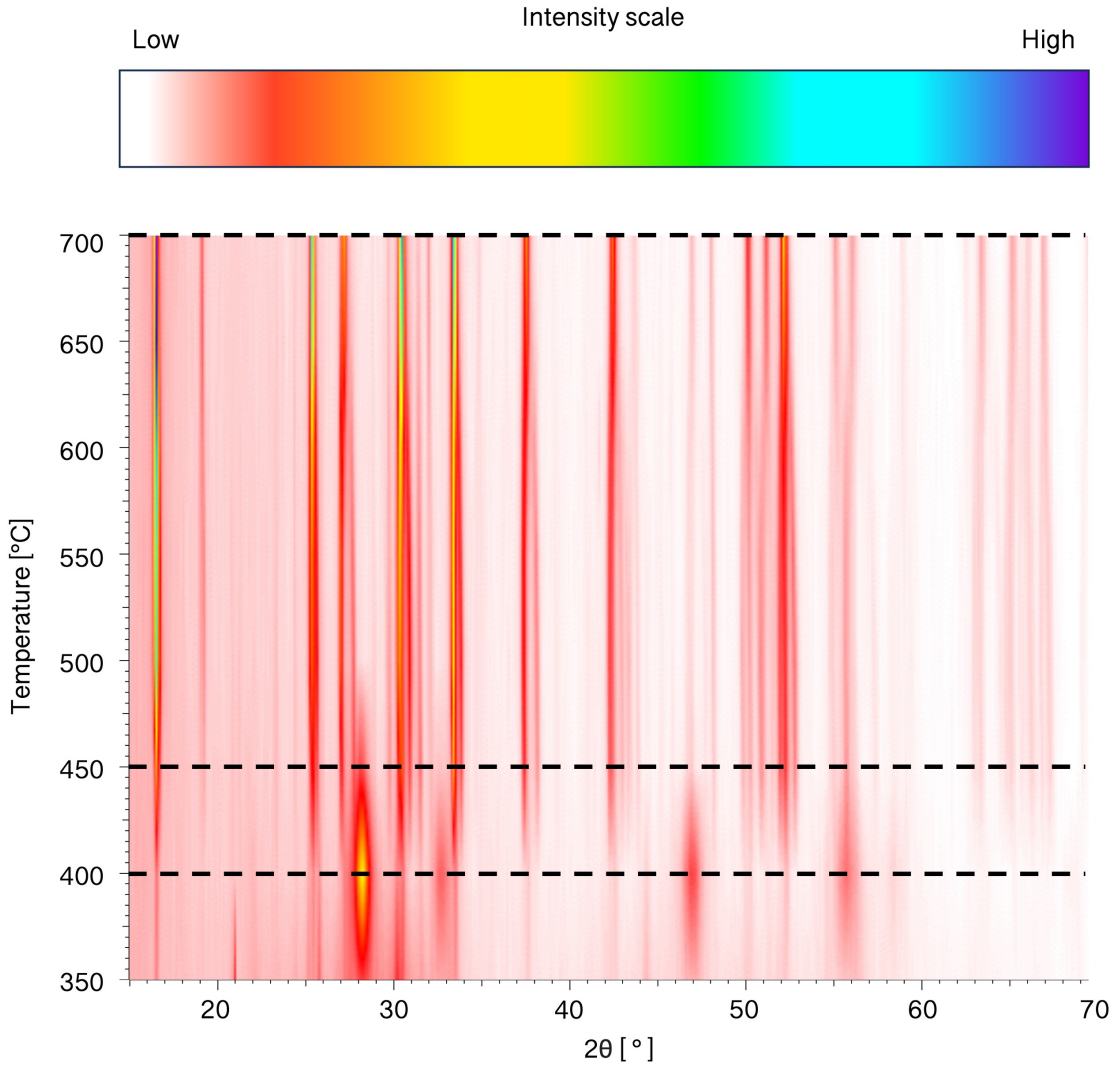

Figure 4.4: Two-dimensional (2D) X-ray diffraction patterns for high-temperature measurements of 24,2-LALZO precursor powder, with temperature range 350 to 700 °C and $2\theta \ \epsilon \ [15°, 70°]$. Diffractograms displayed in Figure 4.5 marked as broken lines. Intensity scale is shown above the diffractogram.

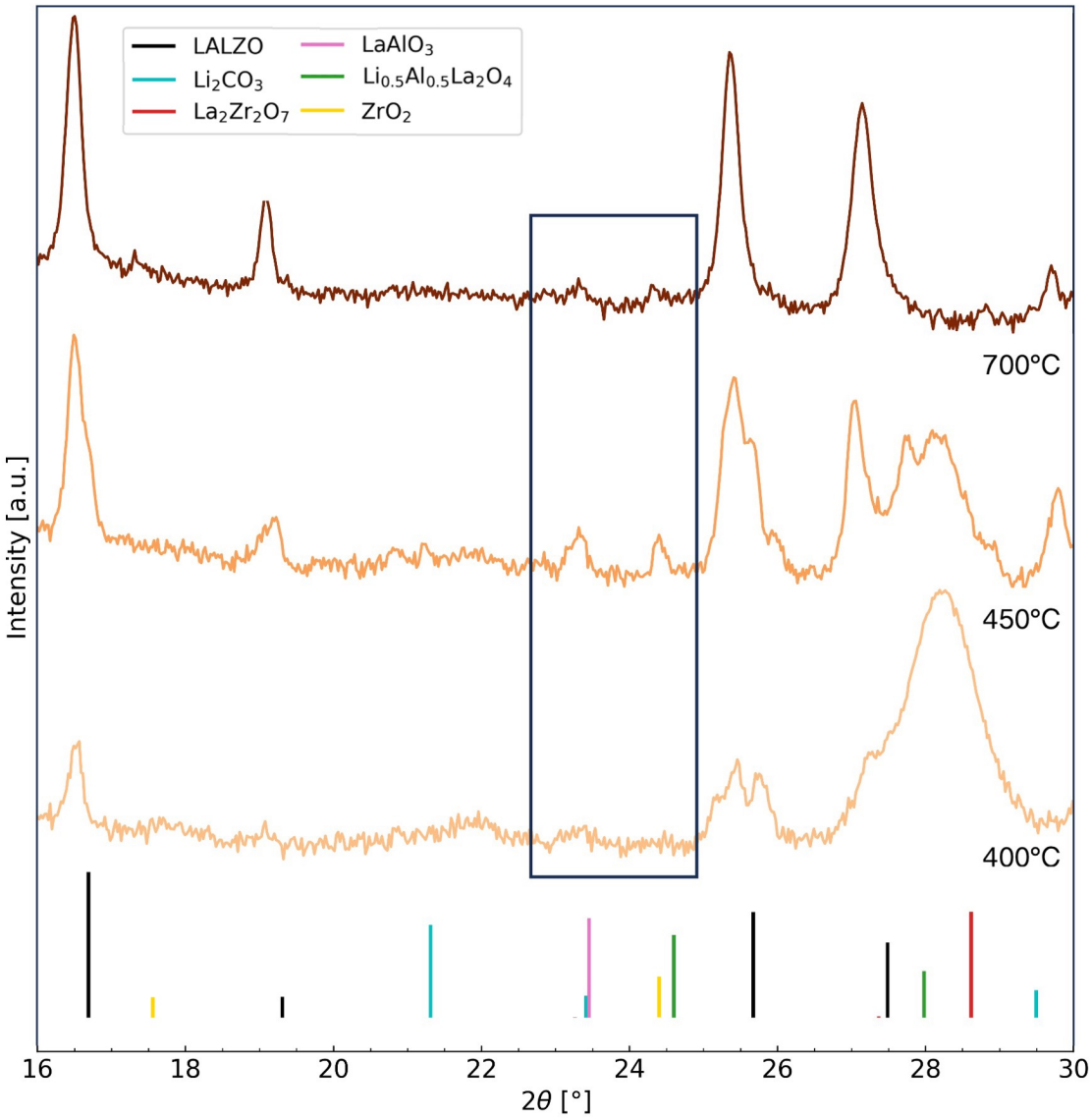

Figure 4.5: High-temperature XRD of 24,2-LALZO precursor powder. Logarithmic scale on y-axis. Diffractograms of 700, 450 and 400 °C are included. Diffraction lines for LALZO, Li_2CO_3, $La_2Zr_2O_7$, $LaAlO_3$, $Li_{0.5}Al_{0.5}La_2O_4$ and ZrO_2 are displayed. The inserted black frame focuses on the formation and disappearance of the secondary phases $Li_{0.5}Al_{0.5}La_2O_4$ and $LaAlO_3$.

4.1.4 Microstructure

SEM of the precursor powders are shown in Figure 4.6. Both powders show similar agglomerate size distribution, as depicted in the images of low magnification in Figures 4.6a and c. The images with higher magnification reveal spherical agglomerates with diameters in the range 5 to 20 µm, shown in Figures 4.6b and d. Agglomerates are fractured due to the spray pyrolysis process, especially prominent for precursor powder 24,2-LALZO in Figure 4.6b.

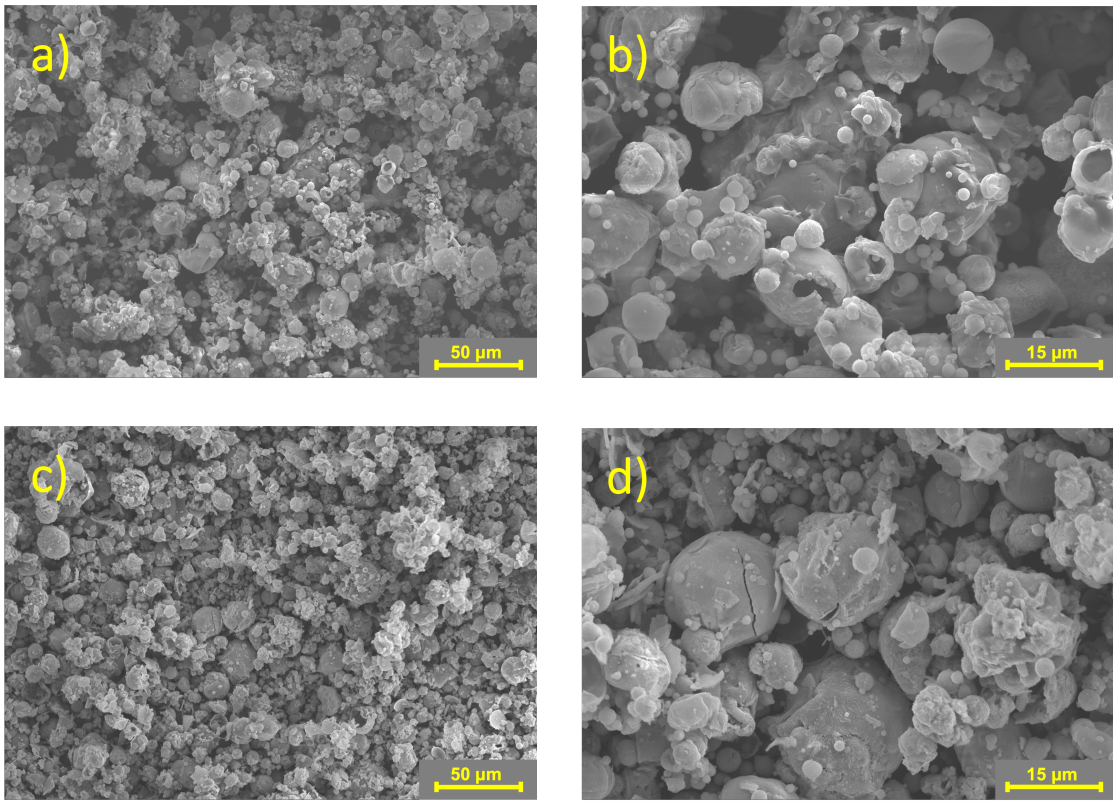

Figure 4.6: Secondary electron micrographs of precursor powders. Agglomerate size shown to the left and higher magnification to the right. 24,2-LALZO displayed in a) and b), 17-LALZO in c) and d).

4.2 Calcined powder

The measured mass losses after calcination of precursor powders at 750 °C for 6 h are displayed in Appendix E.3. 24,2-LALZO showed the highest mass loss with an average of 30.2 % for the calcined batches, while 17-LALZO had an average mass loss of 26.9 %. The decrease in mass occurs due to decomposition of nitrates and removal of surface- and crystal water. The disparity between the powders correlates with the Li concentration.

4.2.1 Phase composition

The phase composition of calcined powders were analysed by X-ray diffraction, shown in Figure 4.7. Li_2CO_3 is observed for both 24,2-LALZO and 17-LALZO at 2θ-values 23.41° and 31.80° due to CO_2 from ambient air. $La_2Zr_2O_7$ is indexed for 17-LALZO, shown for 2θ-value 28.59°, indicating Li-deficiency. Line splitting is observed for composition 24,2-LALZO for all diffraction lines indexed to LALZO, indicating formation of tetragonal phase LALZO. This is highlighted in Figure 4.8 for 2θ-values from 24° to 39°, where the reflection of highest intensity is indexed to c-LALZO, while the two smaller neighbouring diffraction lines are indexed to t-LALZO.

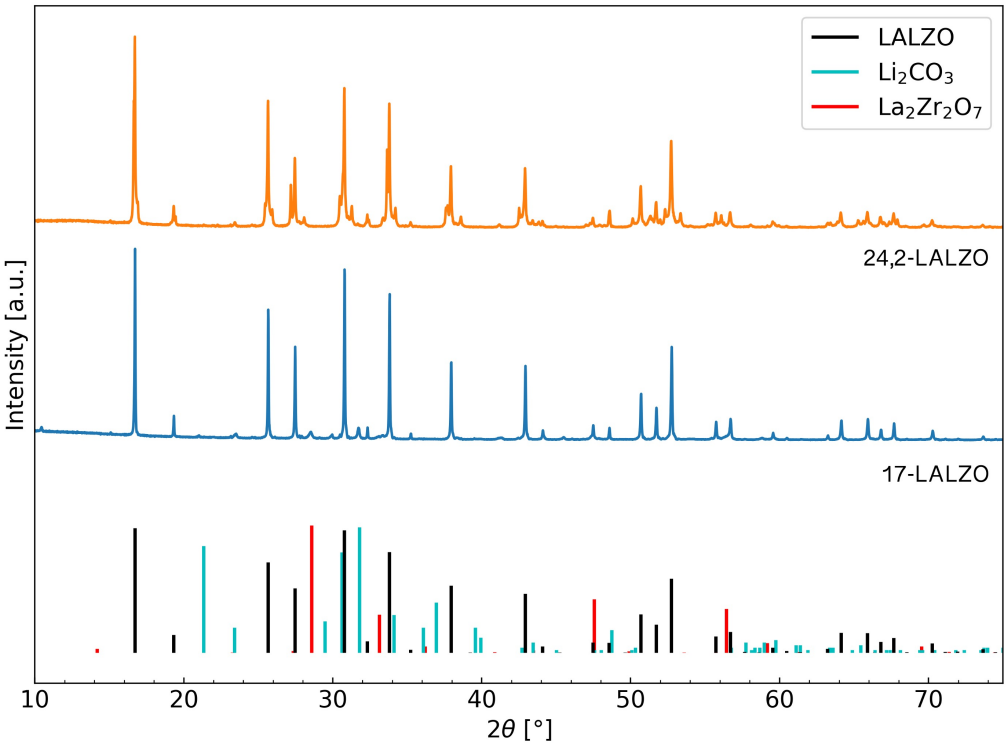

Figure 4.7: X-ray diffractogram of calcined powders. Diffraction lines indicating LALZO, Li_2CO_3 and $La_2Zr_2O_7$ are included.

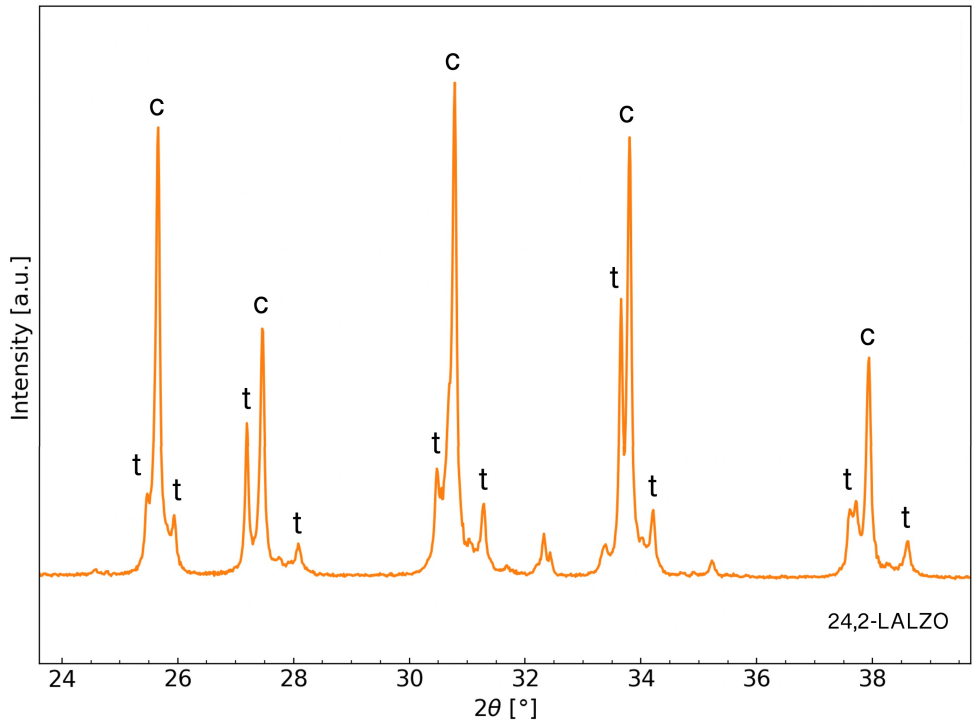

Figure 4.8: Splitting of diffraction lines for calcined 24,2-LALZO powder at 2θ-values between 25° and 39°. Tetragonal and cubic diffraction lines are indicated by t and c.

4.2.2 Microstructure

Microstructures of calcined powders are presented in Figure 4.9. Similar aggglomerate size distribution is observed for 24,2-LALZO and 17-LALZO, shown in Figures 4.9a and c. Spherical agglomerates with size between 5 and 15 µm are observed for both samples, highlighted in Figures 4.9b and d. Agglomerates in 24,2-LALZO are fractured due to the heat treatments.

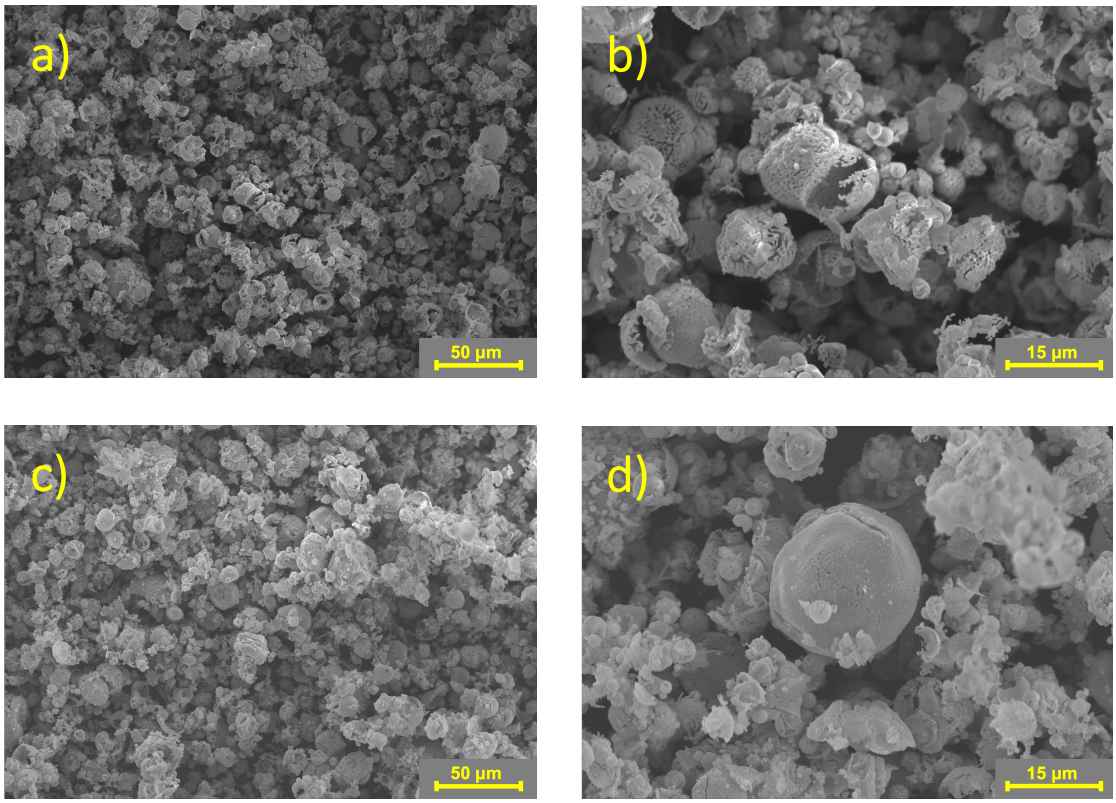

Figure 4.9: Secondary electron micrographs of calcined powders. 24,2-LALZO displayed in a) and b), 17-LALZO in c) and d).

4.3 Two-step sintering

4.3.1 Relative density

Densities of the two-step sintered pellets are presented in Figure 4.10. All relevant measurements and calculations for the displayed values can be found in Appendix F.1. The obtained results reveal that the highest densities were obtained for TSS-1 (1000/0.5) for both compositions, and these samples were subjected to assessment of Li-ionic conductivity by EIS. The 24,2-LALZO pellets exhibit higher densities for all temperature programs, differing from the 17-LALZO pellets between 2.4 and 4.9%. The differences in relative densities for the sintered pellets of composition 24,2-LALZO are less than 2%. For 17-LALZO, the most significant disparity in relative density among the utilized temperature programs is observed between TSS-1 (1000/0.5) and TSS-2 (1000/6), with a difference of 2.2%.

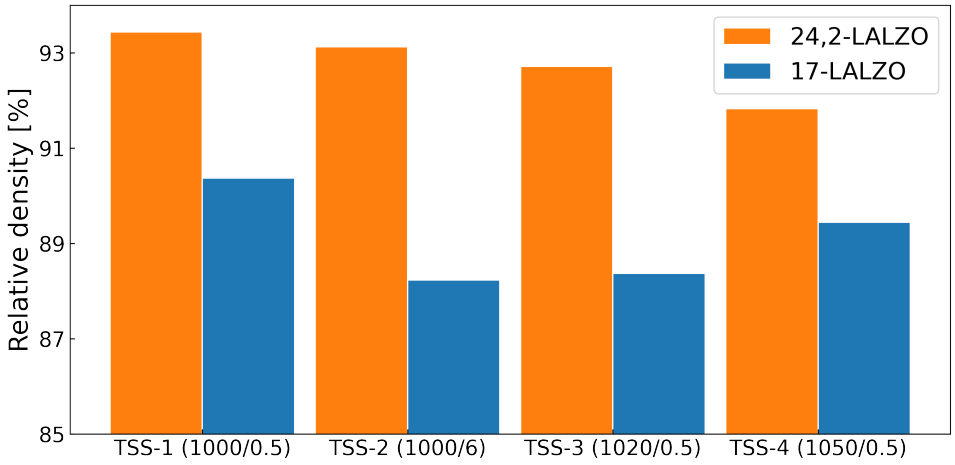

Figure 4.10: Density measurements from Archimedes method for two-step sintered pellets. Temperature programs displayed at the x-axis.

4.3.2 Phase composition

Figure 4.11 displays the X-ray diffractograms for grinded two-step sintered pellets of composition 24,2-LALZO. All scans of the sintered pellets resulted in line splitting for all reflections of LALZO, indicating formation of single phase tetragonal LALZO due to an excess of Li. Broad diffraction lines are observed for 2θ-values above 25° due to small grain size.

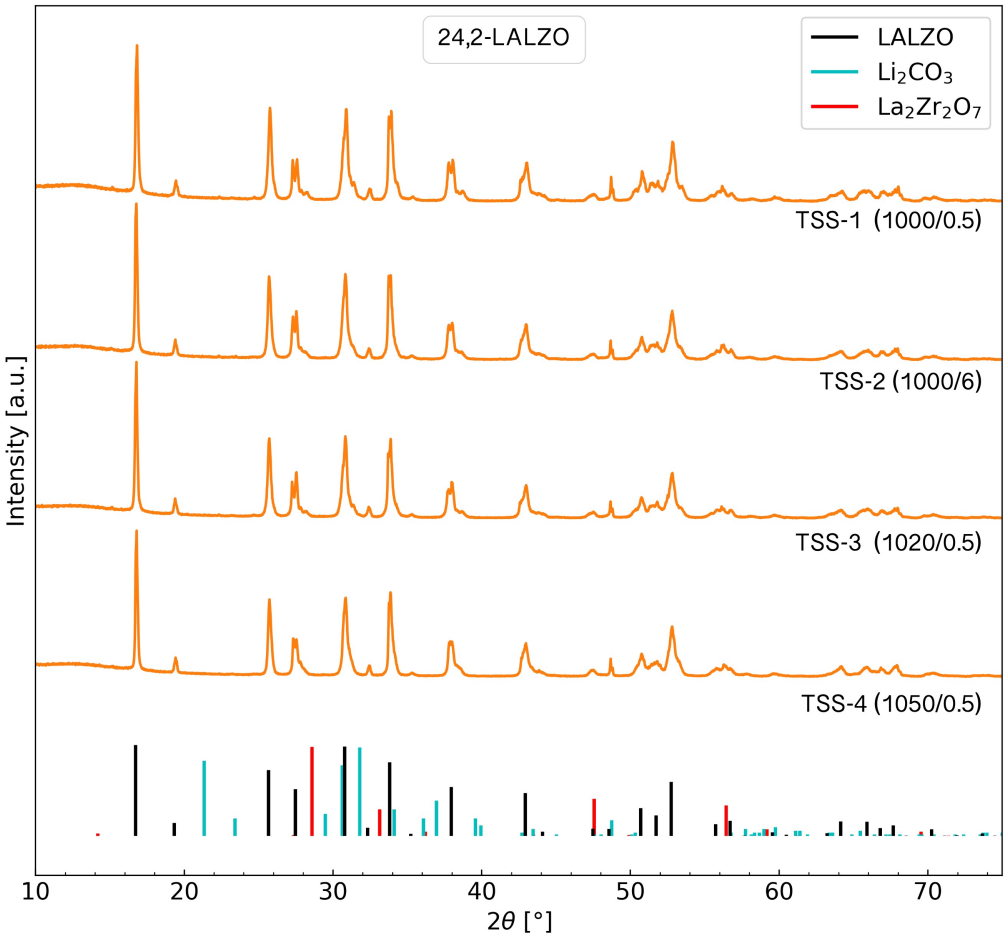

Figure 4.11: Diffraction patterns of two-step sintered pellets of composition 24,2-LALZO. Tetragonal splitting is observed for all samples, as well as wide diffraction lines due to small grains.

Diffractograms for grinded two-step sintered pellets of composition 17-LALZO are displayed in Figure 4.12. TSS-4 (1050/0.5) is identified as single phase c-LALZO, while the other temperature programs gave c-LALZO together with small amounts of secondary phases. For TSS-1 (1000/0.5), TSS-2 (1000/6) and TSS-3 (1020/0.5), small amounts of $La_2Zr_2O_7$ were observed due to Li loss. Also, small reflections observed at 2θ-value 31.80° indicate small amounts of Li_2CO_3 for the respective temperature programs.

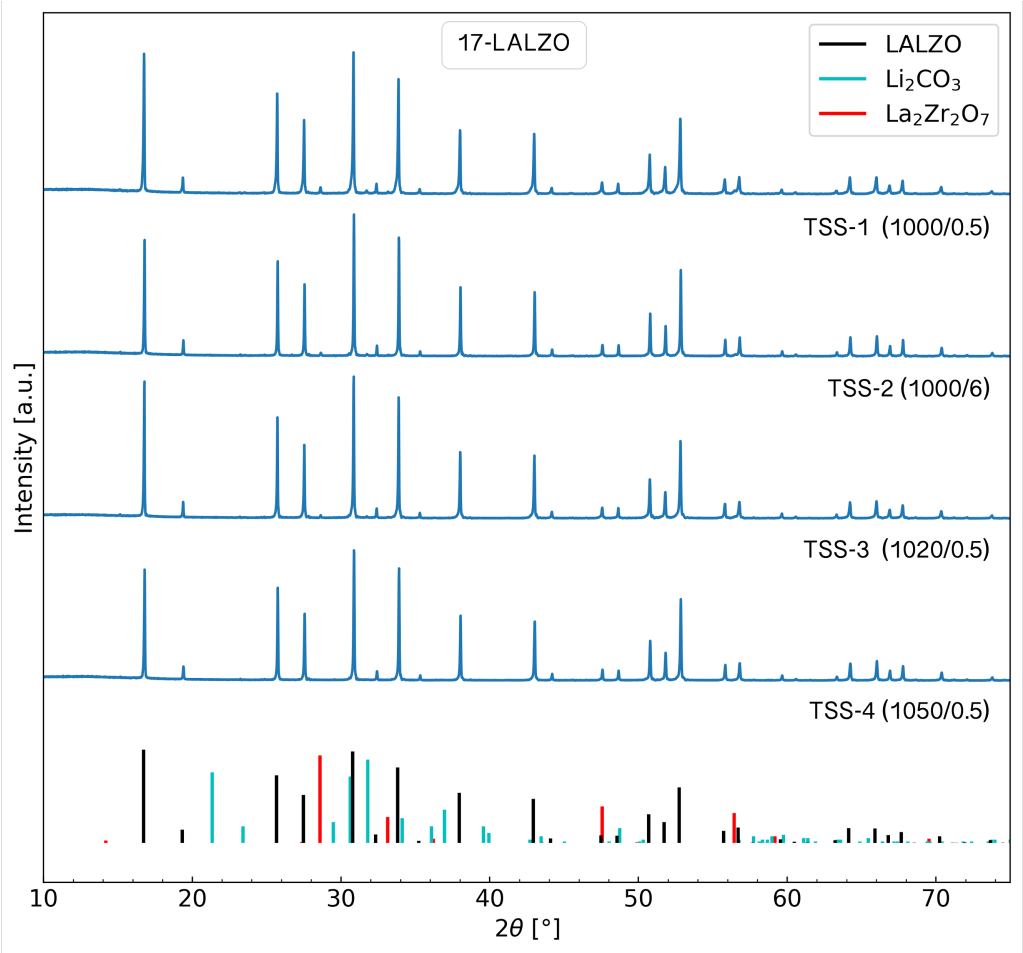

Figure 4.12: Diffraction patterns of two-step sintered pellets of composition 17-LALZO. All samples are indexed to c-LALZO. TSS-1 (1000/0.5), TSS-2 (1000/6) and TSS-3 (1020/0.5) contain traces of $La_2Zr_2O_7$ and Li_2CO_3.

4.3.3 Microstructure

Microstructures of the fracture surfaces for two-step sintered pellets of composition 24,2-LALZO are displayed in Figures 4.13 and 4.14. Coarsening and abnormal grain growth with a wide grain size distribution were observed for all temperature programs used. Grains with diameters of 100 µm are especially prominent in Figures 4.13b, d, f and h, while tiny grains of size 1 µm implying low degree of grain growth during the heat treatment are visible in Figure 4.14a of TSS-1 (1000/0.5). The micrograph is representative for all two-step sintered pellets of composition 24,2-LALZO. Small grains are especially concentrated along the edges of the pellets as illustrated in Appendix G.1 of temperature program TSS-2 (1000/6), while larger grains are observed at the center of the pellets as shown in Figures 4.13a, c, e and g.

Transgranular fractures are observed for large grains, while intergranular fractures are observed for small grains. Internal pores are evidenced in the large grains, as shown in Figure 4.14b of TSS-1 (1000/0.5) sintered pellet.

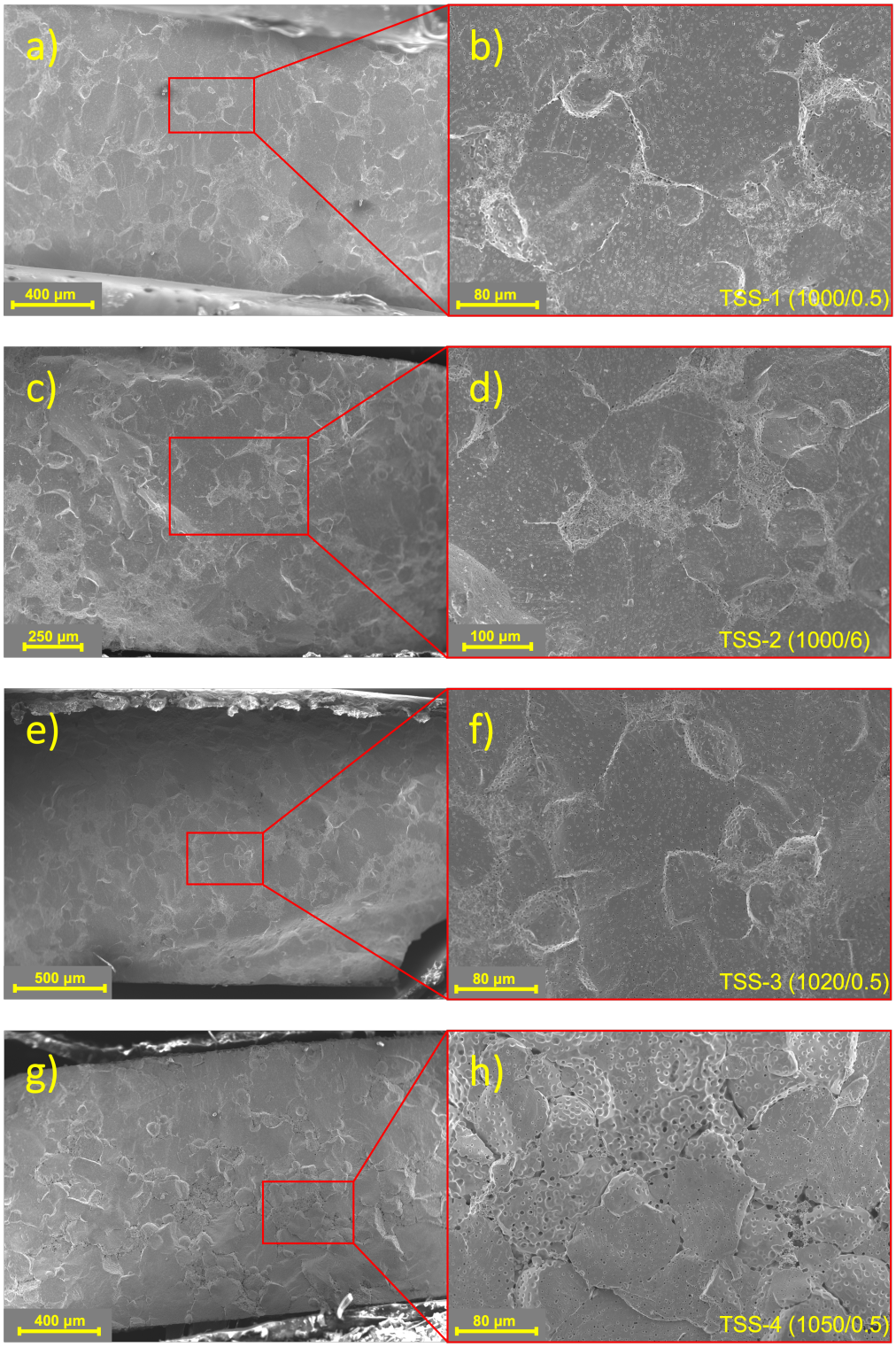

Figure 4.13: SEM of two-step sintered pellets of composition 24,2-LALZO. Temperature program TSS-1 (1000/0.5) displayed in a) and b), TSS-2 (1000/6) in c) and d), TSS-3 (1020/0.5) in e) and f), and TSS-4 (1050/0.5) in e) and f). Areas in red frames in a), c), e) and g) are magnified in b), d), f) and h).

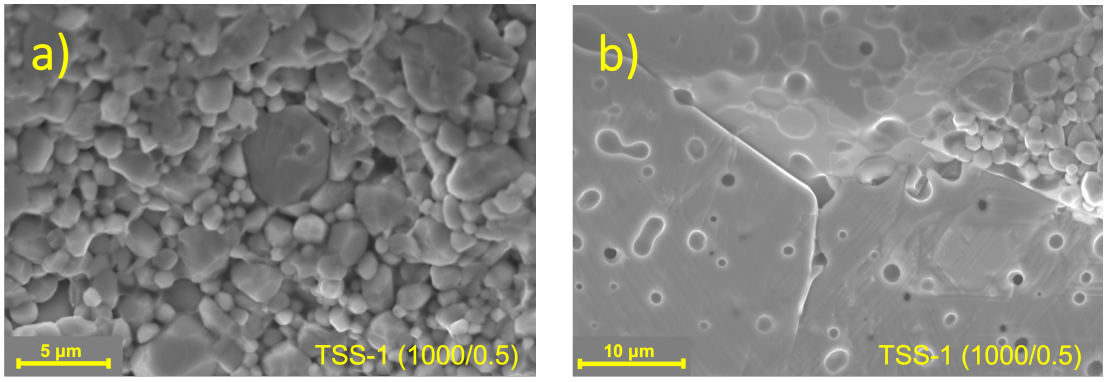

Figure 4.14: SEM of 24,2-LALZO pellet fracture surface after TSS-1 (1000/0.5). Small grains in bulk displayed in a), abnormal grain growth shown in b).

Figure 4.15 presents fracture surfaces of two-step sintered pellets of composition 17-LALZO. Normal grain growth is observed for all temperature programs in Figures 4.15b, c and d, with a grain size distribution between 2 and 10 µm. Most prominent densification behavior is observed for TSS-2 (1000/6), shown in Figure 4.15d, with the longest holding time of 6 h at 1000 °C for the secondary sintering. TSS-3 (1020/0.5) and TSS-4 (1050/0.5), with the highest temperatures during the final sintering at respectively 1020 and 1050 °C for 0.5 h, show least effect with larger concentrations of very small grains, displayed in Figure 4.15f and h.

The polished surfaces of TSS-1 (1000/0.5) 24,2-LALZO and 17-LALZO are compared in Figure 4.16 using back-scattered electrons (BSE) for imaging. The micrographs clearly display the difference in density of the pellets, which corresponds with the density measurements in Figure 4.10. The higher degree of porosity shown in sintered pellet of 17-LALZO resulted in lower density, and is mainly due to intergranular pores. 24,2-LALZO obtained the highest density with high degree of grain growth, revealing large grains with captured pores causing irretrievable porosity within the grains.

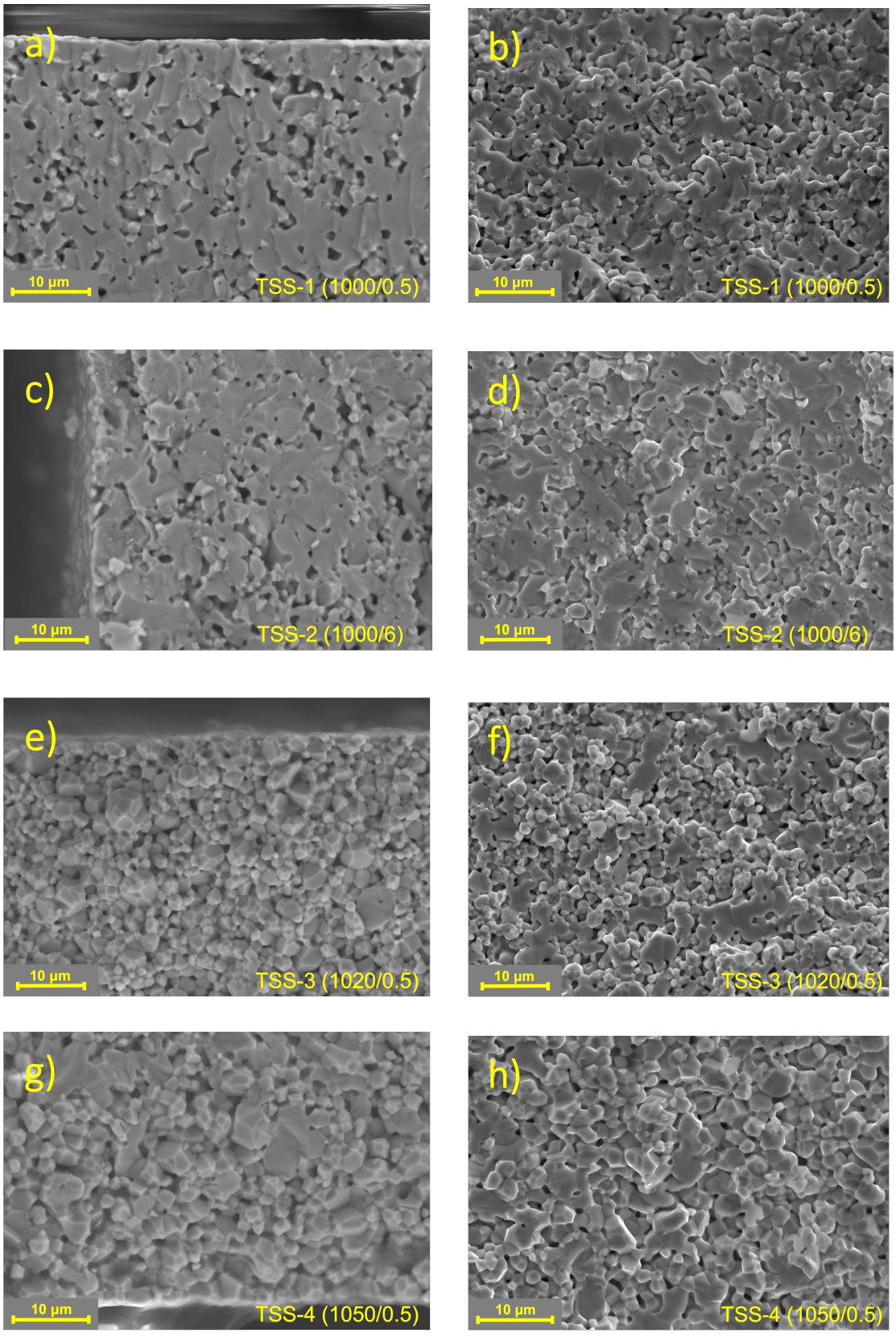

Figure 4.15: SEM of two-step sintered pellets of composition 17-LALZO. Temperature program TSS-1 (1000/0.5) displayed in a) and b), TSS-2 (1000/6) in c) and d), TSS-3 (1020/0.5) in e) and f), and TSS-4 (1050/0.5) in g) and h) displaying edge and bulk, respectively.

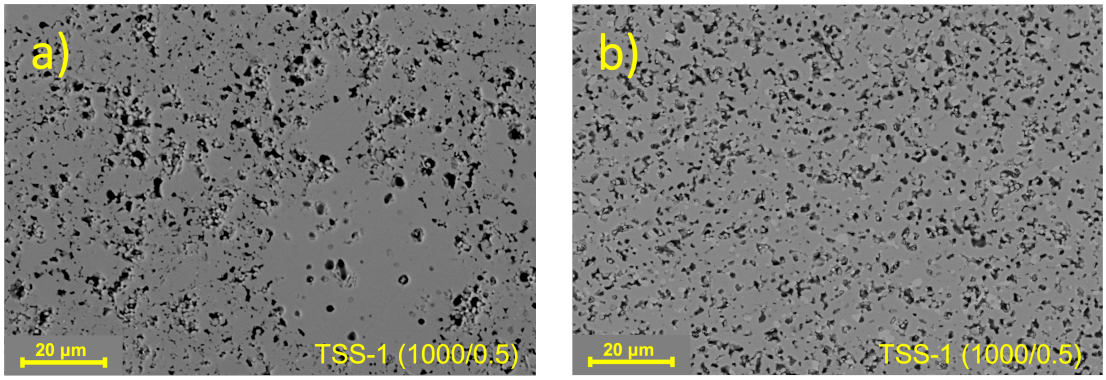

Figure 4.16: Back scattered electron micrographs of TSS-1 (1000/0.5) sintered pellets. 24,2-LALZO is displayed in a) and 17-LALZO is displayed in b).

4.3.4 Elemental analysis

EDS elemental analyses were conducted on polished fracture surfaces of TSS-1 (1000/0.5) sintered pellets utilizing point scan detection. Li is not detected due to the low atomic number. Carbon sputtering was utilized prior to imaging for providing conductivity, and carbon is therefore excluded from the scan results as the measurements of the carbon concentration would be incorrect.

The results obtained from the point scan analysis of composition 24,2-LALZO are presented in Table 4.1, and the corresponding micrograph can be found in Figure 4.17. The analysis focused on three distinct areas: edge of pores (spectrum 1 and 2) and the bulk (spectrum 3) of the pellet. Observations at the grain boundaries in spectrum 1 and 2 revealed higher concentrations of Al and O when compared to the bulk. No Al was found in spectrum 3, but there was a significant amount of La and Zr in this area.

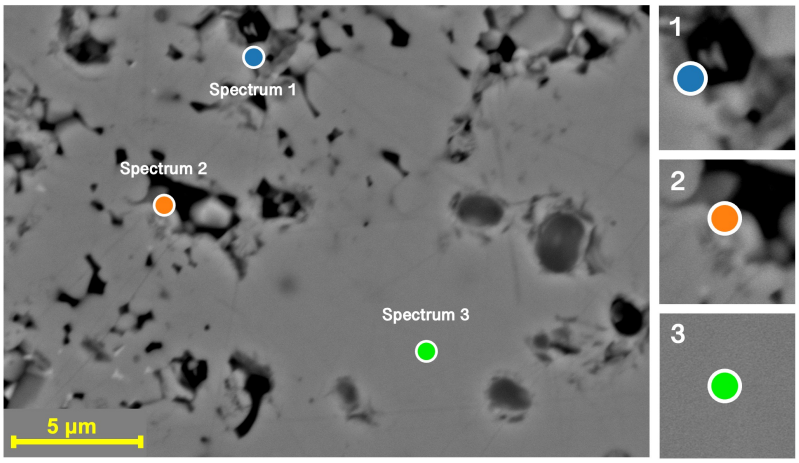

Figure 4.17: EDS analysis of two-step sintered 24,2-LALZO (TSS-1 (1000/0.5)). Imaging using back scattered electrons (BSE).

Table 4.1: EDS point scan detection results from composition 24,2-LALZO using EDS.

	24,2-LALZO		
Element	Spectrum 1	Spectrum 2	Spectrum 3
	[at%]	[at%]	[at%]
O	69.7	72.5	67.4
Al	1.3	0.7	
Zr	11.3	10.8	12.6
La	17.7	16	20
Position	Edge of pore	Edge of pore	Bulk

EDS elemental distribution analysis for 17-LALZO is presented in Table 4.2, and the corresponding SEM micrograph can be found in Figure 4.18. Three specific areas were selected for point scans, each representing different properties. Spectrum 1 was chosen from one of the light areas visible on the fracture surface of the polished pellet. In this spectrum, a high concentration of La was detected, while the concentrations of Al and Zr were lower compared to the other areas polished. Si was detected due to contamination from equipment utilized. Spectrum 2 represents the element distribution at the edge of pores. In this spectrum, higher concentrations of Al were observed. The elemental content in bulk sections is represented by spectrum 3.

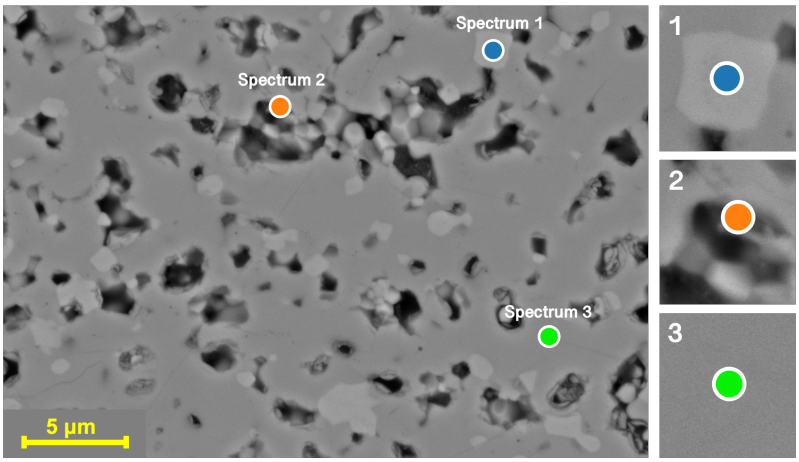

Figure 4.18: EDS analysis of two-step sintered 17-LALZO (TSS-1 (1000/0.5)). Imaging using back scattered electrons (BSE).

Table 4.2: EDS point scan detection results from composition 17-LALZO using EDS.

	17-LALZO		
Element	Spectrum 1	Spectrum 2	Spectrum 3
	[at%]	[at%]	[at%]
O	62.5	62.6	66.6
Al	1.7	2.4	2.1
Zr	7.2	13.1	12.4
La	27.5	21.9	18.9
Si	1.1		
Position	Bulk	Edge of pore	Bulk

4.4 Spark plasma sintering

4.4.1 Phase composition

In Figure 4.19, the phase identifications of spark plasma sintered pellets and two-step sintered pellets are compared. SPS-3 (0.7) and TSS-1 (1000/0.5) for composition 17-LALZO are displayed. The sintered pellet of SPS-3 (0.7) contains secondary phases, with numerous diffraction lines deviating from the diffraction pattern of c-LALZO. Li_2CO_3 is observed at 2θ-values 23.41°, 29.47°, 31.80° and 48.02°. Diffraction lines of high intensity indicating $La_2Zr_2O_7$ to be present, corresponding with all 2θ-values characterizing the secondary phase due to high Li loss during the spark plasma sintering process. Graphite is identified at 2θ-value 26.54° caused by contamination from the graphite pistons and foil. Residual diffraction lines are indexed to carbon-containing materials. Broad diffraction lines for all observed reflections are detected, indicating small crystallites.

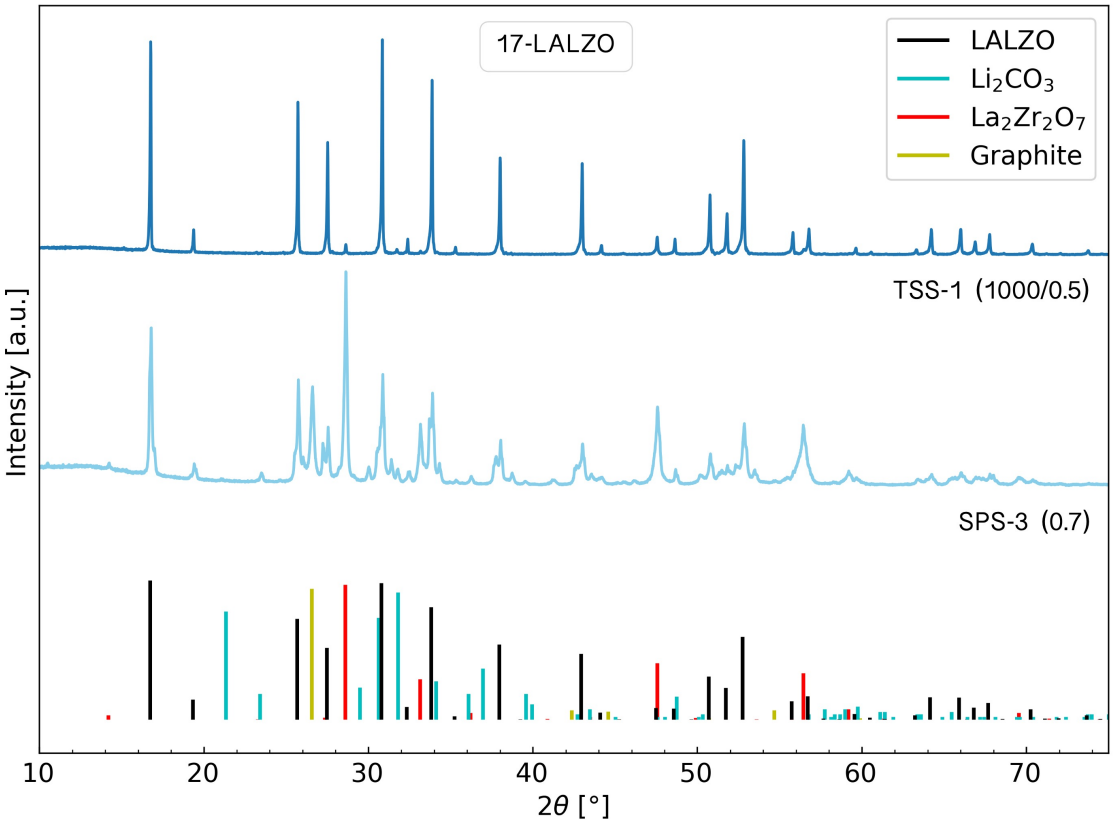

Figure 4.19: Comparison of two-step sintered and spark plasma sintered pellets of composition 17-LALZO. Diffraction diffraction lines for LALZO, Li_2CO_3, $La_2Zr_2O_7$ and graphite are included.

4.4.2 Microstructure

Photos captured after spark plasma sintering of 17-LALZO are displayed in Appendix H.1 of SPS-1 (0.35) and SPS-3 (0.7) and in Appendix H.2 of SPS-2 (0.4). A metallic color was observed after the sintering process at the pistons, as shown in Appendix H.1, which could indicate reactions with carbon (graphite paper and graphite die). Only pellets of sintering programs SPS-2 (0.4) and SPS-3 (0.7) could be removed from the piston, as the mass loss during the heat treatment were too excessive for the SPS-1 (0.35) sintered pellet, shown in H.1a. The thicknesses of the pellets were measured to $\sim$ 0.6 and 1 mm for SPS-2 (0.4) and SPS-3 (0.7), with some deviation due to deformation during removal. The pellets were not coherent after the sintering process, and were falling apart while trying to remove the graphite paper on the surfaces for sintered pellets of SPS-2 (0.4) and SPS-3 (0.7). Phase characterization and imaging of microstructure were hence executed with the graphite paper present.

The microstructures of spark plasma sintered pellets of composition 17-LALZO and sintering programs SPS-2 (0.4) and SPS-3 (0.7) are displayed in Figure 4.20. The pellets are heterogeneously sintered as shown in Figure 4.20b, displaying the edge of the SPS-2 (0.4) sintered pellet, with variation in densification degree. Small grains are observed in 4.20c, while neck formation between grains is observed in Figure 4.20d. These two areas are 20 µm apart from each other, illustrating the sudden difference in densification during spark plasma sintering.

The difference within the bulk is displayed in Figures 4.20e and f of SPS-3 (0.7). Some areas contain very small grains ($\sim$ 1 µm) with no densification observed, while others are dense. Major cracks of up to 150 µm are observed in the sintered pellets, as shown in 4.20a of SPS-2 (0.4), indicating low mechanical strength.

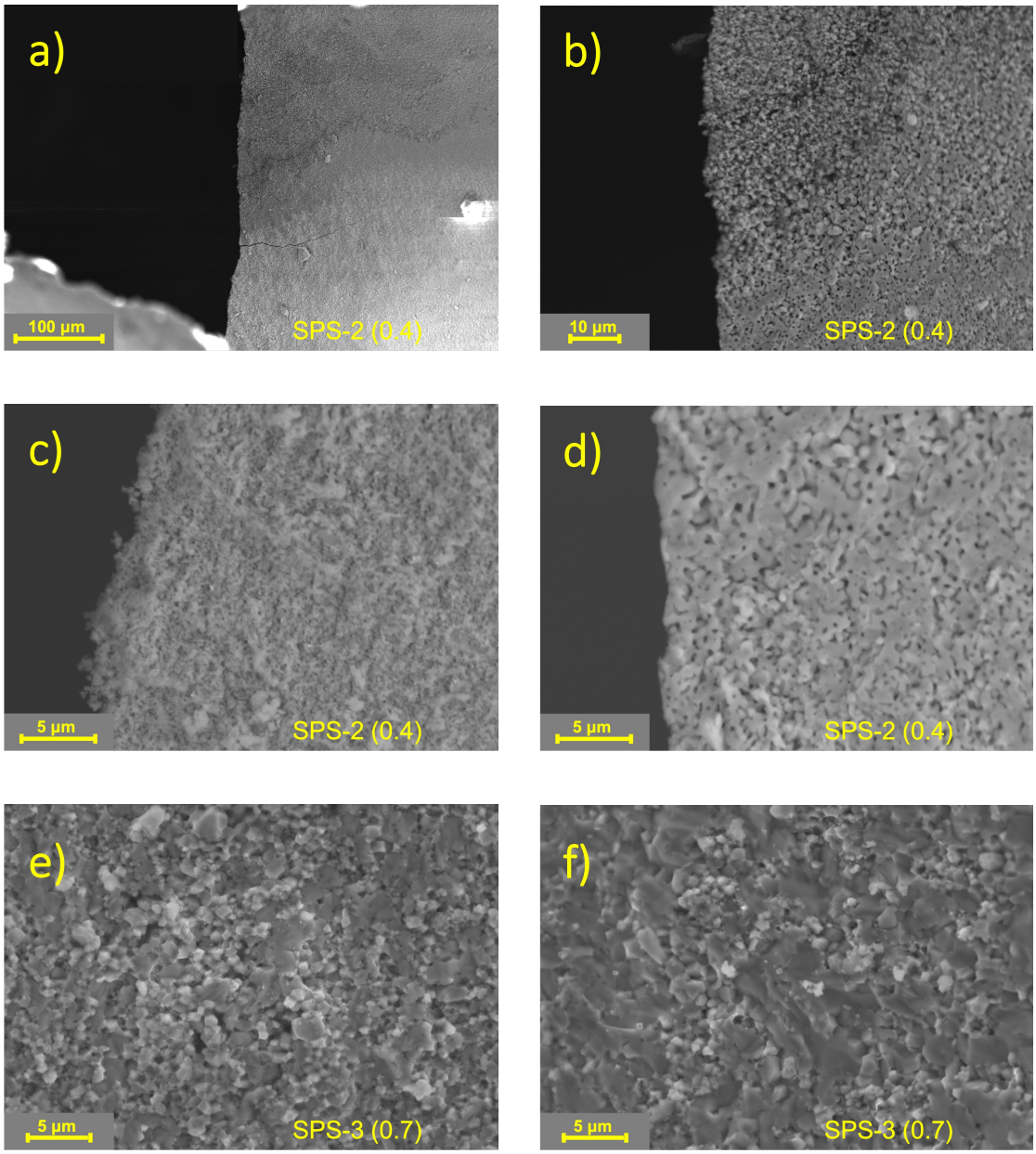

Figure 4.20: SEM micrographs of spark plasma sintered pellets of composition 17-LALZO. SPS-2 (0.4) is displayed in a), b), c) and d), SPS-3 (0.7) is displayed in e) and f).

4.4.3 Gas evolution

Figure 4.21 displays the gas pressure during SPS-3 (0.7) of 17-LALZO and temperature development as a function of time. Three notable and sharp features are observed. Conditions and measurements during the increase in gas pressure are shown in Table 4.3 with corresponding time intervals highlighted in the grey frames in Figure 4.21. Temperatures for the first increase in gas pressure are not included, as the temperature measurements started at 400 °C. The second peak shows the greatest pressure increase with 10.6 Pa. The third peak was observed with an increase of 5 Pa, which occurred when the applied uniaxial pressure was increased from 25 to 50 MPa.

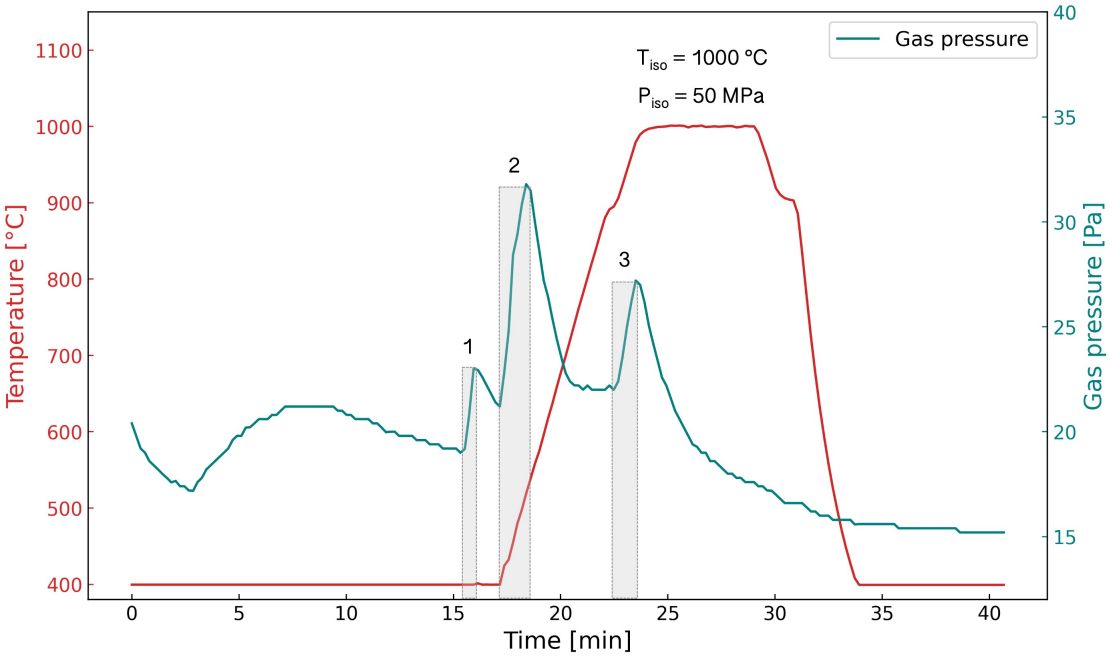

Figure 4.21: Gas evolution during spark plasma sintering of pellets. Measured temperature and vacuum are displayed as functions of time. Notable gas evolution highlighted in the grey frames.

Table 4.3: Conditions and measurements during gas evolution for spark plasma sintering. ΔGas pressure and ΔP denotes the change in respectively vacuum and temperature for the gas evolution. The starting temperature of the first peak was below measurable temperature.

Interval	ΔP [MPa]	T_{start} [°C]	T_{end} [°C]	ΔGas pressure [Pa]
1	0	-	-	4
2	0	400	530	10.6
3	25	900	960	5

4.5 Electrochemical impedance assessment of sintered pellets

Nyquist plots obtained from the measurements conducted at RT are presented in Figure 4.22. The dimensions of the pellets were taken into account to ensure comparability. The resistance values in the samples were calculated based on the widths of the semicircles observed in the Nyquist plots.

For 24,2-LALZO, a single semicircle is observed in Figure 4.22a, which arises mainly due to contributions from the bulk. The grain boundary density is low for materials with larger grains, causing the resistivity contributions to be negligible. In the case of 17-LALZO, two semicircles are observed, as shown in Figure 4.22b. The high-frequency semicircle is attributed to resistance contributions from the bulk, while the second semicircle at lower frequencies is caused by resistance contributions at the grain boundaries. Additionally, the diffusion tails observed in both samples correspond to the resistance from the blocking electrode. The total ionic conductivities for the samples are listed in Table 4.4, and was determined using the equivalent circuits depicted in Figure 3.7 to 5.6×10^{-6} S/cm for 24,2-LALZO and 4.3×10^{-4} S/cm for 17-LALZO.

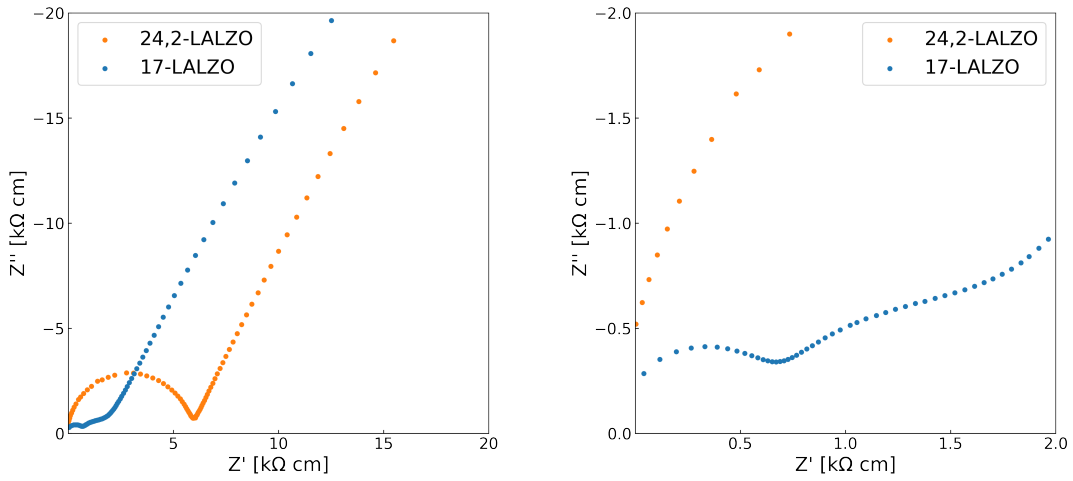

(a) (b)

Figure 4.22: Electrochemical impedance measurements for TSS-1 (1000/0.5) 24,2-LALZO and 17-LALZO, conducted at RT.

The EIS measurements for temperatures ranging from 30 to 200 °C are plotted in Arrhenius diagrams, depicted in Figures 4.23 and 4.24 for 24,2-LALZO and 17-LALZO, respectively. The plots include interpolated lines to facilitate the assessment of activation energy. In Figure 4.24, two lines represent the sintered pellet of composition 17-LALZO, corresponding to temperature intervals of 30 to 70 °C and 80 to 200 °C. One interpolated line is displayed in Figure 4.23 of 24,2-LALZO corresponding to the whole temperature range.

The measurements reveal a distinct change in behavior above 80 °C for the 17-LALZO composition. At this point, the absolute value of the slope noticeably increases, indicating a change in Li-ion conductivity mechanism. The experimental data for 24,2-LALZO, as shown in Figure 4.23, align closely to a single line.

From the Arrhenius plots and interpolated lines, the activation energies and pre-exponential factors were determined and are listed in Table 4.4. 24,2-LALZO obtains an activation energy of 0.35 eV and a pre-exponential factor of 51 S/mol. For measurements below 80 °C, the activation energy of 17-LALZO is determined to 0.22 eV and the pre-exponential factor to 0.34 S/mol. A shift occurs at 80 °C, where the activation energy is increased to 0.47 eV and the pre-exponential factor to 1070 S/mol.

Table 4.4: Data obtained from Nyquist plots and Arrhenius plots. T = temperature, E_a = activation energy for lithium diffusion, A = pre-exponential factor, σ_{RT} = total ionic conductivity.

Composition	T [°C]	E_a [eV]	E_a [kJ/mol]	A [S/mol]	σ_{RT} [S/cm]
24,2-LALZO	RT				5.6×10^{-6}
17-LALZO	RT				4.3×10^{-4}
24,2-LALZO	30-200	0.35	34	51	
17-LALZO	30-70	0.22	21	0.34	
17-LALZO	80-200	0.47	45	1070	

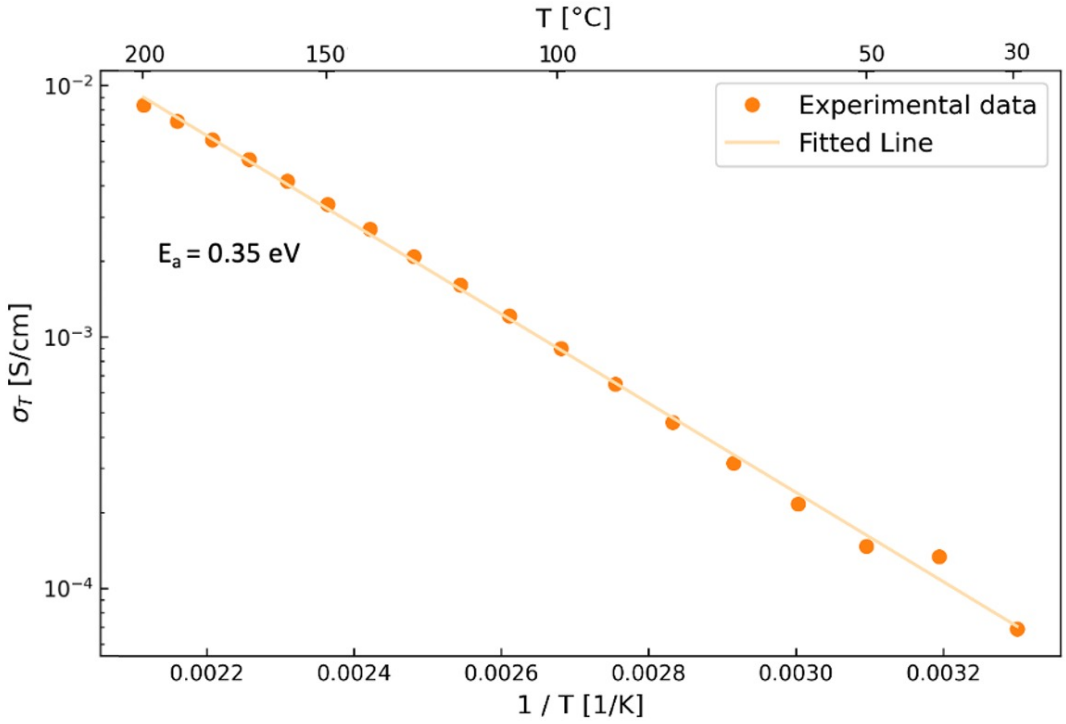

Figure 4.23: Arrhenius plot of TSS-1 (1000/0.5) 24,2-LALZO. Temperature range measured was 30 to 200 °C. The line displayed is interpolated using the total temperature range.

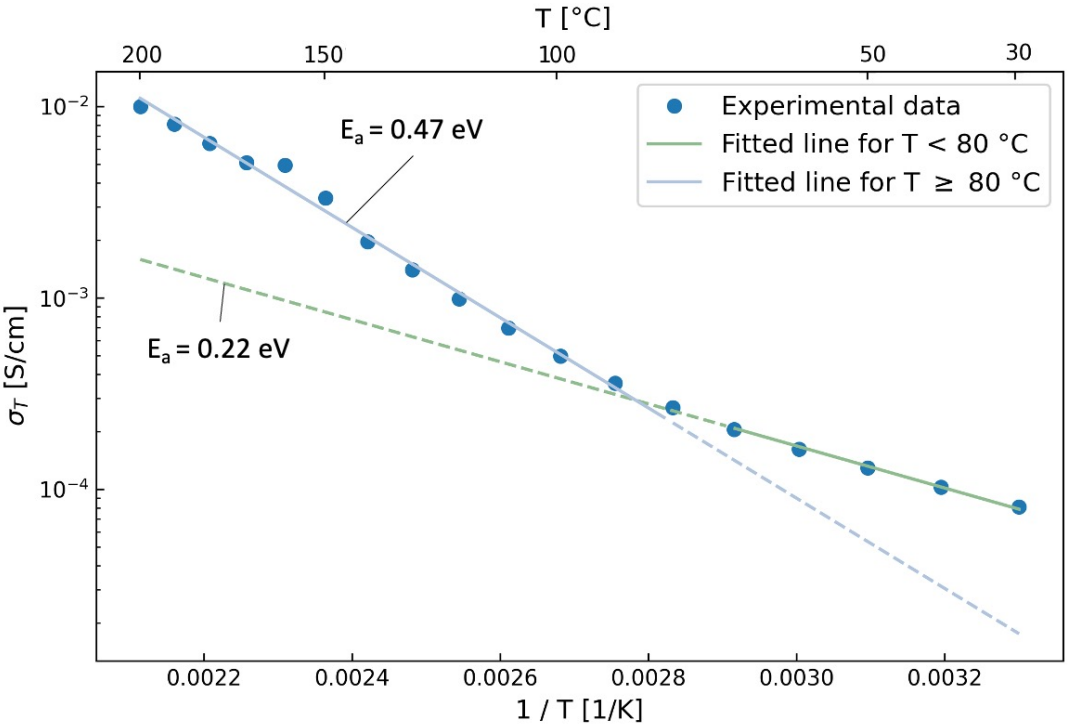

Figure 4.24: Arrhenius plot of TSS-1 (1000/0.5) 17-LALZO. Temperature range measured was 30 to 200 °C. Two lines are interpolated using the experimental for data temperature ranges 30-70 °C and 80-200 °C, indicating a break point at 80 °C.

5 | Discussion

5.1 Precursor powders

5.1.1 Phase composition

The nitrates undergo incomplete decomposition during the spray pyrolysis process, as shown in the diffractograms of precursor powders 24,2-LALZO and 17-LALZO in Figure 4.1. Despite having decomposition temperatures below measured temperature in the tube furnace during spray pyrolysis, the XRD of the precursor powders indicate insufficient exposure time for achieving single phase c-LALZO (Appendix A). As a result of residual $LiNO_3$ in the precursor powders, available Li used during formation of LALZO is limited, and the secondary phase $La_2Zr_2O_7$ is formed.

Traces of Li_2CO_3 was also observed due to exposure to an atmosphere containing CO_2 during synthesis of precursor solution and spray pyrolysis, and could be removed by adequate exposure to elevated temperatures. Li_2CO_3 decomposes according to Equation 2.4, and at elevated temperatures the transport of CO_2 will be facilitated due to enhanced partial pressure of CO_2 (Appendix B).

5.1.2 Phase development during heat treatment

The appearance of $LiNO_3$ and $La_2Zr_2O_7$ in the precursor powders induces formation of $LaAlO_3$ and $Li_{0.5}Al_{0.5}La_2O_4$ at temperatures between 400 and 500 °C, as observed in the 2D representation of the HT XRD in Figure 4.5 and the DSC in Figure 4.3. Formation of the secondary phases is attributed to a deficiency of Li and an excessive amount of Al within the crystal structure during the formation of LALZO. Different decomposition rates and temperatures for the respective nitrates cause a concentration of Al above the solubility limit in the LLZO-structure, leading to formation of the Al-rich secondary phases $LaAlO_3$, shown in Equation 2.6, and $Li_{0.5}Al_{0.5}La_2O_4$, shown in Equation 5.1 [21].

$$0.25Li_2O(s) + 0.25Al_2O_3(s) + La_2Zr_2O_7(s) \longrightarrow Li_{0.5}Al_{0.5}La_2O_4(s) + 2ZrO_2(s) \tag{5.1}$$

Also high concentration of $La_2Zr_2O_7$ plays a role in the formation of $Li_{0.5}Al_{0.5}La_2O_4$, in accordance with Le Chatelier's principle applied to the reaction described in Equation 5.1. Upon further heating of the precursor powder, decomposition of $LiNO_3$ occurs, evidenced in the TGA in Figure 4.2 and DSC in Figure 4.3, leading to an increase of available Li in the system. The significant mass losses observed from TGA for both 24,2-LALZO and 17-LALZO around the decomposition temperature of $LiNO_3$ indicate high concentrations of the nitrate in the precursor powders, and hence a notable increase in Li content after decomposition. The increase in Li content causes reactions with $Li_{0.5}Al_{0.5}La_2O_4$ and $LaAlO_3$, resulting in formation of LALZO, as evidenced in the diffractogram at 700 °C in Figure 4.5.

The difference in mass loss between 24,2-LALZO and 17-LALZO of 15 wt% measured during TGA is higher than anticipated comparing to the calculated expected mass losses of 0.1 wt% (Appendix E). This is most likely a consequence of the spray pyrolysis process together with formation of VLCs. As different amounts of deionized water were utilized during the initial synthesis of precursor solutions, this will affect the results from the TGA. Varying evaporation and heating conditions during spraying for the two precursor powders could be a source of uncertainty, which is expected for the applicable manufacturing method. In addition, 24,2-LALZO shows higher mass loss at the decomposition temperature of Li_2CO_3, implying different exposure to ambient air and therefore CO_2 during synthesis of precursor powders 24,2-LALZO and 17-LALZO.

5.1.3 Microstructure

Since the phase compositions of the precursor powders 24,2-LALZO and 17-LALZO are primarily dominated by nitrates, obtaining a similar agglomerate size distribution and microstructure is expected. The spherical shape of the agglomerates, shown in the micrographs in Figures 4.6b and d, indicates simultaneous agglomeration through the spraying procedure. The maximum agglomerate size formed during spray pyrolysis is approximately 10 µm and aligns well with the results shown in Figures 4.6b and d.

5.2 Calcined powders

5.2.1 Phase composition

The calcined 24,2-LALZO powder exhibits a single phase tetragonal crystal structure, as illustrated in Figure 4.8, which arises from an excess of Li within the system after complete decomposition of $LiNO_3$. This excess of Li causes occupation of the tetragonal Li sites in the cubic crystal structure, which are originally vacant as depicted in Figure 2.1 due to the introduction of Al to the material. The formation of t-LALZO suggests that the amount of additional Li incorporated in the precursor solution of 24,2-LALZO was too high for achieving c-LALZO through calcination. The absence of diffraction lines of $La_2Zr_2O_7$ in the diffractogram confirms the complete removal of the secondary phase, contributing to the formation of LALZO through reaction with Li_2O(s) as shown in Equation 2.5.

In 17-LALZO, c-LALZO and small amounts of $La_2Zr_2O_7$ are formed, observed in the diffractogram in Figure 4.7, due to a deficiency of Li in the calcined powder. In an attempt to counteract this issue, an excess of 17 mol% Li was included in the precursor solution, which shows to be insufficient for achieving a single phase material from calcination.

Low intensity diffraction lines of Li_2CO_3 are observed for both compositions, indicating insufficient decomposition during calcination. It is therefore apparent that the concentration of Li_2CO_3 in the precursor powders requires higher temperatures or longer exposure time for decomposition and sufficient transport of CO_2 out of the material.

5.2.2 Microstructure

The range of agglomerate sizes for calcined 24,2-LALZO and 17-LALZO, shown in Figure 4.9, has decreased with $\sim$ 5 µm compared to the precursor powders of equal composition. Volatile compounds, moisture and residual nitrates are removed from the agglomerates during the heat treatment, causing shrinkage of the agglomerates. The phase transformation from c-LALZO to t-LALZO in the calcined powder of 24,2-LALZO may have altered some of the agglomerates to break, as shown in Figure 4.9b. The crystal structure distortion and change in lattice parameters are suspected to have affected the stability and cohesion of the agglomerates. In 17-LALZO, agglomerates retained spherical shapes due to the preserved cubic crystal structure.

5.3 Two-step sintered pellets

5.3.1 Phase composition

Single phase c-LALZO was successfully achieved for TSS-4 (1050/0.5) of 17-LALZO, which implies a sufficient Li supply from the powder bed, causing formation of c-LALZO from $La_2Zr_2O_7$ and the available Li^+ in the structure. Also, the decomposition of Li_2CO_3 implies that the duration and temperature were adequate for transportation of CO_2 out of the pellet. As TSS-1 (1000/0.5), TSS-2 (1000/6) and TSS-3 (1020/0.5) are observed with small concentrations of the secondary phases $La_2Zr_2O_7$ and Li_2CO_3, there seem to be minor differences in concentrations within the utilized calcined powder, leading to slightly different phase compositions for the pellets.

What differentiates TSS-4 (1050/0.5) from the other temperature programs of 17-LALZO is the higher temperature at the secondary sintering. This could have caused an increase in transportation rate of CO_2 out of the crystal structure, but as the temperature difference is quite small, between 30 and 50 °C, it should not have a significant impact on the decomposition of Li_2CO_3. Also, due to the higher sintering temperature during operation, the pellet is more likely to form VLCs and subsequently decreasing the Li content rather than increasing the amount of Li causing removal of $La_2Zr_2O_7$ from the structure. Since the precursor powders were calcined in multiple batches, observations from XRD analysis of the sintered pellets give reason to believe that there may have been some variation in the phase composition of the different batches. Additionally, the entire batch was most likely not properly mixed, causing differences in the final products.

Two-step sintering of 24,2-LALZO resulted in single phase t-LALZO for all temperature programs, proving no significant change in Li content in the samples during sintering. The pellets have been subjected to high temperatures, where formation of VLCs is expected, but due to the use of powder bed of high Li content, the composition has not changed significantly. The broadening observed for the diffraction lines corresponding to t-LALZO is caused by a small grain size in the pellet. Although the sintered pellets are observed with enormous grains, as shown in the micrograph in Figure 4.13, several minor grains are also present, shown in Figure 4.14a and Appendix G.1, causing the wide diffraction lines in Figure 4.11. The smaller crystalline domains obtain a distribution of crystallographic orientations, resulting in a spread of diffraction angles [74]. Furthermore, Li_2CO_3 is no longer evident in the sintered pellets of 24,2-LALZO, proving sufficient exposure to elevated temperatures for decomposition.

5.3.2 Densification behavior

Pellets of high density, uniform microstructure, normal grain growth and single phase composition were achieved from two-step sintering of calcined powder of 17-LALZO. Ball milling prior to sintering was employed for breaking the agglomerates in the calcined powders, yielding a homogeneous agglomerate size distribution and facilitating optimal grain growth during the heat treatment.

Temperatures and duration of the second step of the two-step sintering were adjusted for achieving high densities and optimal microstructure of the pellets. The selection of temperatures was based on observations from previous studies, where elevated temperatures led to the formation of a liquid Li-Al-O phase and consequently AGG and a bimodal grain size distribution after sintering of Al-doped LLZO [7, 25]. To prevent the formation of this phase, all secondary sintering temperatures were kept below the eutectic temperature 1064 °C in the Li_2O-Al_2O_3 system, shown in the phase diagram in Figure 2.5. At this temperature, the coexistence of Li_5AlO_4, $LiAlO_2$, and a liquid phase may occur, which could lead to high diffusion rates and coarsening. Although lowering the temperatures could inhibit an unfavorable microstructure, a significant decrease would restrain the densification of the material. Hence, the secondary temperatures were determined to 1000, 1020, and 1050 °C. The primary sintering temperature was kept constant at 1150 °C for all temperature programs to initiate neck formation between particles and increase the density of the final product. Although this temperature is above the eutectic temperature in the Li-Al-O system, the short exposure time of 10 min is considered insufficient for the liquid Li-Al-O phase to significantly impact the microstructures of the pellets and cause AGG.

The relative densities for two-step sintered pellets of 24,2-LALZO and 17-LALZO deviated from each other with between 2.4 and 4.9% for each temperature program (presented in Figure 4.10), suggesting a potential correlation between the Li content in the compositions and the densification behavior during sintering. As the pellets of highest Li excess resulted in highest relative density, this could indicate enhanced diffusion rates with increased Li concentration and subsequently rapid removal of porosity in the microstructure.

Observations of AGG in Figure 4.13 of two-step sintered 24,2-LALZO support the assumptions of higher diffusion rates, causing excessive grain growth and a bimodal grain size distribution. The large growth of the grains could remove porosity between the grains, but trapped pores within the grains is likely to occur, resulting in irretrievable porosity. Porosity is removed by grain boundary movement. However, as the grains grow, if the grain boundary movement is too rapid, the pores will be trapped within the grains. As seen in the micrograph in Figure 4.14b, isolated pores are observed within some of the grains. Dark areas are observed in the fracture surface in the micrograph in Figure 4.16a, which could be trapped pores within the grains due to the rapid grain growth, but it could also be porosity between the grains.

By assessing the density measurements of the pellets, presented in Figure 4.10, there is a slight difference between the pellets. TSS-4 (1050/0.5), with the highest temperature during the secondary sintering of 1050 °C, shows the lowest relative density of the 24,2-LALZO sintered pellets, which could indicate a higher concentration of trapped pores within the grains as a result of rapid grain growth. The duration at the secondary sintering does not seem to have significant impact on the density or the microstructure of the pellets, as the difference between TSS-1 (1000/0.5) and TSS-2 (1000/6) with 0.5 h and 6 h, respectively, is negligible.

The rapid grain growth could be induced by the formation of liquid Li-Al-O phases. Table 5.1 displays the relation between cations and oxygen, based on the selected areas and corresponding values from the EDS point scan analysis of 24,2-LALZO sintered pellet of temperature program TSS-1 (1000/0.5), presented in Figure 4.17 and Table 4.1. Nominal stochiometry of LALZO is included for comparison. No Al was found in the bulk sections, showing an accumulation of the element towards the edge of the pores. The increased concentration of Al in these areas could contribute to the formation of Li-Al-O phases, and together with the primary sintering above the eutectic temperature, this could promote excessive grain growth. Values representing the bulk areas correlate with LALZO for the ratios including La, Zr and O, which matches with the identification of t-LALZO from XRD of the pellet. Low Al content distorts the crystal structure from cubic to tetragonal, as the Al ions stabilizes the c-LALZO by occupying Li sites and forming Li vacancies.

Table 5.1: Ratios between cations and oxygen, based on the EDS point scan analysis of 24,2-LALZO.

	24,2-LALZO			
Relation	Spectrum 1	Spectrum 2	Spectrum 3	LALZO
La/Zr	1.6	1.5	1.6	1
La/Al	13.7	22.5	-	12
Zr/Al	8.7	15.2	-	8
O/La	3.9	4.5	3.4	4
O/Zr	6.2	6.7	3.5	6
O/Al	53.6	102.1	-	48
Position	Edge of pore	Edge of pore	Bulk	

17-LALZO, on the other hand, is observed with normal grain growth and narrow grain size distribution, as shown in the micrographs in Figure 4.15, due to slow grain growth during sintering. AGG primarily occurs at relative densities above 92 %, and as density measurements of 17-LALZO was between 88.2 and 90.4 %, it is uncertain whether the samples are susceptible to AGG. The narrow grain size distribution increases the connectivity between grains in the sample, contributing to efficient transport of Li^+ across the grains in the material.

Table 5.2 displays the ratios between cations and oxygen in TSS-1 (1000/0.5) of 17-LALZO, where nominal compositions of $La_2Zr_2O_7$ and LALZO are included as the phases were observed in the XRD. Due to the lower content of Al in spectrum 1 compared to the two other areas measured, the secondary phase $La_2Zr_2O_7$ is suspected. $La_2Zr_2O_7$ consists of heavy elements, which explains the brighter appearance in the backscatter SEM micrographs compared to the other areas. The presence of light areas due to $La_2Zr_2O_7$ on polished surface of LLZO systems was also observed in the work by Nybrodahl, due to Li loss during sintering [26]. Spectrum 2 and 3 obtain similar elemental distributions. The deviation between the measurements and the literature values of LALZO is expected due to uncertainty of EDS, but is quite small, indicating formation of c-LALZO in these areas.

Table 5.2: Ratios between cations and oxygen, based on the EDS point scan analysis of 17-LALZO.

	17-LALZO				
Relation	Spectrum 1	Spectrum 2	Spectrum 3	$La_2Zr_2O_7$	LALZO
La/Zr	3.8	1.7	1.5	1	1
La/Al	10.6	9	8.9	-	12
Zr/Al	4.4	5.4	5.8	-	8
O/La	2.3	2.9	3.5	3.5	4
O/Zr	8.7	4.8	5.4	5.4	6
O/Al	37.88	25.9	31.4	-	48
Position	Bulk	Edge of pore	Bulk		

Most notable densification behavior for 17-LALZO is observed for TSS-2 (1000/6), shown in Figures 4.15c and d, which obtained the longest exposure time at elevated temperatures. Also, TSS-1 (1000/0.5) presented in the micrographs in Figures 4.15a and b show prominent necking between the grains. Although TSS-1 (1000/0.5) and TSS-2 (1000/6) show similar microstructure, the two samples differ from each other with respect to density with 2.1 %. The sample of shortest holding time, TSS-1 (1000/0.5), obtained the highest relative density, which is unexpected as a longer duration should increase the reduction of porosity. The difference could be explained by microstructural defects like voids decreasing the density of TSS-2 (1000/6). TSS-3 (1020/0.5) and TSS-4 (1050/0.5) show low degree of necking from the micrographs in Figures 4.15e, f, g and h, but obtain relative densities between TSS-1 (1000/0.5) and TSS-2 (1000/6) due to close packing of the grains.

5.4 Spark plasma sintered pellets

5.4.1 Formation of secondary phases

The attempt of spark plasma sintering on Al-doped LLZO was unsuccessful as a consequence of the graphite equipment's susceptibility to Li intercalation. This outcome establishes that the utilization of graphite dies is unsuitable for this process. The spark plasma sintered pellets contain large amounts of the secondary phase $La_2Zr_2O_7$, shown in the diffractogram of SPS-3 (0.7) in Figure 4.19 with high intensity diffraction lines across all 2θ-values, due to substantial Li loss during the SPS process. This is caused by formation of VLCs, corresponding with the gas evolution observed in Figure 4.21. Additionally, reactions with the graphite die and foil extract Li from the sample and cause further Li loss.

Formation of CO_2(g) and other carbon-containing gases is likely to have occurred in the system, corresponding with the observations of Li_2CO_3 in the XRD and the increase in gas pressure during SPS. Equipment of graphite were utilized during the procedure and could induce formation of CO_2(g), that may react with Li_2O(s) according to the reaction displayed in Equation 2.4. Although the reaction is not thermodynamically favorable at RT, the application of high temperature, pressure, and current simultaneously enhances the likelihood of the reaction occurring.

5.4.2 Microstructure

The uneven densification of the spark plasma sintered pellets, presented in Figure 4.20, is caused by contamination of secondary phases, evident from the XRD pattern, inhibiting material diffusion and movement of grain boundaries in certain areas. The rapid sintering process may induce an uneven distribution of secondary phases in the material, explaining the sudden change in microstructure shown in Figure 4.20b. The contact points between the graphite foil and the material are at the outer edge of the pellet, where reactions promoting carbon-containing compositions are most likely to occur. As the pellet was milled prior to the XRD measurement to achieve a representative result of the whole sample, the phase distribution is currently unknown.

The microstructure of the material explains the incoherence of the pellets during removal from the pistons, as displayed in Appendix H.2 of SPS-2 (0.4), and the low mechanical strength causing deformation during removal, as shown in Appendix H.1 of SPS-1 (0.35) and SPS-3 (0.7). Cracks in the microstructure are also observed, as shown in Figure 4.20a. The combination of low mechanical strength, incomplete densification, uneven microstructure and highly contaminated phase composition renders the spark plasma sintered pellet unsuitable for use as a solid-state electrolyte. The use of a graphite die is unsuitable for spark plasma sintering of LALZO, and alternative die materials, such as steel, must be employed instead.

5.5 Ionic conductivity of sintered pellets

High ionic conductivity was achieved for two-step sintered 17-LALZO as a result of the obtained microstructure and phase composition. 24,2-LALZO showed lower ionic conductivity, implying that the Li excess in precursor solution of 17-LALZO was notably better than of 24,2-LALZO for obtaining a material with ionic properties suitable for use as solid-state electrolyte. The pellets sintered at 1000 °C for 0.5 h (TSS-1 (1000/0.5)) were selected for impedance assessment based on an overall evaluation of the results obtained from phase composition, microstructure and density.

For 24,2-LALZO, the ionic conductivity at RT of 5.6 $\times$ 10^{-6} S/cm corresponds with literature values for t-LLZO of around 10^{-6} S/cm, which is outside the range of what is suitable for use in solid-state electrolytes [12]. In addition, an activation energy of 0.35 eV and pre-exponential factor of 51 was obtained for 24,2-LALZO (Figure 4.23). The previous studies presented in Table 2.2 resulted in ionic conductivities of up to 100 times higher than for 24,2-LALZO observed in this study. Hence, it is evident that the tetragonal distortion combined with AGG are the reasons for the reduced Li-ion conductivity. As only one semicircle is observed in the Nyquist plot for 24,2-LALZO, it is primarily contributions from the bulk that dominate the ionic conductivity, since the density of grain boundaries is low in materials with large grains.

The ionic conductivity measured for 17-LALZO of 4.3 $\times$ 10^{-4} S/cm is within the range of the reported values from previous studies displayed in Table 2.2. By comparing the result with the sintering studies using solid state reaction and ambient air sintering, the pellets with ionic conductivities higher than 4.3 $\times$ 10^{-4} S/cm possessed higher relative densities than what was measured for 17-LALZO in this study. Ma et al. achieved single phase c-LALZO with ionic conductivity of 5.3 $\times$ 10^{-4} S/cm and relative density of 92 % after sintering at 1210 °C for 6 h, indicating that increasing the density of the pellet could lead to an improvement in ionic conductivity [50]. By making adjustments in the sintering program, such as optimizing temperatures and duration, while ensuring formation of single phase c-LALZO and avoid the presence of secondary phases that could impede the transport of Li^+, it should be possible to further enhance the ionic conductivity.

17-LALZO exhibits two temperature ranges with different activation energies and pre-exponential factors, as depicted in Figure 4.24, where a change in the slope of the curve occurs at 80 °C. Previous studies have reported similar behavior in Al-doped LLZO. Sastre et al. investigated the ionic conductivity of thin films (thicknesses of 450 to 550 nm) made of Al-doped LLZO, revealing two temperature ranges with different activation energies during impedance measurements with a shift above 100 °C [75]. In contrast to the findings in this study, which resulted in activation energies of 0.22 eV for lower temperatures and 0.47 eV for higher temperatures, Sastre et al. observed a shift resulting in 0.49 eV for lower temperatures and 0.32 eV for higher temperatures. Sastre explained this phenomenon with ion-ion correlation. It is expected that measurements of pellets and thin films may differ from each other, but the reason for the opposite shift remains unclear.

The pre-exponential factor is usually associated with the frequency of ion hopping in the material, corresponding to Li^+ in this case. As the pre-exponential factor for 17-LALZO increases from 0.34 to 1070 S/mol at temperatures above 80 °C, it is suggested that a shift in conductivity mechanisms from grain boundaries to bulk (grain) diffusion occurred. It is seen that there is no shift in activation energy for 24,2-LALZO which may originate from AGG and the corresponding low density of grain boundaries, suggesting that the observed activation energy is dominated by bulk (grain) diffusion in tetragonal LALZO [76]. However, it should be emphasized that the above interpretation is preliminary and further investigations are needed to reveal the nature of Li-conduction in cubic and tetragonal LALZO.

6 | Conclusion

Stable, carbon-free and homogeneous precursor solutions were successfully synthesized from nitrates, providing precursors as an excellent basis for the synthesis of single phase c-LALZO. Calcination of precursor powders of 24.2 mol% (24,2-LALZO) and 17 mol% (17-LALZO) Li excess at 750 °C for 6 h resulted in t-LALZO and c-LALZO, respectively. Both calcined powders were observed with Li_2CO_3 due to exposure to ambient air during synthesis. 17-LALZO was observed with $La_2Zr_2O_7$ as a consequence of Li loss during the heat treatment.

Two-step sintering of 17-LALZO yielded single phase c-LALZO, achieved by employing a secondary sintering temperature of 1000 °C for a duration of 6 h. The samples sintered at 1000, 1020 and 1050 °C for 0.5 h were indexed to c-LALZO and traces of $La_2Zr_2O_7$ and Li_2CO_3. The difference in phase composition can be explained by small variations in the calcined powder. Abnormal grain growth was suppressed during two-step sintering of 17-LALZO, evident from a homogeneous microstructure and narrow grain size distribution, reaching relative densities of 88.2 to 90.4%. All pellets of 24,2-LALZO were identified as single phase t-LALZO due to Li excess. Abnormal grain growth occurred during sintering of 24,2-LALZO due to the higher Li content and subsequently formation of Li-Al-O phases, inducing rapid grain growth in the structure. Relative densities of 91.8 to 93.4% were measured for 24,2-LALZO.

Measurements of electrochemical impedance spectroscopy conducted on two-step sintered pellets with a secondary sintering temperature of 1000 °C for 0.5 hours proved higher ionic conductivity for 17-LALZO, with 4.3×10^{-4} S/cm, in comparison to 24,2-LALZO with 5.6×10^{-6} S/cm. The ionic conductivity obtained for 17-LALZO aligns well with literature and is close to the acceptable range for utilization in solid-state batteries (between 10^{-3} and 10^{-4} S/cm). Improving the relative density, while suppressing AGG and achieving a single phase material, is expected to increase the ionic conductivity even further, indicating that the process utilized in this study is very promising for achieving a material with excellent properties for use in Li-ion batteries. Two temperature ranges with different activation energies and pre-exponential factors was observed for 17-LALZO, where the increase at above 80 °C was suggested to originate from a shift in conductivity mechanism from grain boundaries to bulk (grain) diffusion.

Spark plasma sintering of calcined powder was considered not successful in this work, and resulted in a massive Li loss during sintering and formation of carbon-containing secondary phases due to the use of equipment made of graphite. An incoherent and heterogeneous microstructure was observed in the sintered pellets, making it unsuitable for use as solid-state electrolyte.

This study demonstrates that the use of liquid-based synthesis through spray pyrolysis can yield great results, with a low-cost setup, simplicity during operation, and an energy efficient process as lower temperatures can be utilized for a short duration, which is promising for future powder synthesis of LALZO.

7 | Further Work

Future work should aim at further increasing density of two-step sintered 17-LALZO, while suppressing AGG, for optimizing the ionic properties of the material. This can be done by further optimization of time and temperature during primary and secondary sintering, as a limited range were investigated during this work. Furthermore, a Rietveld analysis should be conducted on the calcined powders to quantify the amount of secondary phases present. Attention should be given to potential carbon contamination from air and equipment used during synthesis to minimize formation of Li_2CO_3.

Further investigation of the electronic properties of the sintered pellets should be conducted. Only one temperature program for the two-step sintered pellets were examined using EIS, and should be extended to explore the influence of differences in microstructure, phase composition and relative densities on the electronic properties. Also, the effect of two temperature regions with different activation energies and pre-exponential factors in 17-LALZO should be looked closer into, as the change in ionic properties will influence the performance of the material during battery operation.

As spark plasma sintering has shown excellent results in previous studies, efforts should be made to improve the sintering method, aiming at achieving a single phase material with coherent and dense microstructure. A reevaluation of the die material should be made, as the use of graphite caused severe Li loss and contamination, where a material inert to Al-doped LLZO could lead to significantly improved results.

Finally, to ensure the results obtained in this study are both reproducible and reliable, it is essential to conduct multiple parallel analyses using identical preparation and sintering conditions. As there were small differences in phase composition and relative densities within each composition, it becomes crucial to repeat the measurements in order to confirm the observed trends.

Bibliography

[1] Jianwu Wen, Yan Yu and Chunhua Chen. 'A review on lithium-ion batteries safety issues: existing problems and possible solutions'. In: *Materials express* 2.3 (2012), pp. 197–212.

[2] Xiangkun Wu et al. 'Safety issues in lithium ion batteries: Materials and cell design'. In: *Frontiers in Energy Research* 7 (2019), p. 65.

[3] Tirath Raj et al. 'Recycling of cathode material from spent lithium-ion batteries: Challenges and future perspectives'. In: *Journal of Hazardous Materials* 429 (2022), p. 128312.

[4] Xiulin Fan et al. 'Non-flammable electrolyte enables Li-metal batteries with aggressive cathode chemistries'. In: *Nature nanotechnology* 13.8 (2018), pp. 715–722.

[5] Charles A Geiger et al. 'Crystal chemistry and stability of "$Li_7La_3Zr_2O_{12}$" garnet: a fast lithium-ion conductor'. In: *Inorganic chemistry* 50.3 (2011), pp. 1089–1097.

[6] Md Mozammal Raju et al. 'Crystal structure and preparation of $Li_7La_3Zr_2O_{12}$ (LLZO) solid-state electrolyte and doping impacts on the conductivity: An overview'. In: *Electrochem* 2.3 (2021), pp. 390–414.

[7] Margrethe Klokkehaug. *Solid-State Lithium Batteries as the next Generation of Energy Storage Technology*. NTNU. 2022.

[8] Fei Chen et al. 'Origin of the phase transition in lithium garnets'. In: *The Journal of Physical Chemistry C* 122.4 (2018), pp. 1963–1972.

[9] Reinhard Wagner et al. 'Crystal structure of garnet-related Li-ion conductor $Li_{7-3x}Ga_xLa_3Zr_2O_{12}$: fast Li-ion conduction caused by a different cubic modification?' In: *Chemistry of materials* 28.6 (2016), pp. 1861–1871.

[10] Junji Awaka et al. 'Synthesis and structure analysis of tetragonal $Li_7La_3Zr_2O_{12}$ with the garnet-related type structure'. In: *Journal of solid state chemistry* 182.8 (2009), pp. 2046–2052.

[11] N Bernstein, MD Johannes and Khang Hoang. 'Origin of the structural phase transition in $Li_7La_3Zr_2O_{12}$'. In: *Physical review letters* 109.20 (2012), p. 205702.

[12] M Matsui et al. 'Phase stability of a garnet-type lithium ion conductor $Li_7La_3Zr_2O_{12}$'. In: *Dalton Transactions* 43.3 (2014), pp. 1019–1024.

[13] Matthew Klenk and Wei Lai. 'Local structure and dynamics of lithium garnet ionic conductors: tetragonal and cubic $Li_7La_3Zr_2O_7$'. In: *Physical Chemistry Chemical Physics* 17.14 (2015), pp. 8758–8768.

[14] G Larraz, Alodia Orera and ML Sanjuán. 'Cubic phases of garnet-type $Li_7La_3Zr_2O_{12}$: the role of hydration'. In: *Journal of Materials Chemistry A* 1.37 (2013), pp. 11419–11428.

[15] Matthew J Klenk and Wei Lai. 'Finite-size effects on the molecular dynamics simulation of fast-ion conductors: A case study of lithium garnet oxide $Li_7La_3Zr_2O_{12}$'. In: *Solid State Ionics* 289 (2016), pp. 143–149.

[16] Yubing Hu et al. 'Probing the Phase Transition during the Formation of Lithium Lanthanum Zirconium Oxide Solid Electrolyte'. In: *ACS Applied Materials & Interfaces* 14.37 (2022), pp. 41978–41987.

[17] A Kuhn et al. 'Li self-diffusion in garnet-type $Li_7La_3Zr_2O_{12}$ as probed directly by diffusion-induced Li 7 spin-lattice relaxation NMR spectroscopy'. In: *Physical Review B* 83.9 (2011), p. 094302.

[18] Hamed Salimkhani, Alp Yurum and Selmiye Alkan Gursel. 'A glance at the influence of different dopant elements on $Li_7La_3Zr_2O_{12}$ garnets'. In: *Ionics* 27.9 (2021), pp. 3673–3698.

[19] Ying Jin and Paul J McGinn. 'Al-doped $Li_7La_3Zr_2O_{12}$ synthesized by a polymerized complex method'. In: *Journal of Power Sources* 196.20 (2011), pp. 8683–8687.

[20] Wenhao Xia et al. 'Ionic conductivity and air stability of Al-doped $Li_7La_3Zr_2O_{12}$ sintered in alumina and Pt crucibles'. In: *ACS applied materials & interfaces* 8.8 (2016), pp. 5335–5342.

[21] Ezhiyl Rangasamy, Jeff Wolfenstine and Jeffrey Sakamoto. 'The role of Al and Li concentration on the formation of cubic garnet solid electrolyte of nominal composition $Li_7La_3Zr_2O_{12}$'. In: *Solid State Ionics* 206 (2012), pp. 28–32.

[22] Sangryun Kim et al. 'Epitaxial growth and lithium ion conductivity of lithium-oxide garnet for an all solid-state battery electrolyte'. In: *Dalton Transactions* 42.36 (2013), pp. 13112–13117.

[23] Yasuaki Matsuda et al. 'Phase formation of a garnet-type lithium-ion conductor $Li_{7-3x}Al_xLa_3Zr_2O_{12}$'. In: *Solid State Ionics* 277 (2015), pp. 23–29.

[24] Hanna Herskedal. 'Sintering Properties and Li-ion Conductivity of Solid-State Electrolytes with Composition $Li_{7-x}La_3Zr_{2-x}Ta_xO_{12}$ (x=0.25 and x=0.6)'. MA thesis. NTNU, 2022.

[25] Ulrik Eriksen. 'Sintering and transport properties of Al-LLZO ceramic electrolytes for use in solid-state Li-ion batteries'. MA thesis. NTNU, 2021.

[26] Marthe Nybrodahl. 'The effect of MgO-addition on sintering properties and Li-ion conductivity of solid-state electrolytes with composition $Li_{6.25}Al_{0.25}La_3Zr_2O_{12}$'. MA thesis. NTNU, 2022.

[27] Junhao Li et al. 'Low-temperature synthesis of cubic phase $Li_7La_3Zr_2O_{12}$ via sol-gel and ball milling induced phase transition'. In: *Journal of Power Sources* 412 (2019), pp. 189–196.

[28] Yan Chen et al. 'A study of suppressed formation of low-conductivity phases in doped $Li_7La_3Zr_2O_{12}$ garnets by in situ neutron diffraction'. In: *Journal of Materials Chemistry A* 3.45 (2015), pp. 22868–22876.

[29] GP Wyers and EHP Cordfunke. 'Phase relations in the system Li_2O-ZrO_2'. In: *Journal of nuclear materials* 168.1-2 (1989), pp. 24–30.

[30] Hanyu Huo et al. 'Li2CO3: a critical issue for developing solid garnet batteries'. In: *ACS Energy Letters* 5.1 (2019), pp. 252–262.

[31] Taeho Yoon et al. 'Thermal decomposition of the solid electrolyte interphase (SEI) on silicon electrodes for lithium ion batteries'. In: *Chemistry of Materials* 29.7 (2017), pp. 3237–3245.

[32] L. R. Gahan A. G. Blackman and G. H. Aylward. *Aylward and Findlays's SI Chemical Data*. 7th ed. Milton: John Wiley 6 Sons Australia, 2014.

[33] Helir Joseph Muñoz, Sophia A Korili and Antonio Gil. 'Progress and recent strategies in the synthesis and catalytic applications of perovskites based on lanthanum and aluminum'. In: *Materials* 15.9 (2022), p. 3288.

[34] Yoshitoyo Nishio and Masakuni Ozawa. 'Microstructure of La-modified Al_2O_3 support with $LaAlO_3$ nano-particles'. In: *Journal of the Ceramic Society of Japan* 116.1360 (2008), pp. 1295–1298.

[35] Anja Paulus, Rüdiger-Albert Eichel and Ulrich Simon. *Synthesis and characterization of garnet-type solid state electrolytes for lithium-ion batteries*. Tech. rep. Lehrstuhl für Materialien und Prozesse für elektrochemische Energiespeicher ..., 2019.

[36] Nagraj S Kulkarni, Theodore M Besmann and Karl E Spear. 'Thermodynamic optimization of lithia–alumina'. In: *Journal of the American Ceramic Society* 91.12 (2008), pp. 4074–4083.

[37] Xiao Huang et al. 'Manipulating Li_2O atmosphere for sintering dense $Li_7La_3Zr_2O_{12}$ solid electrolyte'. In: *Energy Storage Materials* 22 (2019), pp. 207–217.

[38] H Kudo, CH Wu and HR Ihle. 'Mass-spectrometric study of the vaporization of Li_2O (s) and thermochemistry of gaseous LiO, Li_2O, Li_3O, and Li_2O_2'. In: *Journal of Nuclear Materials* 78.2 (1978), pp. 380–389.

[39] David W Richerson and William E Lee. *Modern ceramic engineering: properties, processing, and use in design*. CRC press, 2018.

[40] Tesfaye Tadesse Molla, Nini Pryds and Rasmus Bjørk. 'Modeling Macroscopic Shape Distortions during Sintering of Multi-layers'. In: *Technical University of Denmark* (2014).

[41] Dalu Gao et al. 'Microwave assisted reactive sintering for Al doped $Li_7La_3Zr_2O_{12}$ lithium ion solid state electrolyte'. In: *Materials Research Express* 6.12 (2020), p. 125539.

[42] Adriana Castillo et al. 'Bulk Li mobility enhancement in spark plasma sintered $Li_{7-3x}Al_xLa_3Zr_2O_{12}$ garnet'. In: *Ceramics International* 44.15 (2018), pp. 18844–18850.

[43] Yanda Zhu et al. 'Enhanced Li+ Conductivity of $Li_7La_3Zr_2O_{12}$ by Increasing Lattice Entropy and Atomic Redistribution Via Spark Plasma Sintering'. In: *Available at SSRN 4425457* ().

[44] Yanhua Zhang et al. 'Field assisted sintering of dense Al-substituted cubic phase $Li_7La_3Zr_2O_{12}$ solid electrolytes'. In: *Journal of Power Sources* 268 (2014), pp. 960–964.

[45] Ramaswamy Murugan, Venkataraman Thangadurai and Werner Weppner. 'Fast lithium ion conduction in garnet-type $Li_7La_3Zr_2O_{12}$'. In: *Angewandte Chemie International Edition* 46.41 (2007), pp. 7778–7781.

[46] Biyi Xu et al. 'Multistep sintering to synthesize fast lithium garnets'. In: *Journal of Power Sources* 302 (2016), pp. 291–297.

[47] Pengcheng Zhao et al. 'Self-consolidation mechanism and its application in the preparation of Al-doped cubic $Li_7La_3Zr_2O_{12}$'. In: *Materials & Design* 139 (2018), pp. 65–71.

[48] Juliane Franciele Nonemacher et al. 'Microstructure and properties investigation of garnet structured $Li_7La_3Zr_2O_{12}$ as electrolyte for all-solid-state batteries'. In: *Solid State Ionics* 321 (2018), pp. 126–134.

[49] Stefan Smetaczek et al. 'Local Li-ion conductivity changes within Al stabilized $Li_7La_3Zr_2O_{12}$ and their relationship to three-dimensional variations of the bulk composition'. In: *Journal of Materials Chemistry A* 7.12 (2019), pp. 6818–6831.

[50] Jun Ma et al. 'A low-cost Al-doped garnet $Li_7La_3Zr_2O_{12}$ with high ionic conductivity for high-energy solid-state lithium metal batteries'. In: *Applied Physics Letters* 121.19 (2022), p. 193901.

[51] Bo Dong et al. 'Low temperature synthesis of garnet solid state electrolytes: Implications on aluminium incorporation in $Li_7La_3Zr_2O_{12}$'. In: *Solid State Ionics* 350 (2020), p. 115317.

[52] Ying Tian et al. 'Formation mechanism of sol-gel synthesized $Li_{7-3x}Al_xLa_3Zr_2O_{12}$ and the influence of abnormal grain growth on ionic conductivity'. In: *Solid State Ionics* 354 (2020), p. 115407.

[53] Hany El-Shinawi et al. 'Low-temperature densification of Al-doped $Li_7La_3Zr_2O_{12}$: a reliable and controllable synthesis of fast-ion conducting garnets'. In: *Journal of Materials Chemistry A* 5.1 (2017), pp. 319–329.

[54] Janez Košir et al. 'Comparative analysis on the thermal, structural, and electrochemical properties of Al-doped $Li_7La_3Zr_2O_{12}$ solid electrolytes through solid state and sol-gel routes'. In: *Solid State Ionics* 380 (2022), p. 115943.

[55] Noriko Saito et al. 'Sintering behaviors of highly sinterable Al-doped $Li_7La_3Zr_2O_{12}$ powder prepared by polymerized-complex method'. In: *Ceramics International* 48.15 (2022), pp. 22262–22268.

[56] Ian J McColm and NJ Clark. 'Forming, Shaping, and Working of High-Performance Ceramics'. In: *Blackie and Son Ltd., 1988,* (1988), p. 345.

[57] W Robert and P Haasen. *Physical Metallurgy, Fourth, Revised and Enhanced Edition*. 1996.

[58] A Lawrence et al. 'Parsing abnormal grain growth'. In: *Acta Materialia* 103 (2016), pp. 681–687.

[59] Xiao Huang et al. 'Two-step sintering strategy to prepare dense Li-Garnet electrolyte ceramics with high Li^+ conductivity'. In: *Ceramics International* 44.5 (2018), pp. 5660–5667.

[60] Yali Luo et al. 'Influence of sintering aid on the microstructure and conductivity of the garnet-type W-doped $Li_7La_3Zr_2O_{12}$ ceramic electrolyte'. In: *Journal of Materials Science: Materials in Electronics* 30.18 (2019), pp. 17195–17201.

[61] Nataly Carolina Rosero-Navarro et al. 'Effect of sintering additives on relative density and Li-ion conductivity of Nb-doped $Li_7La_3Zr_2O_{12}$ solid electrolyte'. In: *Journal of the American Ceramic Society* 100.1 (2017), pp. 276–285.

[62] Narayanasamy Janani et al. 'Influence of sintering additives on densification and Li^+ conductivity of Al doped $Li_7La_3Zr_2O_{12}$ lithium garnet'. In: *Rsc Advances* 4.93 (2014), pp. 51228–51238.

[63] Shaojie Chen et al. 'Low-sintering-temperature garnet oxides by conformal sintering-aid coating'. In: *Cell Reports Physical Science* 2.9 (2021), p. 100569.

[64] Jianmeng Su et al. 'Overcoming the abnormal grain growth in Ga-doped $Li_7La_3Zr_2O_{12}$ to enhance the electrochemical stability against Li metal'. In: *Ceramics International* 45.12 (2019), pp. 14991–14996.

[65] Ubenthiran Sutharsini, Murugathas Thanihaichelvan and Ramesh Singh. 'Two-step sintering of ceramics'. In: *Sintering of Functional Materials* (2018), pp. 3–22.

[66] Zheng-Yang Hu et al. 'A review of multi-physical fields induced phenomena and effects in spark plasma sintering: Fundamentals and applications'. In: *Materials & Design* 191 (2020), p. 108662.

[67] Yunis Ahmad Dar and Nazir Ahmad Sheikh. 'A review of fabrication and properties of spark plasma sintered tungsten carbide based advanced composites'. In: *Proceedings of the Institution of Mechanical Engineers, Part E: Journal of Process Mechanical Engineering* 236.3 (2022), pp. 1216–1228.

[68] M Suárez et al. 'Challenges and opportunities for spark plasma sintering: a key technology for a new generation of materials'. In: *Sintering applications* 13 (2013), pp. 319–342.

[69] John TS Irvine, Derek C Sinclair and Anthony R West. 'Electroceramics: characterization by impedance spectroscopy'. In: *Advanced materials* 2.3 (1990), pp. 132–138.

[70] Md-Jamal Uddin and Sung-Jin Cho. 'Reassessing the bulk ionic conductivity of solid-state electrolytes'. In: *Sustainable Energy & Fuels* 2.7 (2018), pp. 1458–1462.

[71] Alexandros Ch Lazanas and Mamas I Prodromidis. 'Electrochemical Impedance Spectroscopy A Tutorial'. In: *ACS Measurement Science Au* (2023).

[72] MJ Joshi. 'Importance of Impedance Spectroscopy Technique in Materials Characterization: A Brief Review'. In: *Mechanics, Materials Science & Engineering MMSE Journal. Open Access* 9 (2017).

[73] Hanna Herskedal. 'Phase stability and sintering properties of $Li_{7-x}La_3Zr_{2-x}Ta_xO_{12}$ produced by spray pyrolysis (x = 0.25 and 0.6)'. MA thesis. NTNU, 2021.

[74] Davor Balzar. 'X-ray diffraction line broadening: Modeling and applications to high-T_c superconductors'. In: *Journal of research of the National Institute of Standards and Technology* 98.3 (1993), p. 321.

[75] Jordi Sastre et al. 'Lithium garnet $Li_7La_3Zr_2O_{12}$ electrolyte for all-solid-state batteries: closing the gap between bulk and thin film Li-ion conductivities'. In: *Advanced Materials Interfaces* 7.17 (2020), p. 2000425.

[76] Junko Habasaki, Carlos Leon and KL Ngai. 'Dynamics of glassy, crystalline and liquid ionic conductors'. In: *Top Appl Phys* 132 (2017), pp. 355–410.

[77] Anne-Elisabeth Gobichon, Jean-Paul Auffrédic and Daniel Louër. 'Thermal decomposition of neutral and basic lanthanum nitrates studied with temperature-dependent powder diffraction and thermogravimetric analysis'. In: *Solid State Ionics* 93.1-2 (1996), pp. 51–64.

[78] Goran Štefanić et al. 'Formation of ZrO_2 by the thermal decomposition of zirconium salts'. In: *Croatica chemica acta* 69.1 (1996), pp. 223–239.

Appendix

A Decomposition of nitrates

Decomposition reactions of nitrates utilized in the synthesis of precursor solutions are shown in Equations A.1, A.2, A.3 and A.4. Decomposition temperatures are displayed, where values for $LiNO_3(s)$ and $Al(NO_3)_3(s)$ are retrieved from SI Chemical Data [32], $La(NO_3)_3(s)$ from [77] and $ZrO(NO_3)_2(s)$ from [78].

$$4LiNO_3(s) \rightarrow 2Li_2O(s) + 4NO_2(g) + O_2(g), \qquad T_d = 600°C \tag{A.1}$$

$$4La(NO_3)_3(s) \rightarrow 2La_2O_3(s) + 12NO_2(g) + 3O_2(g), \qquad T_d \approx 500°C \tag{A.2}$$

$$4Al(NO_3)_3(s) \rightarrow 2Al_2O_3(s) + 12NO_2(g) + 3O_2(g), \qquad T_d = 150°C \tag{A.3}$$

$$4ZrO(NO_3)_2(s) \rightarrow 2ZrO_2(s) + 4NO_2(g) + O_2(g), \qquad T_d \approx 400°C \tag{A.4}$$

B | Decomposition of Li_2CO_3

The partial pressure of Li_2CO_3 is used to evaluate the decomposition rate of the component during heating. Decomposition reaction is shown in Equation B.1. The transition from solid to liquid Li_2CO_3 is shown in Equation B.2. All values are retrieved from SI Chemical Data [32].

$$\text{I)} \quad Li_2CO_3(s) \rightarrow Li_2O(s) + CO_2(g) \tag{B.1}$$

$$\text{II)} \quad Li_2CO_3(s) \rightarrow Li_2CO_3(l) \tag{B.2}$$

By combining the two reactions we obtain Equation B.3, which can be used to calculate the partial pressure of $CO_2(g)$.

$$\text{III)} \quad Li_2CO_3(l) \rightarrow Li_2O(s) + CO_2(g) \tag{B.3}$$

Equation for Gibbs free energy is shown in B.4, where ΔH is the change in enthalpy, ΔS is the change in entropy, T is the absolute temperature in Kelvin, R is the gas constant, K is the activity coefficient and a_i is the activity of specie i. The reaction occurs if Gibbs free energy has a value below 0.

$$\Delta G^\circ = \Delta H^\circ - T\Delta S^\circ = -RTln(K) = -RTln\frac{a_{Li_2O(s)}a_{CO_2(g)}}{a_{Li_2CO_3(l)}} \tag{B.4}$$

Activities of $Li_2CO_3(l)$ and $Li_2O(s)$ are assumed to be 1 due to their thermodynamic states, while the activity of $CO_2(g)$ is assumed ideal and equal to the partial pressure of the component. This gives an expression for the partial pressure of $CO_2(g)$, shown in Equation B.5.

$$\Delta_r G^\circ = -RTln(p_{CO_2(g)}) \Rightarrow p_{CO_2(g)} = \exp(-\frac{\Delta_r G^\circ}{RT}) \tag{B.5}$$

$\Delta_{r,I}H^\circ$ and $\Delta_{r,I}S^\circ$, for decomposition reaction shown in Equation B.1, is calculated in Equations B.6 and B.7.

$$\Delta_{r,I}H^\circ = \sum H^\circ_{f,products} - \sum H^\circ_{f,reactants} = (-598 + (-394)) - (-1216))\,kJ/mol = 224\,kJ/mol \tag{B.6}$$

$$\Delta_{r,I}S^\circ = \sum S^\circ_{f,products} - \sum S^\circ_{f,reactants} = ((38 + 214) - (90))\,J/Kmol = 162\,J/Kmol \tag{B.7}$$

Values from the reaction displayed in Equation B.2 can be found by using $\Delta_{\text{fus}}\text{H}$, shown in Equation B.8 and B.9.

$$\Delta_{\text{r,II}}\text{H}^\circ = -\Delta_{\text{fus}}\text{H} = -45\,\text{kJ/mol} \tag{B.8}$$

$$\Delta_{\text{r,II}}\text{S}^\circ = \frac{\Delta_{\text{r}}\text{H}^\circ}{\text{T}_{\text{fus}}} = \frac{-45000\text{J/mol}}{996\text{K}} = -45.18\,\text{J/Kmol} \tag{B.9}$$

Values for the total enthalpy and entropy of the reaction in Equation B.3 are calculated in Equations B.10 and B.11.

$$\Delta_{\text{r,III}}\text{H}^\circ = (224 + (-45))\,\text{kJ/mol} = 179\,\text{kJ/mol} \tag{B.10}$$

$$\Delta_{\text{r,III}}\text{S}^\circ = (162 + (-45.18))\,\text{J/Kmol} = 116.82\,\text{J/Kmol} \tag{B.11}$$

By using the total enthalpies and entropies from Equations B.10 and B.11, values for $\text{p}_{\text{CO}_2\text{(g)}}$ can be obtained using Equation B.5. Partial pressure for CO_2(g) for selected temperatures around the melting point of Li_2CO_3(s) are shown in Table B.1.

Table B.1: Calculated partial pressures and Gibbs free energies of CO_2(g) at temperatures between 700 and 800 °C.

Temperature [$^\circ C$]	$\Delta_r G^\circ$ [J/Kmol]	Partial pressure [bar]
700	65 354	3.1×10^{-4}
723	62 667	5.2×10^{-4}
750	59 514	9.1×10^{-4}
775	56 594	1.5×10^{-3}
800	53 674	2.4×10^{-3}

C Thermal behaviour of precursor powders

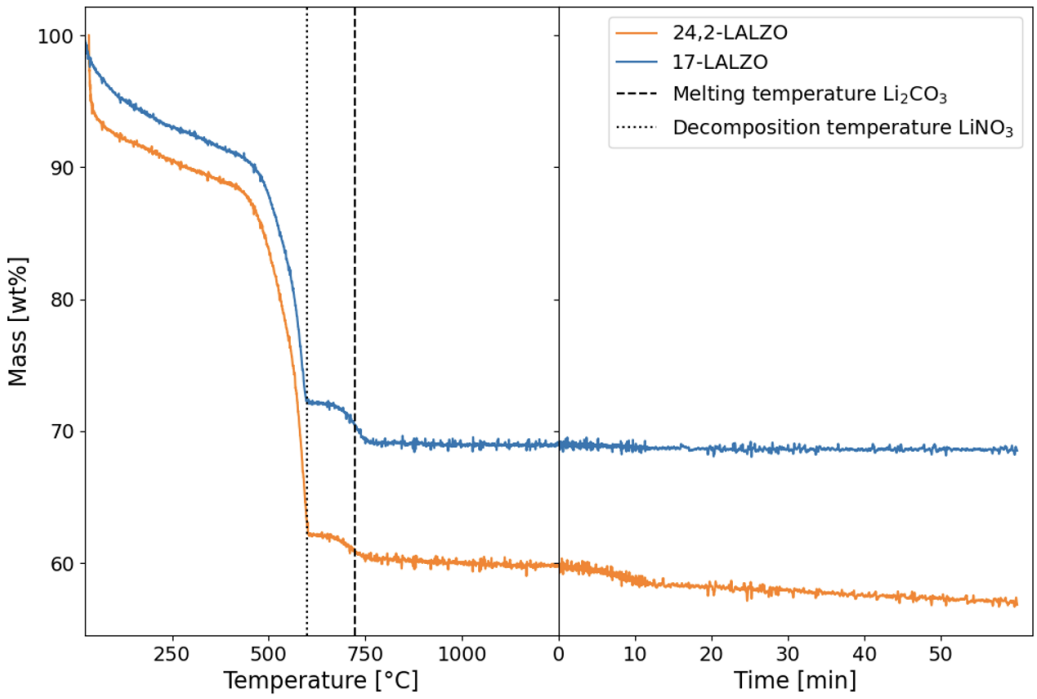

Figure C.1: Thermogravimetric analysis (TGA) of precursor powders, including all temperatures and holding time of 1 h. Melting temperature of Li_2CO_3 and decomposition temperature of $LiNO_3$ displayed as broken lines.

D High temperature X-ray diffraction

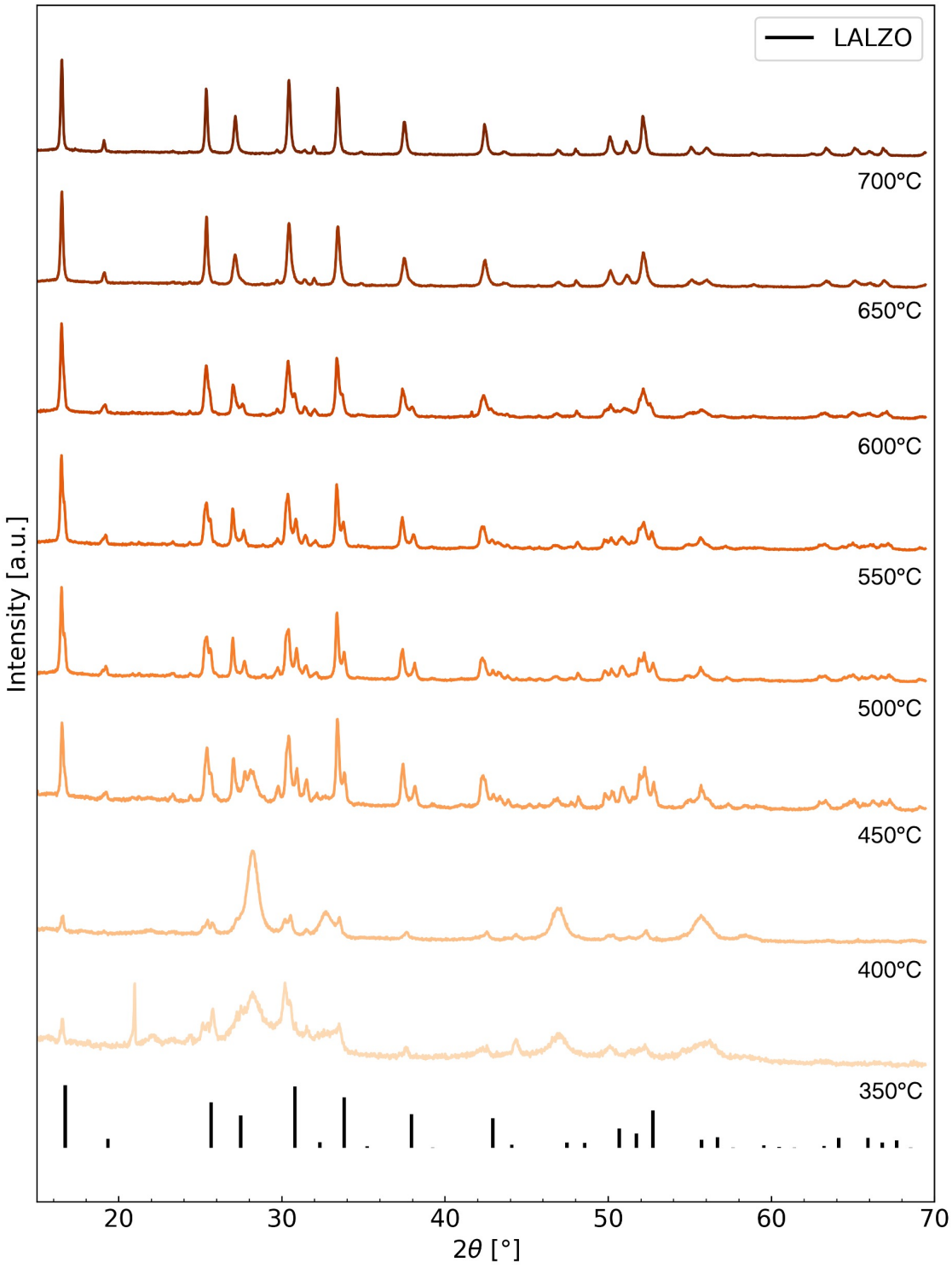

Figure D.1: High-temperature XRD of 24,2-LALZO precursor powder between 350 and 700 °C, with temperature steps of 50 °C. Temperatures for each scan are displayed to the right.

E | Weight loss after calcination

Expected mass loss

Calculations of expected weight loss were based on the nominal stochiometries for the compositions, $Li_{7.31}Al_{0.25}La_3Zr_2O_{12}$ (17-LALZO) and $Li_{7.76}Al_{0.25}La_3Zr_2O_{12}$ (24,2-LALZO), with 1 mole as a base. Assuming complete decomposition of nitrates to oxides and no secondary phases present.

M is the molar mass, n is the stoichiometric amount in moles, m is calculated mass using Equation E.1 and Δm represents the change in mass after decomposition in %. a and b refers to before and after decomposition. The stoichiometric amount for the oxides was found using decomposition reactions in Appendix A. Expected change in mass for powders is calculated in Equation E.2 using values from Table E.1. Expected mass loss is calculated using Equation E.3 and is displayed in Table E.2.

$$\mathrm{m} = \mathrm{M} \cdot \mathrm{n} \tag{E.1}$$

$$\Delta\mathrm{m} = \frac{\mathrm{m_{calcined}}}{\mathrm{m_{precursor}}} = \frac{\mathrm{m_{Al,b}} + \mathrm{m_{La,b}} + \mathrm{m_{Zr,b}} + \mathrm{m_{Li,b}}}{\mathrm{m_{Al,a}} + \mathrm{m_{La,a}} + \mathrm{m_{Zr,a}} + \mathrm{m_{Li,a}}} = \frac{624.68\,\mathrm{g} + \frac{1}{2} \cdot \mathrm{x} \cdot \mathrm{M_{Li_2O}}}{1747.02\,\mathrm{g} + \mathrm{x} \cdot \mathrm{M_{LiNO_3}}} \tag{E.2}$$

$$\mathrm{m_{loss}} = \frac{\mathrm{m_{precursor}} - \mathrm{m_{calcined}}}{\mathrm{m_{precursor}}} = 1 - \Delta\mathrm{m} \tag{E.3}$$

Table E.1: Molar mass, stoichiometry and calculated mass for nitrates and oxides.

i	$Al(NO_3)_3$	$La(NO_3)_3$	$ZrO(NO_3)_2$	$LiNO_3$	Al_2O_3	La_2O_3	ZrO_2	Li_2O
	a				b			
M_i [g/mol]	375.13	324.92	339.24	68.95	101.96	325.81	123.22	29.88
n_i [mol]	0.25	3	2	x	$\frac{1}{2}\cdot$ 0.25	$\frac{1}{2}\cdot$ 3	$\frac{1}{2}\cdot$ 2	$\frac{1}{2}\cdot$ x
m_i [g]	93.78	974.76	678.49	x · M	12.74	488.72	123.22	$\frac{1}{2}\cdot$ x · M

Table E.2: Calculated expected mass loss for compositions of 17 and 24.2% Li excess. Δm = expected change in mass, m_L = expected mass loss.

Composition	x [mol]	Δm [%]	m_L [%]
17-LALZO	7.31	32.6	67.4
24,2-LALZO	7.76	32.5	67.5

Calcined mass loss

Precursor powders 24,2-LALZO and 17-LALZO were calcined in several batches. Masses before (m_p) and after (m_c) calcination are displayed in Table E.3. Mass loss (m_L) was calculated using Equations E.4 and E.5. All batches of same composition were mixed and stored in the same beaker.

$$m_L[g] = m_p - m_c \tag{E.4}$$

$$m_L[\%] = \frac{m_p - m_c}{m_p} \times 100 \tag{E.5}$$

Table E.3: Measured mass prior to (m_p) and after (m_c) calcination. Mass losses (m_L) included.

24,2-LALZO				17-LALZO			
m_p [g]	m_c [g]	m_L [g]	m_L [%]	m_p [g]	m_c [g]	m_L [g]	m_L [%]
6.129	4.243	1.886	30.8	6.165	4.489	1.676	27.2
5.986	4.264	1.722	28.8	6.193	4.508	1.685	27.2
5.856	4.265	1.591	27.2	5.966	4.341	1.625	27.2
5.841	4.233	1.608	27.5	6.183	4.541	1.642	26.6
5.845	4.055	1.790	30.6	6.181	4.540	1.641	26.6
5.748	3.986	1.762	30.7	6.093	4.461	1.632	26.8
5.899	4.024	1.875	31.8	6.035	4.416	1.619	26.8
5.970	4.113	1.857	31.1				
6.110	4.109	2.001	32.8				
5.882	4.075	1.807	30.7				
5.975	4.136	1.839	30.8				
Mean			30.2				26.9

F Archimedes' measurements

Measurements of masses and temperatures from Archimedes' method are listed in Table F.1, together with calculated values for densities and porosity. Due to the inert behavior of isopropanol to LALZO, this was used as the immersion liquid during measurements of submerged and wet weights.

The theoretical density of LALZO, ρ_{th}, was used for estimating the relative densities of the sintered pellets, and was estimated using Equation F.1. The lattice parameter, a, of the unit cell of 8 pfu pure cubic LLZO was found in litterature equal to 12.9438Å. N_A denotes Avogadro's number, M_i is the molar mass of specie i found using SI Chemical Data [32] and a^3 represents the volume of the cubic unit cell.

$$\rho_{th} = \frac{8M_{LLZO}}{N_A a^3} = 8 \times \frac{6.25M_{Li} + 0.25M_{Al} + 3M_{La} + 2M_{Zr} + 12M_O}{N_A(12.9438 \times 10^{-8})^3} = 5.1 \text{ g/cm}^3 \tag{F.1}$$

The temperature dependent density of isopropanol, ρ_{liq}, is calculated using Equation F.2.

$$\rho_{liq} = -0.0009 \times T + 0.8018 \tag{F.2}$$

Where T is the temperature in °C during measurements of m_2. The bulk density is calculated as shown in Equation F.3, where m_1 is the mass of the dry pellet, m_2 is the mass of the pellet submerged in isopropanol and m_3 is the pellet mass with the liquid in open pores.

$$\rho_b = \frac{m_1}{m_3 - m_2} \times \rho_{liq} \tag{F.3}$$

The apparent porosity, π_a, is calculated using Equation F.4. The total or true porosity, π_t, is calculated as shown in Equation F.5, where ρ_t is the theoretical density of LALZO. Relative density, *RD*, is found using Equation F.6.

$$\pi_a = \frac{m_3 - m_1}{m_3 - m_2} \times 100 \tag{F.4}$$

$$\pi_t = \frac{\rho_t - \rho_b}{\rho_t} \times 100 \tag{F.5}$$

$$\text{RD} = 100 - \pi_t \tag{F.6}$$

Table F.1: Measurements and calculations from Archimedes' method.

Sample	m_1 [g]	m_2 [g]	m_3 [g]	T_{iso} [°C]	ρ_{liq} [g/cm^3]	ρ_b [g/cm^3]	π_a [%]	π_t [%]	RD [%]
24,2 TSS-1	0.327	0.274	0.328	20	0.784	4.77	2.05	6.56	93.4
24,2 TSS-2	0.317	0.265	0.318	20	0.784	4.75	1.34	6.88	93.1
24,2 TSS-3	0.382	0.320	0.383	21	0.783	4.73	1.11	7.28	92.7
24,2 TSS-4	0.323	0.270	0.325	18	0.786	4.68	2.58	8.17	91.8
17 TSS-1	0.331	0.276	0.332	17	0.787	4.61	1.59	9.63	90.4
17 TSS-2	0.324	0.269	0.326	20	0.784	4.50	3.01	11.77	88.2
17 TSS-3	0.355	0.293	0.355	21	0.783	4.51	0	11.63	88.4
17 TSS-4	0.333	0.270	0.334	18	0.786	4.56	1.92	10.56	89.4

G Microstructure of sintered pellets

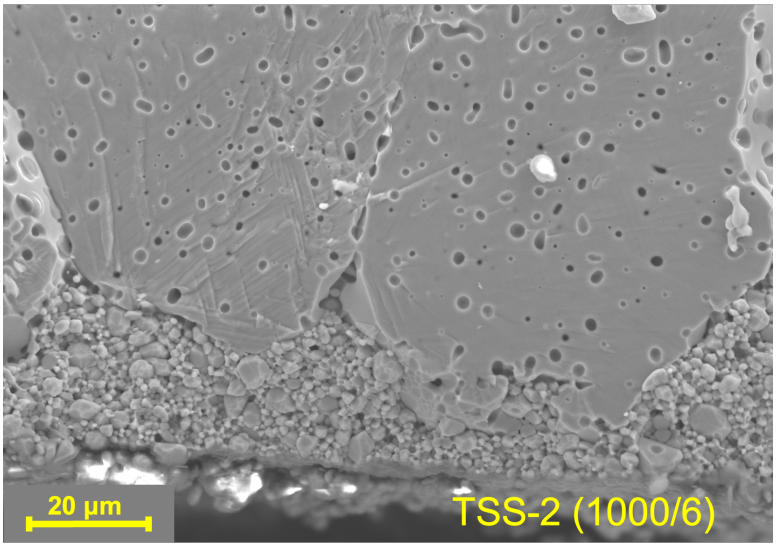

Figure G.1: Secondary electron micrograph of TSS-2 (1000/6) 24,2-LALZO, displaying accumulation of small grains towards the edge. White areas caused by charging during imaging.

H Spark plasma sintered pellets

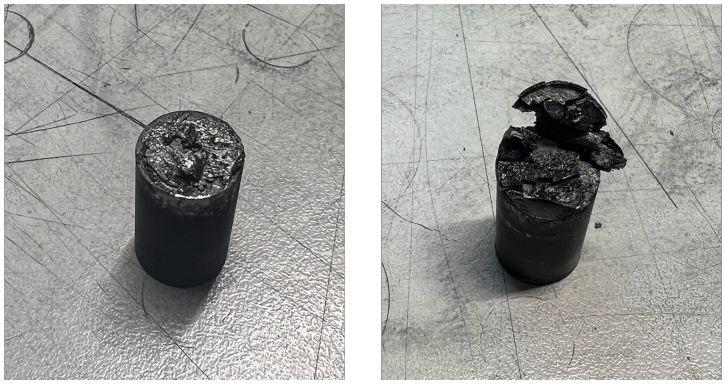

(a) (b)

Figure H.1: Photos captured after spark plasma sintering of 17-LALZO. The material is still on the pistons. SPS-1 (0.35) in a) and SPS-3 (0.7) in b).

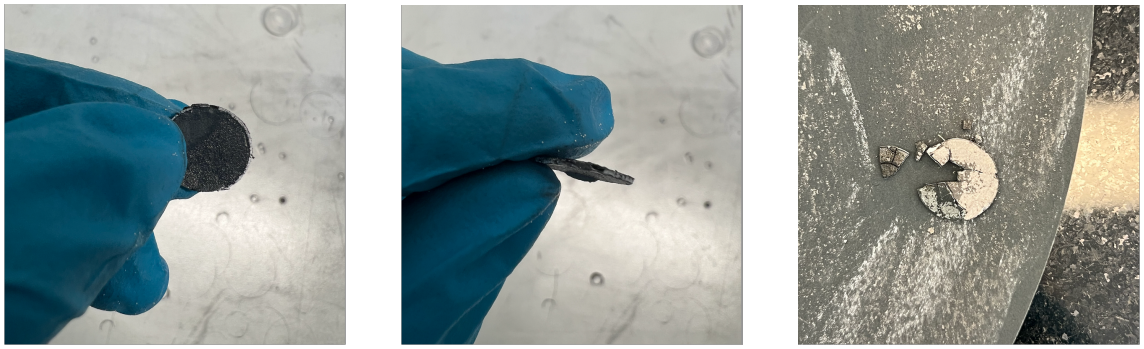

(a) (b) (c)

Figure H.2: Photos captured after spark plasma sintering of 17-LALZO using SPS-2 (0.4). Pellet surface with carbon paper displayed in a), thickness of pellet in b), attempt of removing carbon foil using SiC paper in c).

I Electrochemical impedance measurements

Table I.1: Dimensions of sintered pellets utilized during EIS measurements.

Sample	Sintering program	Thickness [cm]	Diameter [cm]	Volume [cm^3]
24,2-LALZO	TSS-1 (1000/0.5)	0.14	0.82	0.53
17-LALZO	TSS-1 (1000/0.5)	0.14	0.73	0.42

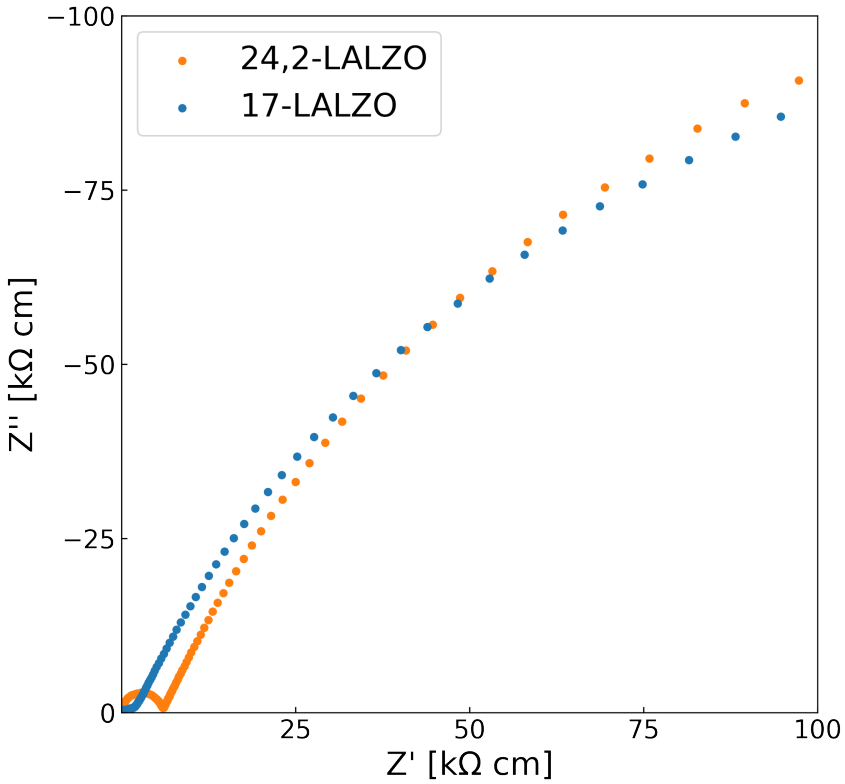

Figure I.1: Complete Nyquist plot for measurements conducted at room temperature. Displaying sintered pellets of TSS-1 (1000/0.5), with 24,2-LALZO in orange and 17-LALZO in blue.